LIFT : Liège Innovation Flight Team

Ultra Premium Long Range Business Jet

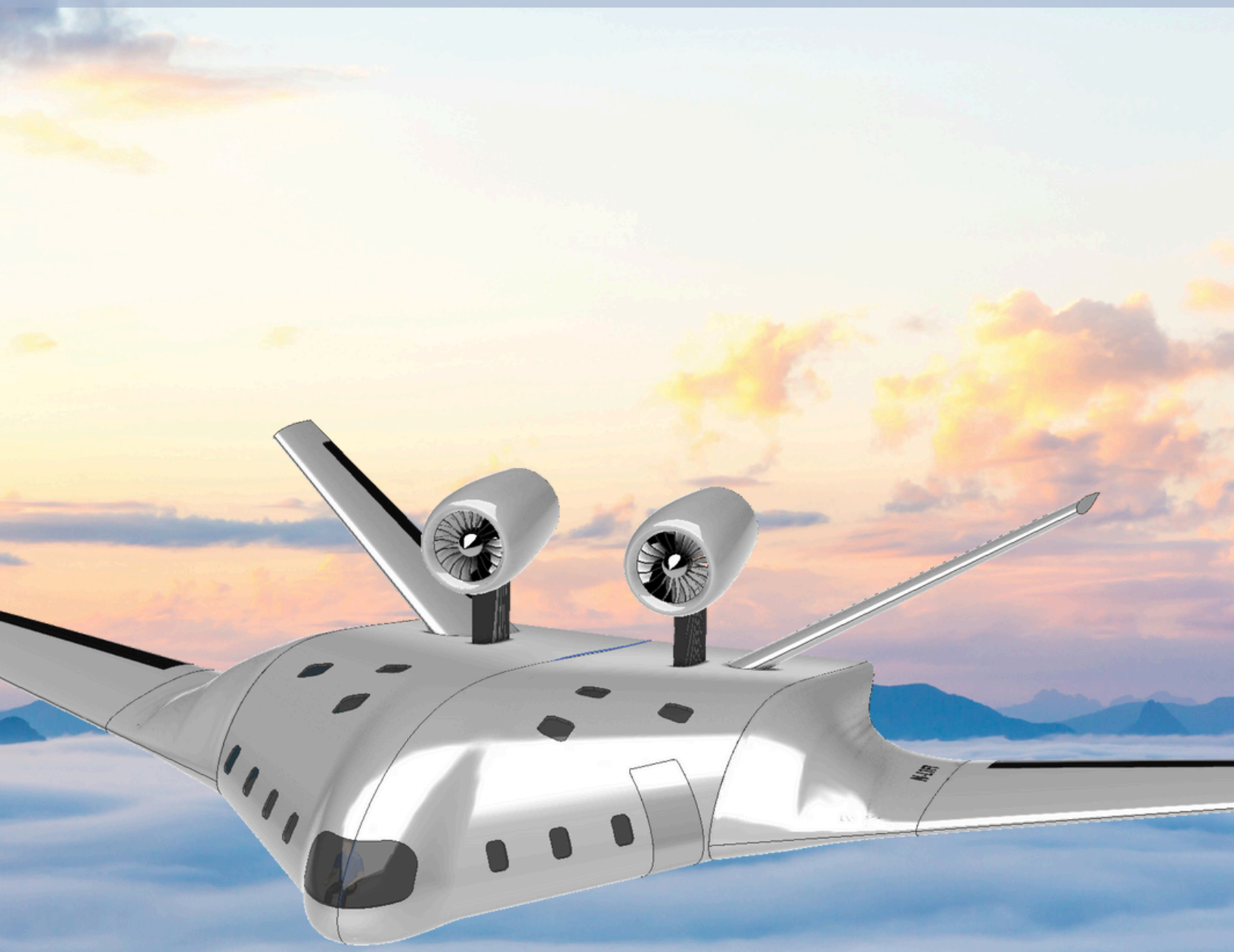

Academic year 2024-2025

LIÈGE université
Sciences Appliquées

AIAA

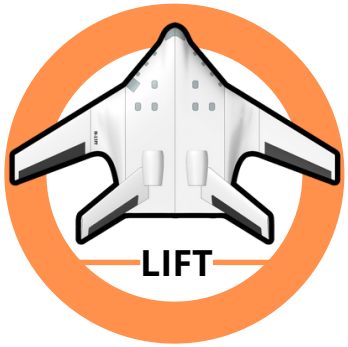

8000 nm Range

MACH 0.9

Pratt & Whitney PW1521G

$66,461,123

L/D = 16.95

8 passengers

MTOW = 105,682 lbs

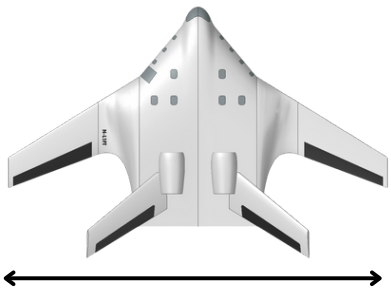

Span = 94.98 ft

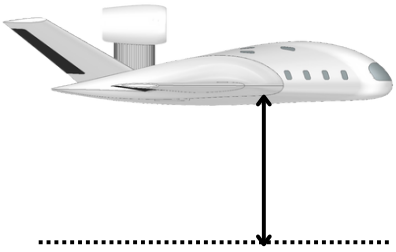

Cruise altitude = 41,010.5 ft

TEAM MEMBERS

Name	Uliège ID	AIAA ID	Email	Signature	
BELBOOM Louis	s213169	1763138	louis.belboom@student.uliege.be		
DAVID Amos	s2407141	1762549	aodavid@student.uliege.be		
DE LAMALLE Emile	s214035	1761260	emile.delamalle@student.uliege.be		
DI PUMA Léo	s213170	1762500	leo.dipuma@student.uliege.be		
VAILLOT Guillaume	s2402423	1761267	guillaume.vaillot@student.uliege.be		
SCHYNS Diego	s212522	1762543	diego.schyns@student.uliege.be		
VAN HOYE Antoine	s200743	1760580	antoine.vanhoye@student.uliege.be		

FACULTY ADVISORS

Name
ANDRIANNE Thomas
NOELS Ludovic

ASSISTANTS

Name
BUDO Arnaud
DECHAMPS Paul

Contents

Chapter 1. Introduction

Nowadays, business aviation plays a significant role in air transportation through business jet operations. Following a slowdown during the COVID-19 pandemic, which affected the entire aviation industry, the market has rebounded with an increasing number of passengers [1]. A similar trend is observed in the business aviation sector, which has regained its pre-pandemic growth trajectory [2]. This resurgence reflects the demand from affluent individuals seeking personalized, efficient, and comfortable travel experiences. Consequently, the business aviation sector must continuously evolve to meet these changing expectations, often requiring extended flight ranges, reduced takeoff and landing distances, and improved airport accessibility. Additionally, increasing pressure to reduce operating costs and limit environmental impact drives the need for more efficient business jets, both economically and ecologically.

In response to these industry challenges, the American Institute of Aeronautics and Astronautics (AIAA) has established a competition for graduate students to design a next-generation, ultra-premium, long-range business jet [3]. As specified in the AIAA Graduate Team Aircraft Design Competition requirements, participants must achieve a balance between range, cruise speed, takeoff performance, landing performance, and interior layout while ensuring regulatory compliance and market feasibility.

This report presents the conceptual and the preliminary design of a business jet developed in response to these challenging requirements. It provides an in-depth examination of the design process at the conceptual design stage. The report is organized into several sections detailing each aspect of the aircraft, including its overall configuration, structural components, and performance characteristics.

Chapter 2. Requirements

The Request for Proposal (RFP) outlines the design criteria for the next generation of high-end business jets. The proposed aircraft must meet stringent certification, performance, and operational requirements to ensure compliance with industry standards and to satisfy customer expectations.

2.1 General requirements

The aircraft design must comply with the Federal Aviation Administration (FAA) 14 CFR Part 25 certification requirements [4]. The main constraints specified by AIAA for this design are summarized in Table 2.1.

Constraint	Requirement
Mach range	[0.85-0.92]
Engine availability	Must be in service by 2035
Interior layout	Private room with queen-size bed, two lavatories
Flight crew	2 pilots, 1 flight attendant
Passenger weight	215 lb per person
Baggage allowance	50 lb per passenger, 8 ft^3 per person
Water storage	Sufficient for a 30-minute shower

Table 2.1: Key design constraints specified by AIAA for the design.

2.2 Missions

LIFT must fulfill three missions specified by the AIAA. Table 2.2 presents the requirements for the Aspen economic mission, defined as the route from Van Nuys Airport (KVNY) to Aspen–Pitkin County Airport (KASE). The Napa economic mission, from Napa County Airport (KAPC) to Mexico City Airport (MEX), is described in Table 2.3. Finally, the long-range design Passenger mission is outlined in Table 2.4.

Requirement	
Range	644 nm
Passenger number	4
Takeoff	59°F at standard pressure on an 8,000 ft dry runway; elevation: 802.1 ft
Landing	20°F at standard pressure to an 8,006 ft runway; elevation: 7,837.9 ft
Additional	Max wingspan of 95 ft; wheel braking coefficient of 0.16

Table 2.2: Mission requirements for the Aspen economic mission [5, 6].

Requirement	
Range	1,651.53 nm
Passenger number	8
Takeoff	75°F at standard pressure from a 5,930 ft dry runway; elevation: 35.5 ft
Landing	85°F at standard pressure on a 12,966 ft dry runway; elevation: 7,320 ft
Additional	Storage of 12 cases of wine

Table 2.3: Mission requirements for the Napa economic mission [7, 8].

Requirement	
Range	8,000 nm
Passenger number	8
Takeoff	Sea level standard day temperature and pressure from a 6,000 ft dry runway
Landing	Sea level standard day temperature and pressure to a 6,000 ft dry runway

Table 2.4: Mission requirements for the design passenger mission.

Figure 2.1 summarizes the most restrictive requirements concerning the flight.

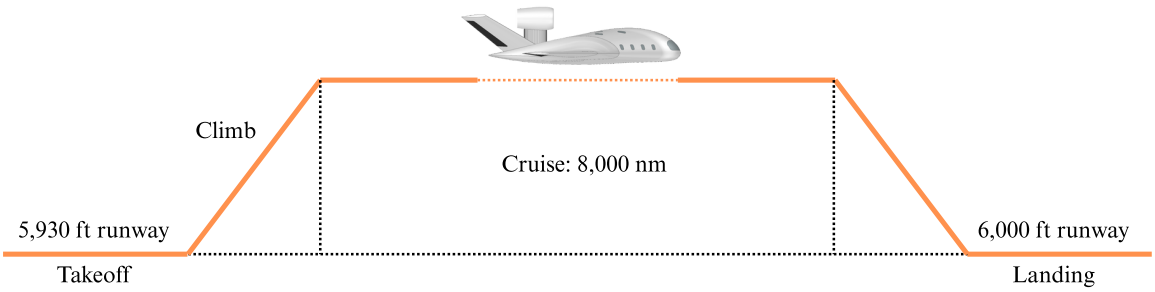

Figure 2.1: Graphical summary of main requirements about the missions.

Chapter 3. Methodology

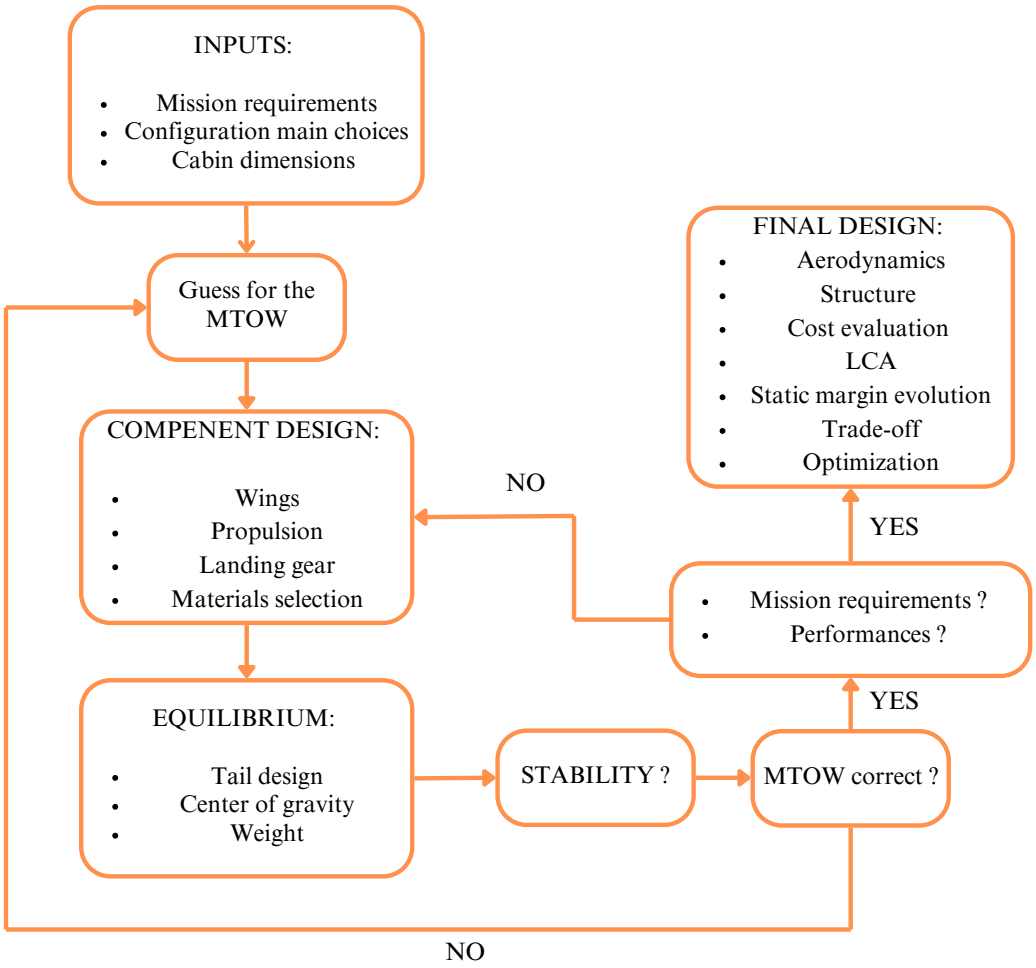

Figure 3.1: Flowchart of the overall design process of LIFT.

The design process begins with a thorough analysis of the mission and regulatory requirements, which informs the selection of a general aircraft configuration. A review of existing business jets and conceptual blended wing body (BWB) designs is conducted to establish initial estimates and benchmarks for subsequent design computations.

To arrive at an optimized configuration that satisfies all mission and performance criteria, an iterative design approach is employed. The process is decomposed into multiple sub-problems, each addressing a specific aspect of the aircraft's design, and solved sequentially while maintaining consistency across disciplines.

The methodology starts by defining the cabin dimensions to ensure a spacious and comfortable interior, aligned with premium customer expectations. Next, using references from existing aircraft concepts, an initial estimate of the maximum takeoff weight (MTOW) is established. This estimate enables the determination of preliminary wing-body geometric parameters. Then, suitable airfoils for the BWB configuration are selected based on aerodynamic performance.

Subsequently, engines are selected and landing gear are designed to meet thrust and efficiency requirements. Additionally, the center of gravity position can be approximated. With propulsion and center of gravity position defined,

equilibrium equations are solved to support tail design. If the assumed MTOW proves consistent through these computations, aircraft performance and stability are evaluated to validate the preliminary design.

Upon validation, the configuration is further refined and analyzed in greater detail across aerodynamics, structural layout, and cost estimation. The resulting design defines LIFT as a balanced solution—stable, aerodynamically efficient, and compliant with all specified constraints.

This methodology, summarized in Figure 3.1, is inspired by the systematic approach described by E. Torenbeek [9].

Chapter 4. Configuration

4.1 Brief history of the concept

The selected configuration for LIFT design is the Blended Wing Body (BWB). This concept emerges from the observation that conventional tubular aircraft feature distinct components: wings generate lift, while engines, tail surfaces, and the fuselage contribute to drag and structural weight, limiting overall performance. In contrast, a flying wing eliminates these separate components, integrating them into a single lifting surface. This design maximizes lift, minimizes drag, and enhances aerodynamic efficiency. Since the fuselage itself provides lift, the structural weight is reduced, leading to lower fuel consumption and increased range.

The idea of a flying wing was pioneered by John K. Northrop [10]. During World War II, the U.S. Army sought a long-range bomber capable of reaching Europe, leading to a contract with Northrop for development. The first operational prototypes, the XB-35 (powered by piston engines) and the YB-35 (powered by jet engines), faced stability and reliability challenges. This led to the development of the YB-49, available in Figure 4.1a, with proposals for a civilian airliner variant. In the 1980s, Northrop, under a classified U.S. military program, developed the famous B-2 Spirit stealth bomber, which is represented in Figure 4.1b.

(a) Northrop YB-49 airliner concept [11].

(b) Northrop B-2 Spirit stealth bomber [12].

Figure 4.1: Northrop flying wing aircraft.

In recent years, the BWB concept has gained renewed interest from aerospace manufacturers and agencies, including Airbus, Boeing, and NASA. JetZero, in collaboration with the U.S. Air Force, NASA, and the FAA, is currently developing a BWB aircraft aimed at achieving a 50% reduction in fuel burn and emissions while maintaining 100% compatibility with Sustainable Aviation Fuel (SAF) [13]. Some of these aircraft concepts are shown in Figure 4.2. The JetZero BWB design offers several advantages, including a wider cabin, an optimized interior layout enabling faster boarding for commercial airliners, and reduced noise due to engine placement on the upper fuselage. Some airline companies, such as United Airlines, have recently announced a conditional agreement providing a path to purchase up to 200 JetZero aircraft [14].

(a) Airbus ZEROe concept aircraft [15].

(b) NASA and Boeing X-48 [16].

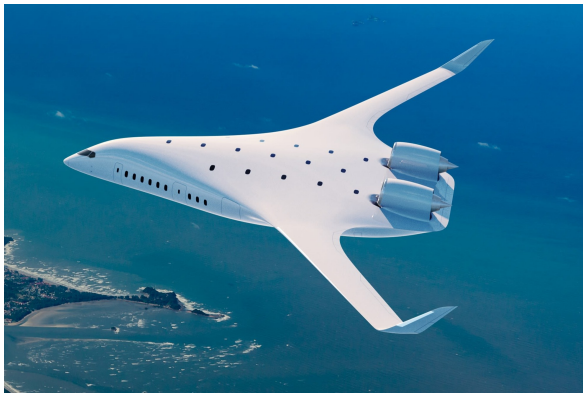

(c) Jetzero BWB concept [13].

(d) Jetzero BWB interior layout [13].

Figure 4.2: Examples of BWB concepts.

4.2 Aircraft configuration

While BWB aircraft offer significant environmental benefits, the primary motivation for selecting this configuration for LIFT is the optimization of the cabin space. Conventional tubular fuselages impose spatial limitations due to the necessity of a central galley for movement, restricting interior layouts to a linear arrangement. In contrast, the wider cabin of a BWB allows for greater flexibility in space utilization, enabling a more customisable interior tailored to passenger needs. This design enhances onboard comfort, offering to the customers a more spacious and home-like environment compared to the constrained layout of a traditional cylindrical fuselage. Moreover, this innovative configuration, still unprecedented in the business jet sector, opens up new opportunities by improving both performance and environmental sustainability.

However, this configuration presents major challenges in terms of static and dynamic stability. It typically has limited control authority and demands sophisticated flight control systems. Additionally, the reduced number of windows in the cabin may potentially diminish passenger comfort. Furthermore, its non-cylindrical configuration introduces some challenges for pressurization. It can cause also some problems about emergency evacuations [17, 18].

Furthermore, as Okonkwo highlights [19], all existing BWB concepts have large wingspans. Therefore, meeting the 95 ft wingspan constraint set for the Aspen mission (Table 2.2) adds another technical challenge for LIFT.

4.2.1 Market analysis

To assess LIFT's position in the market, a brief analysis is conducted of three relatively new long range business jets with conventional configurations, as no BWB aircraft currently exist in this segment. The Gulfstream G700 and Bombardier Global 7500 were introduced in 2024 and 2019, respectively, while the Dassault Falcon 10X is expected to enter service by the end of 2025. The selected aircraft and their prices are presented in Table 4.1. Geometric characteristics and performance metrics are presented in Tables 4.2 and 4.3, respectively [20–23]. The figures for these aircraft are based on publicly available data and are sometimes expressed as ranges due to proprietary restrictions on exact cost values.

Business jet	Unit price [$]	DOC [$/nm]	Max passengers	Cruise Mach [-]
Gulfstream G700	80,000,000	4.5	up to 19	0.925
Bombardier Global 7500	78,000,000	4.3	up to 19	0.85
Dassault Falcon 10X	75,000,000	4	up to 19	0.925
LIFT	66,461,123	4	8	0.9

Table 4.1: Non exhaustive list of several business jets and their main characteristics for the market analysis. DOC stands for Direct Operating Cost.

The maximum passenger capacity of the selected jets is more than double that required by AIAA. However, this figure does not reflect the number of actual seats available in typical cabin configurations, which often prioritize luxury and space. All aircraft listed operate in the transonic regime, aligning with the intended cruise profile of LIFT.

Business jet	Wingspan [ft]	Max cabin height [ft]	Cabin width [ft]
Gulfstream G700	103	6.3	8.2
Bombardier Global 7500	104	6.17	8
Dassault Falcon 10X	110	6.67	9.1
LIFT	94.98	8.1	29.17

Table 4.2: Non exhaustive list of several business jets and their main geometrical characteristics for the market analysis.

The wingspans of the three reference jets exceed the 94.98 ft constraint imposed by the Aspen mission, making them unsuitable under those limitations. Additionally, their cabin dimensions, while luxurious, do not allow for the creation of a true home-like space. In contrast, LIFT addresses this gap by offering a significantly wider and taller cabin, thus providing a unique and spacious onboard experience for customers seeking both innovation and comfort.

Business jet	Range [nm]	Takeoff distance [ft]	Landing distance [ft]
Gulfstream G700	7,500	6,250	2,570
Bombardier Global 7500	7,500	5,760	2,237
Dassault Falcon 10X	7,500	5,930	2,470
LIFT	8,000	4,483.1	3,093.88

Table 4.3: Non exhaustive list of several business jets and their main performance for the market analysis.

All three reference jets achieve a maximum range of 7,500 nautical miles, which falls short of the AIAA range requirement discussed in Chapter 2. In contrast, LIFT's extended range of 8,000 nm positions it as a superior option for ultra-long-range missions.

While all reference aircraft meet the takeoff distance requirement for the Aspen mission, LIFT surpasses them with a significantly shorter required takeoff distance. However, its landing distance is slightly longer than those of the other jets, though still within acceptable operational margins.

Following this market overview, Section 9 compares directly LIFT's characteristics with those of the reference jets discussed here.

4.3 Design choices

The primary goal of LIFT is to cruise at high speeds within the transonic regime to enable rapid completion of long-range missions. However, due to aerodynamic, geometric, and stability considerations, the cruise Mach number is limited to 0.9. As the quarter-chord sweep angle increases with higher Mach numbers, stability concerns arise at $M = 0.92$ due to the relative positions of the aerodynamic center, neutral point, and center of gravity. These issues will be discussed further in Section 6.3. Additionally, a Mach number of 0.9 helps mitigate compressibility effects, as outlined in Section 6.2.1.

To comply with Aspen mission constraints, the wingspan of LIFT is fixed at 94.98 ft, as specified in Table 2.2.

The cruise altitude is set at 41,010.5 ft, a value typical for business jets. Operating at this altitude enables LIFT to fly above most commercial air traffic [24].

4.4 Operational capabilities and operation standards

To ensure LIFT's adaptability across various meteorological conditions, the aircraft is designed to operate under both Visual Flight Rules (VFR) and Instrument Flight Rules (IFR). This compliance is achieved through adherence to equipment and operational standards specified in FAA FAR Part 91.205 and Part 25 Subparts B and C [4, 25]. Additionally, LIFT meets international standards as defined by ICAO Annex 6 [26], ensuring global operational viability.

VFR operations require only basic flight instrumentation. In contrast, IFR operations necessitate more sophisticated avionics, including communication systems, redundant standby instruments, an uninterrupted power supply, and a reliable navigation system. These systems are essential for ensuring airworthiness under both favorable weather conditions (VFR) and low-visibility scenarios (IFR).

4.5 LIFT CAD

Figures 4.3, 4.4, and 4.5 present different views of LIFT, including its main dimensions.

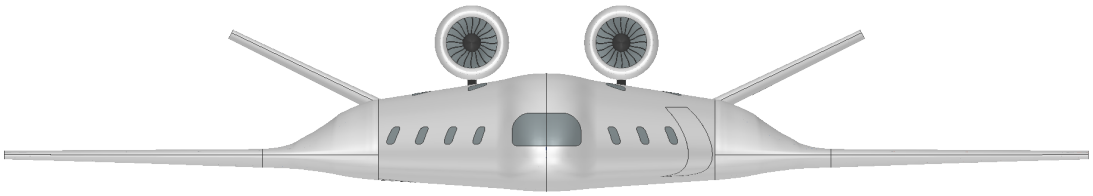

Figure 4.3: Front view of LIFT.

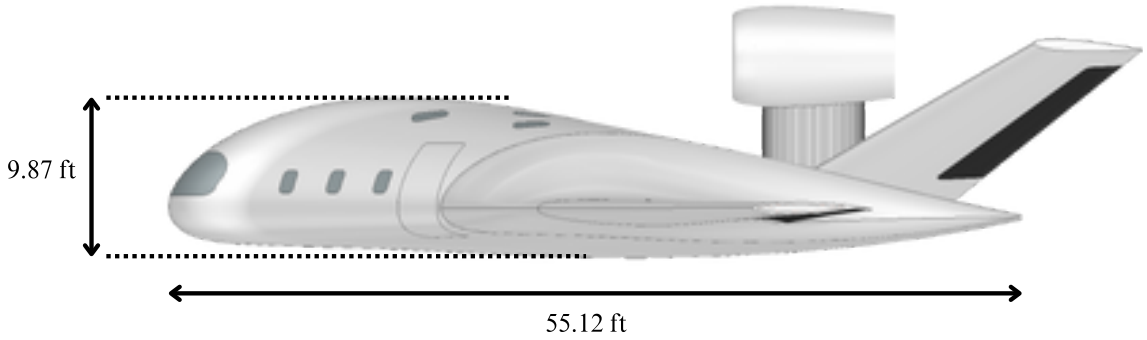

Figure 4.4: Side view of LIFT with the maximum inner wing height.

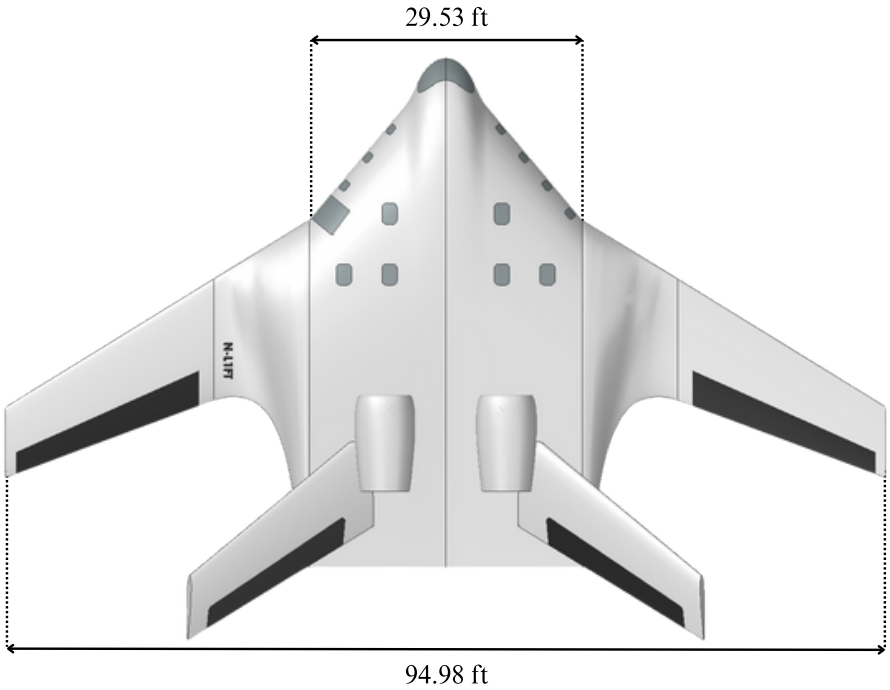

Figure 4.5: Top view of LIFT with the span and cabin width.

Chapter 5. Component Design

5.1 Wings

In this part and for the rest of the report, the wing associated to the inner airfoil section, comparable to the fuselage for a classical configuration, is called the inner wing. The outer airfoil section wing, associated to the wings for a conventional aircraft, is called the outer wing, as shown in Figure 5.1.

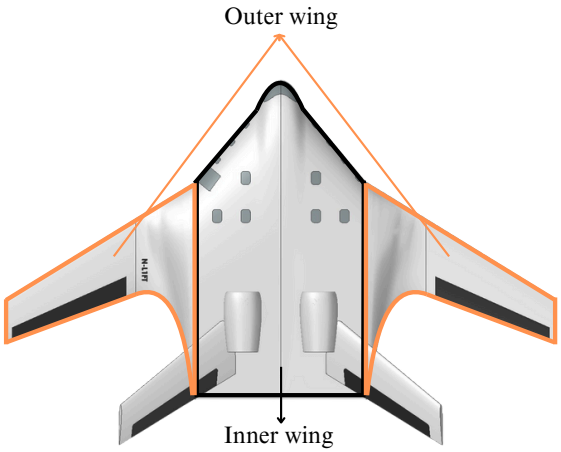

Figure 5.1: Identification of the inner and outer wings of LIFT.

The lift coefficient C_L is set to 0.45 and will be a direct cause of the definition of areas, as explained in Section 5.1.2.

5.1.1 Airfoil selection

The airfoil selections for the wings are based on the operational requirements, such as business jet application and cruise Mach number. Moreover, each airfoil must generate enough lift while minimizing drag.

The outer wing, which is not required to have a certain thickness, must be adapted for high speed, since LIFT flies at M = 0.9. Therefore, a supercritical airfoil, included in the NASA's SC(2) series of airfoils, is considered [27]. The outer wing should maximize lift generation while minimizing its inherent tendency to produce a nose-down pitching moment. Thus, there is a trade-off between both quantities and the SC(2)-0710 airfoil, which is represented in Figure 5.2b, is selected. Nevertheless, this airfoil exhibits a significantly negative pitching moment coefficient, indicating a strong nose-down pitching tendency. This requires the inner wing airfoil to generate a nose-up pitching moment, in order to achieve equilibrium and stability, which are discussed in Sections 6.4 and 6.3.

Additionally, regarding the inner wing, the thickness is a particularly important parameter, since the cabin must be tall enough to accommodate passengers. Therefore, the reflex NACA 45118 airfoil, represented in Figure 5.2a, is chosen. This type of airfoil features a distinctive double camber, which helps to minimize the inherent moment. Nevertheless, it produces lower lift than supercritical airfoils. This wing section choice is discussed in Section 7.

(a) Reflex NACA 45118 airfoil used for the inner wing.

(b) Supercritical Sc(2)-0710 airfoil used for the outer wing.

Figure 5.2: Representation of selected airfoils for the outer and inner wings.

Table 5.1 presents the main aerodynamical coefficients of both airfoils. The polars of the airfoils are extracted from the *BigFoil* database [28]. This database is based on simulation results obtained with *XFOIL* and *JavaFoil*. Both are potential flow solvers that also model the boundary layer, according to Drela [29] and Hepperle [30]. The values in Table 5.1 come from *JavaFoil*, that accounts for compressibility effects at moderate Mach numbers. These assumptions may introduce uncertainties that must be carefully taken into account.

Parameter	Value
Inner wing airfoil lift coefficient derivative [rad^{-1}]	5.641
Outer wing airfoil lift coefficient derivative [rad^{-1}]	6.681
Inner wing airfoil pitching moment coefficient [-]	0.01
Outer wing airfoil pitching moment coefficient [-]	-0.143

Table 5.1: Lift curve slopes and pitching moment coefficients of airfoils for both inner and outer wings [28].

5.1.2 Wing planform

In order to have a home-like cabin interior, the length and width of the inner wing are set to 55.12 ft and 29.53 ft, respectively. Moreover, its sweep angle at the leading edge is fixed to 50°, as explained later. This leads to an inner wing total area of 1367.77 ft^2.

As for the outer wing area, it is a direct consequence of the reference surface. This reference surface, defined as proposed by Panagiotou et al. [31], is represented in orange in Figure 5.3. It represents the surface defined by the wings and their inboard extension up to the fuselage centerline.

After the computation of the lift force thanks to the equilibrium equations in the pitch plane described in Section 6.4, the reference area can be calculated from the definition of the lift coefficient. Consequently, the reference area S_{ref} can be determined and is equal to 1281.44 ft^2. Besides, according to Gundmundsson [32], the taper ratio of the reference area is fixed to 0.4. Since the span equals 94.98 ft due to a mission requirement, the geometry of this surface is known. Then,

using the cabin and reference area dimensions, the geometry of the outer wing can be directly deduced. The latter is equal to 765.42 ft^2. Both inner and outer wings surfaces lead to a LIFT's total surface of 2133.08 ft^2. As a consequence of it, the aspect ratio AR equals 7.04.

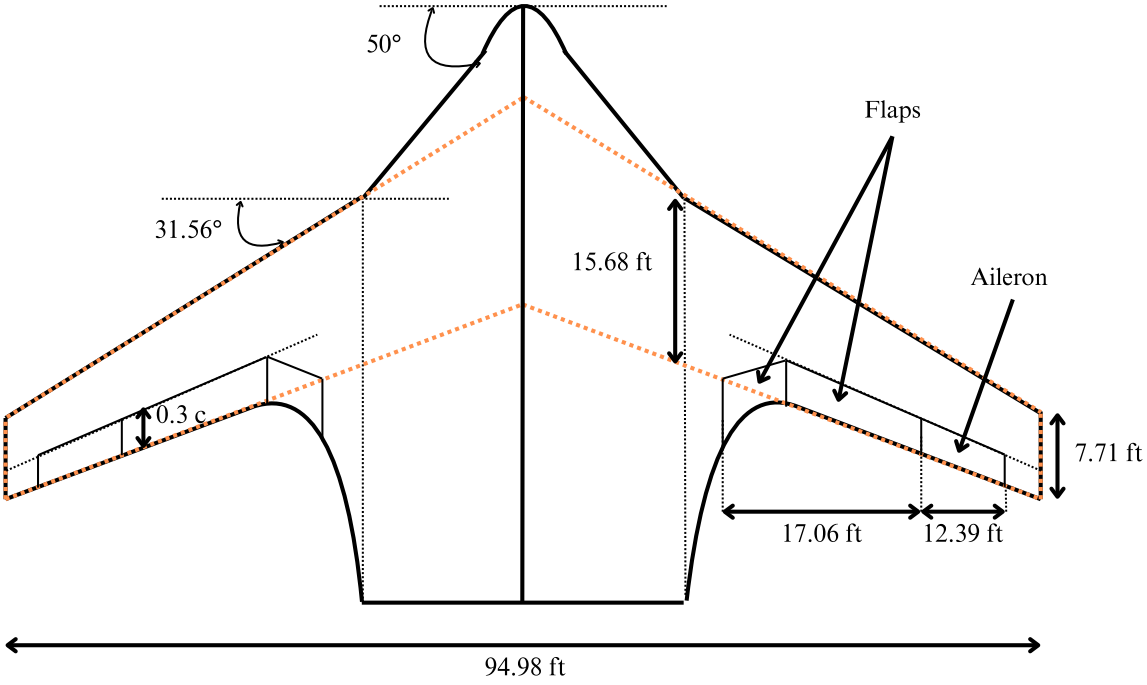

Figure 5.3: Wing planform representation of LIFT with main dimensions.

In order to improve the behavior of the wings at transonic speed, the sweep angle at the quarter chord of the outer wing must be determined from:

$$\Lambda_{c/4} = \cos^{-1} \frac{M_{\text{crit}}}{M_{\text{c}}}. \tag{5.1}$$

where M_{crit} is the critical Mach number of the airfoil and M_{c} the Mach number at cruise.

The critical Mach number of the airfoil of 0.79 (Harris [33]) of the outer wing leads to a minimum outer wing sweep quarter of 28.6°. However, flying with a sweep angle at the quarter chord slightly higher than the one computed from Equation 5.1 provides an aerodynamic safety margin, which allows to avoid strong shock waves, drag increase or even lift instabilities. Therefore, the sweep quarter of the outer wing is set to 29°. This leads to an outer wing leading edge angle of 31.56°.

Nevertheless, because of the lack of information about the critical Mach number for the NACA 45118 airfoil, the sweep angle at the quarter chord of the inner wing cannot be determined from Equation 5.1. Consequently, the leading edge sweep angle of the inner wing is rather first determined, according to a value given by Okonkwo and May-Fun et al. [19, 34] for similar reflex airfoil types. This leads to a leading sweep angle of 50° and a sweep angle at the quarter chord of 41.71° for the inner wing.

The inner taper ratio is geometrically determined by its length, width, and sweep angle, and equals 0.681. The outer wing taper ratio is also a consequence of its geometry and is equal to 0.492, which is validated by a range provided by Gudmundsson [32]. As a result of the geometry, outer wing root chord and tip chord are equal to 15.68 ft and 7.71 ft,

respectively.

To improve controllability and recovery performances in stall, the outer wing is twisted by an angle of -2.63°, which is the optimal value advised by Gudmundsson [32]. In order to generate enough lift, the angle of attack of the outer wing is equal to 0.8°, while the one of the inner wing is set to 0°. The angle of attack establishment is done in Section 6.2.1. Additionally, LIFT does not require a dihedral angle for the outer wing, as it will be verified in Section 6.3.2.
Table 5.2 and Figure 5.3 summarize the geometrical parameters of the wing planform.

The lift curve slope and the zero lift angle of LIFT are determined in Section 6.2.1.

Parameter	Value
Inner wing area [ft^2]	1367.77
Outer wing area [ft^2]	765.42
Reference area [ft^2]	1281.44
Total lifting surface [ft^2]	2133.19
Aspect ratio [-]	7.04
Taper ratio inner wing [-]	0.681
Taper ratio outer wing [-]	0.492
Taper ratio of the reference area [-]	0.4
Twist angle [°]	-2.63
Setting angle of the inner wing [°]	0
Setting angle of the outer wing [°]	0.8
Mean aerodynamic chord [ft]	35.97
Design lift coefficient [-]	0.45
Lift curve slope [rad^{-1}]	6.596
Zero-lift angle [°]	-3.9

Table 5.2: Summary of the main geometric and aerodynamic properties of LIFT wing planform.

5.1.3 High lift devices

Flaps

The maximum lift coefficient required during takeoff and landing phases is 2.1. Following the reverse methodology described by Raymer [35], it is possible to determine the high lift device that is consistent with this aircraft configuration.

Because the wings are small and the cabin takes all the volume at the front of the inner wing, leading-edge devices are not considered.

As defined by Raymer [35], the maximum lift coefficient can be computed as:

$$C_{L\max} = (C_{L\max})_{\text{clean}} + \Delta C_{L\max}, \tag{5.2}$$

where $(C_{L\max})_{\text{clean}}$ represents the maximum lift coefficient when the flaps are not deflected, i.e. $\delta_f = 0°$. $\Delta C_{L\max}$ is computed using the following equation:

$$\Delta C_{L\max} = \Delta C_{l\max} \left(\frac{S_{\text{flapped}}}{S_w} \right) \cos \Lambda_{HL}. \tag{5.3}$$

The parameter Λ_{HL} represents the sweep angle of the hinge line, which is positioned at 30% of the chord length of the outer wing. The surface area $S_{flapped}$ corresponds to the wing section equipped with rear-mounted flaps.

Based on the calculations and design guidelines provided by Raymer [35], single-slotted flaps are selected to achieve a $\Delta C_{l\max}$ of 1.406. A summary of the relevant control surfaces parameters is presented in Table 5.3. Additionally, the flaps are shown in Figure 5.3.

Parameter	Value
Maximum lift coefficient flapped [-]	2.1
Maximum lift coefficient clean [-]	1.329
Delta maximum lift coefficient [-]	1.406
Sweep angle of hinge line [°]	23.98
Flapped surface [ft^2]	459.25

Table 5.3: Summary of main values linked to high lift devices.

Ailerons

Following the guidelines provided by Raymer [35], the ailerons are positioned between 50% and 90% of the wingspan. To ensure consistency with the flap dimensions, the aileron-to-wing chord ratio is set to 0.3. According to a chart provided by Raymer [35], the aileron's span is defined as 12.39 ft, corresponding to the available distance between the end of the flaps and 90% of the wingspan. The maximum deflection angles are set to 25° upward and 20° downward. The ailerons are pictured in Figure 5.3.

5.2 Inner wing layout

5.2.1 Inner wing shape

The inner wing layout is directly dependent on its shape by the choice of its airfoil. As said in Section 5.1.1, the choice of the NACA 45118 reflex airfoil model with a thickness to chord ratio up to 18% is made to ensure sufficient height on the front of the plane to fit a minimum head clearance of 5.58 ft.

5.2.2 Inner wing geometry

The following dimensions in Table 5.4 are stated as a trade-off to ensure the habitability and aerodynamic performance of the inner wing.

Parameter	Dimension [ft]
Cabin length	40.06
Cabin width	29.53
Inner wing length	55.12
Inner wing width	29.53

Table 5.4: Cabin and inner wing dimensions.

It allows to have a 850.35 ft^2 cabin available for the customers. The inner wing part that is not occupied by the cabin is called the AFT part, which represents 27.32% of the total length of the inner wing. The engines, discussed in Section 5.4, and the tail, discussed in Section 5.3, are placed on the top of this part.

5.2.3 Cabin layout

The layout of passenger accommodation (LOPA) is represented in Figure 5.4, where all the rooms and places of the inner wing are listed. Several dispositions can be noted, including the designed component required by the AIAA specifications. The galley takes the shape of a bar with sufficient storage capacities in respect to the mandatory consumable payload. The luggage compartment directly accessible from the cabin can store up to 88 ft^3 of luggage to ensure the storage of the passenger payload. All of this results in a cabin layout focused on customer comfort.

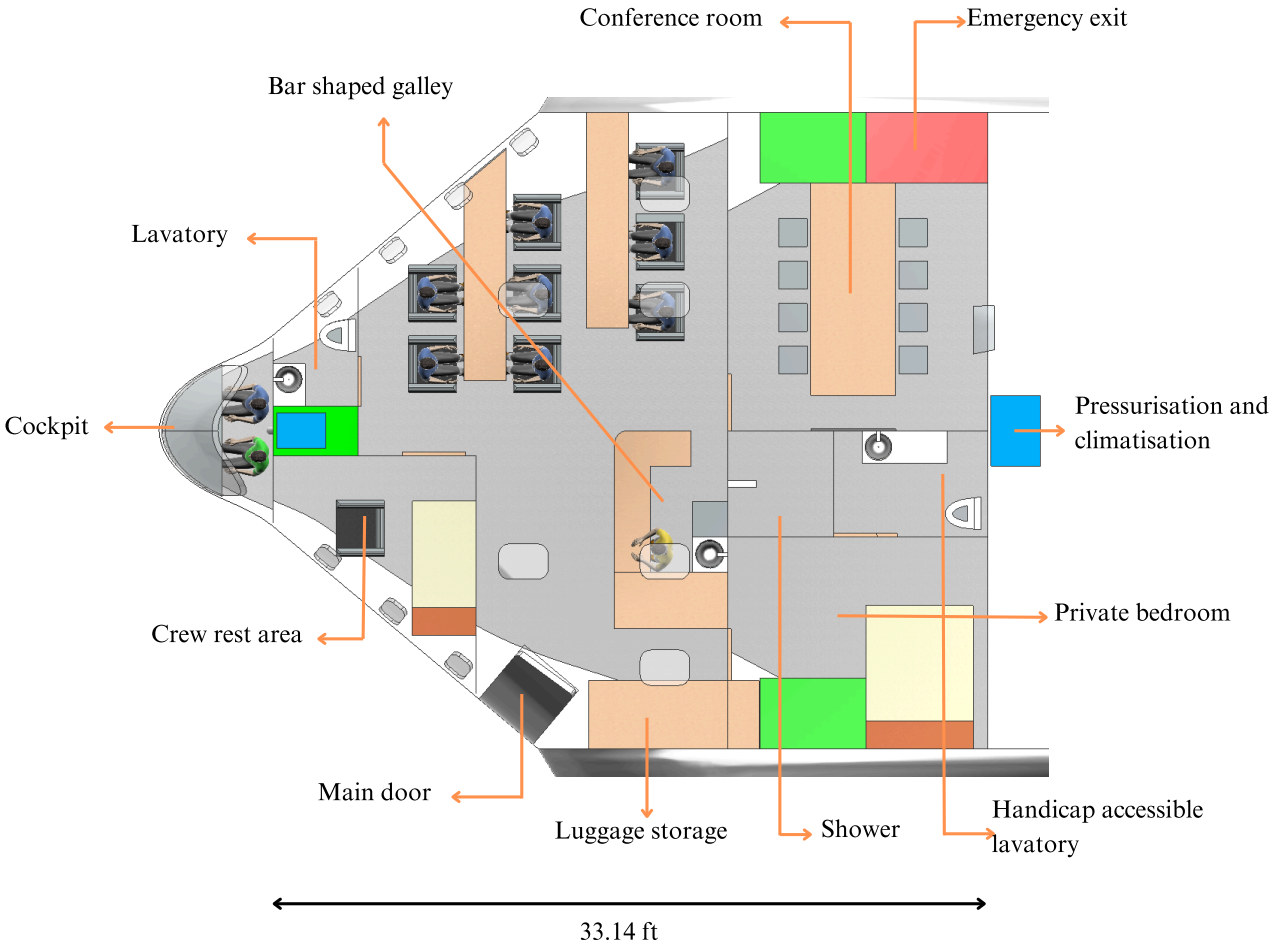

Figure 5.4: LOPA of the LIFT cabin.

The green area in Figures 5.4 and 5.5 represents the landing gear storage area inside the inner wing. Above the rear landing gear storage area, emergency exits of type *III* overwing allow LIFT to fulfill the emergency exit standard of FAA Part 25 requirements [25]. An additional large ventral exit of 5.6 by 3.3 ft present in the conference room can ensure a better exit experience if the integrity of the landing gear can allow a safe exit.

The cabin, which measure 850.35 ft^2, has a wide and home-like main room of 398.99 ft^2. This main room contains 8 seats and the bar shaped galley. This huge area allows a free displacement of the customers in all the direction. They are

not restricted as within a classical configuration of business jets. That is one of the main advantages of the LIFT's cabin. In this main room, the maximum height is 8.1 ft, which strengthens this feeling of an impressive large space. Additionally, there is a 161.61 ft^2 meeting room, which allows all the customers to meet around a table if needed. Just next to it, the 102.36 ft^2 bedroom that offers a pleasant place for the customers to rest thanks to its king-size bed. Moreover, LIFT is equipped with one handicap accessible lavatory, which measures 59.25 ft^2, which allows LIFT to be adapted for all types of customers.

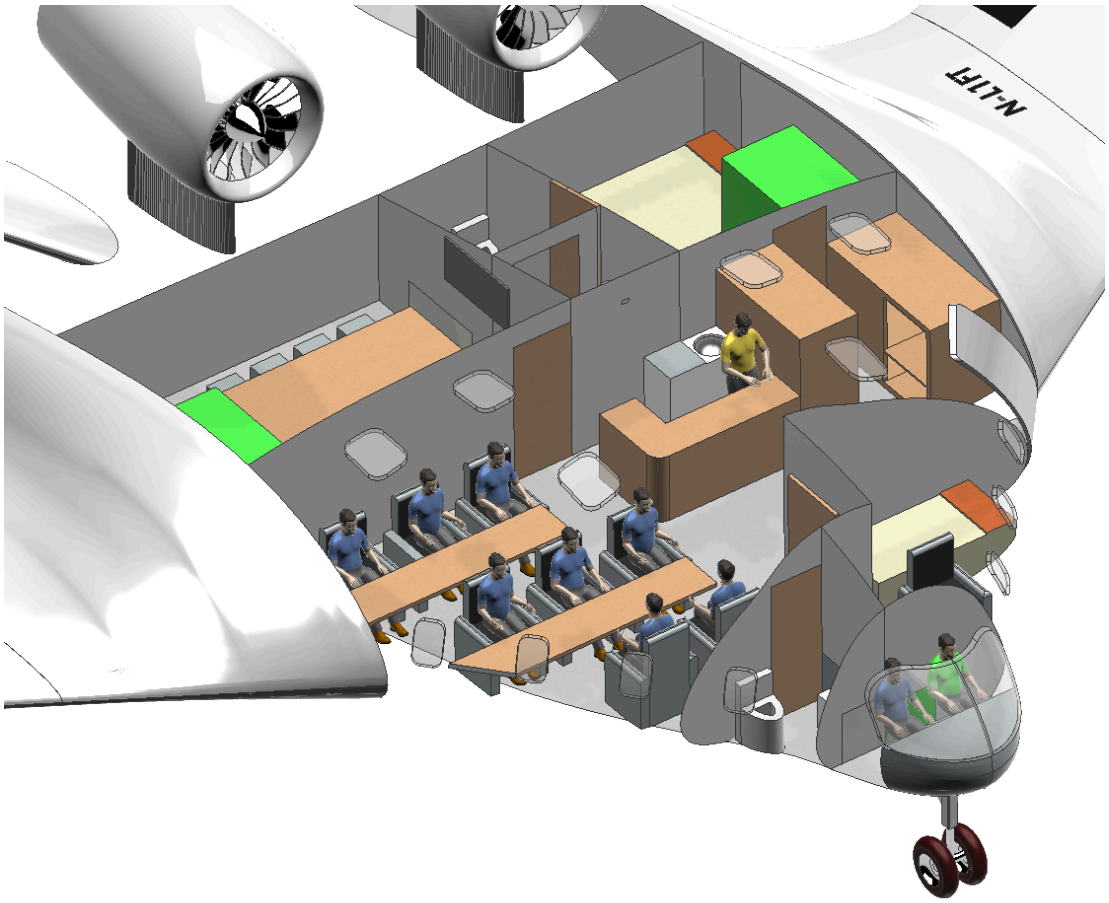

Figure 5.5: Overview of the LIFT cabin layout.

5.3 Tail

The LIFT's tail configuration is a V-tail. This type of configuration can be decomposed into horizontal and vertical components, as for a conventional tail, Gudmundsson [32]. Those parts are build separately, before being assembled by a theoretical method given by Roskam [36] to form the final geometry of the V-tail.

Starting from both rotational and translational static equilibrium equations in the pitch plane described in Section 6.4, the force that the horizontal tail must support to achieve trim conditions is determined. Additionally, static and dynamic stability, that are discussed in Section 6.3, require both horizontal and vertical contributions from the empennage.

According to Gudmundsson [32], the V-tail possesses advantages compared to a classical tail configuration, such as higher performance at landing and takeoff, a lower interference drag, or a lower total area. Raymer [35] mentions also

that the V-tail configuration reduces the wetted area and the weight, compared to a conventional configuration. However, the V-tail requires more complex mechanisms concerning the control surfaces. This is discussed later in Section 5.3.4.

5.3.1 Airfoil selection

As the center of gravity and aerodynamic center vary throughout the flight, the tail may be required to generate force in either direction. To ensure effectiveness across all conditions, a symmetric airfoil is selected, which is advised by Torenbeek [9].

Besides, it must have a reduced thickness for purposes of lower generated drag and higher critical Mach number than the outer wing [35]. This implies the selection of the NACA 0012 airfoil, represented in Figure 5.6. It has no camber and its maximum thickness is located at 12% of the chord length from its leading edge [37].

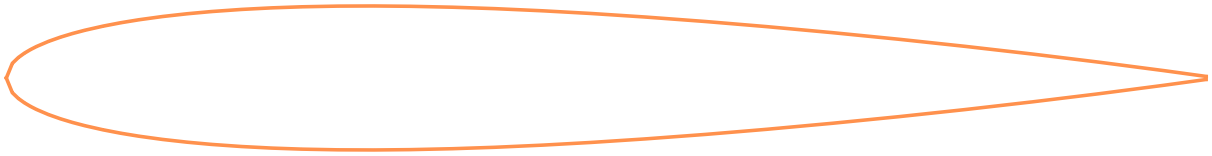

Figure 5.6: NACA 0012 used for the V-tail.

5.3.2 Tail planform

The surface area of the horizontal tail is set to 376.74 ft^2, as a consequence of longitudinal static stability requirements, discussed in Section 6.3.2, and equilibrium, discussed in Section 6.4. However, the vertical tail, sized from directional and lateral stability requirements, must equal 204.51 ft^2. This leads to a total surface of 428.67 ft^2, which represents 20.1 % of the total area of the aircraft.

In order to minimize its span, the root chord of the tail is set to 11.48 ft. However, to reduce weight, the taper ratio is set to 0.6, which is an acceptable value for business jets, as presented by Gudmundsson [32].

The spans of the horizontal and vertical parts of the tail are 41.01 ft and 22.26 ft, respectively. Therefore, the horizontal tail has an aspect ratio of 4.46, while the one of the vertical contribution is 2.42. These AR values are confirmed by Raymer [35]. Thus, the total span and aspect ratio are 93.32 ft and 5.08, respectively. Consequently, the dihedral angle is equal to 28.5 °, according to a formula given by Roskam [36]. The spans and angle are shown in Figure 5.7.

The sweep angle at the quarter chord is defined based on that of the outer wing. Since the tail must stall after the outer wing, the critical Mach number of the tail must be higher than the one of the outer wing. This implies that the sweep angle at the quarter chord of the tail has to be higher [9]. Therefore, an increase of approximately 5° compared to the outer wing is selected and the quarter-chord sweep angle is 34.89° [35]. Furthermore, it allows to avoid shock waves.

5.3.3 Lift coefficient and incidence angle

The lift coefficient of the tail is given by:

$$C_{L_T} = C_{L_{\alpha_T}} \left(\frac{CL_w}{C_{L_{\alpha_w}}} \left(1 - \frac{\partial \varepsilon}{\partial \alpha} \right) + \eta_T + \alpha_{L_0,root} \right), \tag{5.4}$$

where η_T is defined as the difference between the tail incidence angle i_T and the one of the outer wing i_w.

The lift curve slope of the tail is computed from a formula given by Torenbeek [9] and equals 2.75 rad^{-1}.

The downwash effect term $\frac{\partial \varepsilon}{\partial \alpha}$ is estimated from an approximation given by Gudmundsson [32] such that:

$$\frac{\partial \varepsilon}{\partial \alpha} = \frac{2C_{L_{\alpha_w}}}{\pi AR}, \tag{5.5}$$

where $C_{L_{\alpha_w}}$ is the lift curve slope of the aircraft. Thus, this term equals 0.59. Additionally, the lift coefficient C_{L_T} is equal to -0.2 at cruise.

Since the tail airfoil is symmetric, $\alpha_{L_0,root} = 0$, which leads to an incidence angle i_T of -0.1° for the tail.

5.3.4 Control surfaces

For a V-tail configuration, the rudders and the elevators are mixed into a single control surface known as the ruddervator, which allows both pitch and yaw control [32]. The sizing of the surface can be performed using the method proposed by Raymer [35] for rudder design.

As LIFT flies at high transonic speed, the ruddervator starts at the side of the fuselage and extends to about 50% of the tail span, instead of 90% for lower cruise speed aircraft. Besides, it is tapered in chord as the tail surface, with a taper ratio of 0.6. This configuration allows the control surface to maintain a constant percentage chord. As advised by Raymer [35], the ruddervator typically represents about 45% of the V-tail chord. This high speed aircraft consideration avoids an effectiveness problem similar to the aileron reversal, in which the air loads placed upon a deflected aileron are so great that the wing itself is twisted. At some speed, the wing may twist so much that the rolling moment produced by the twist will exceed the rolling moment produced by the aileron, causing the aircraft to roll in the opposite direction [35]. Table 5.5 and Figures 5.7 and 5.8 summarize the key parameters concerning the tail.

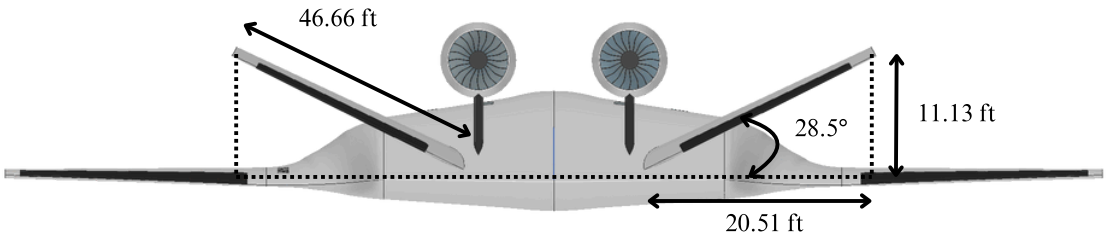

Figure 5.7: Rear view of LIFT to identify tail geometrical parameters.

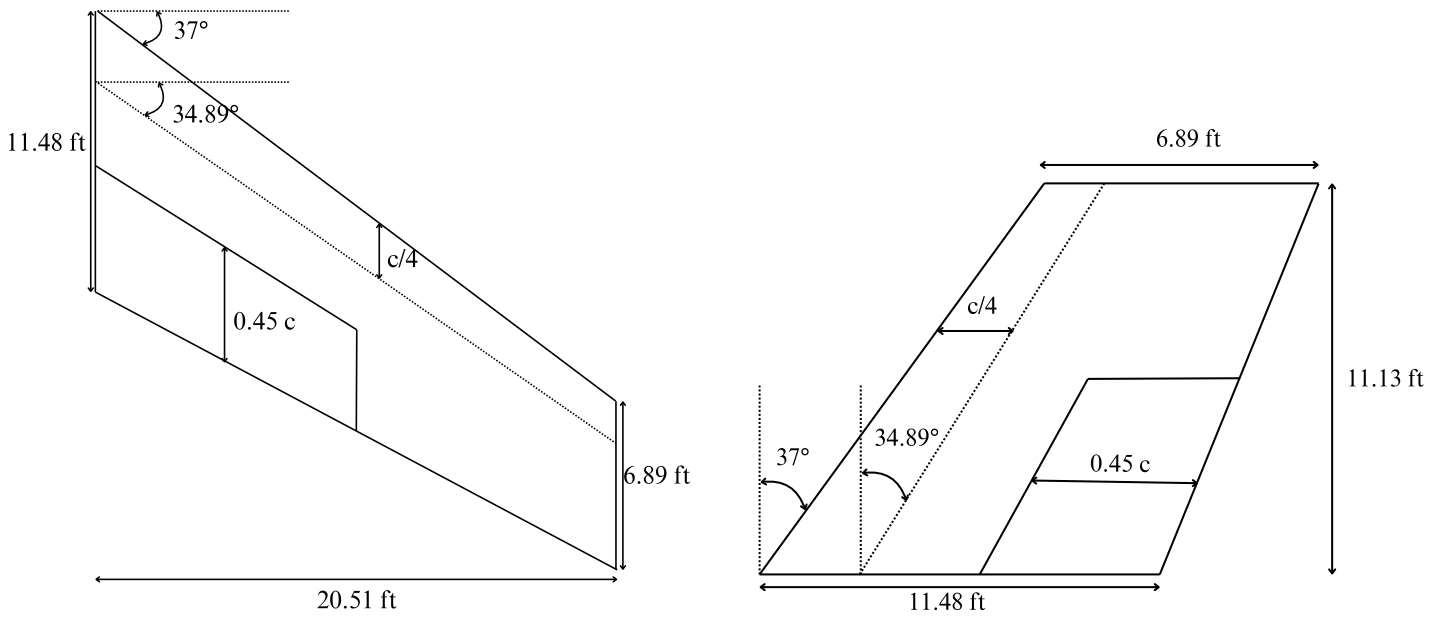

(a) Projection of the V-tail in the horizontal plane.

(b) Projection of the V-tail in the vertical plane.

Figure 5.8: V-tail projections into both horizontal and vertical planes.

Parameter	Value
Horizontal area [ft^2]	376.74
Vertical area [ft^2]	204.51
Total area [ft^2]	428.67
Horizontal AR [-]	4.46
Vertical AR [-]	2.42
Total AR [-]	5.08
Taper ratio [-]	0.6
Mean aerodynamic chord [ft]	8.24
Incidence angle [°]	-0.1

Table 5.5: Summary of the key geometrical parameters of the V-tail.

5.4 Propulsion

The propulsion selection for LIFT is based on the drag coefficients across various flight segments, that are computed in Section 6.2.2. Table 5.6 presents the drag coefficients during takeoff, cruise and landing phases.

	Takeoff	Cruise	Landing
Drag coefficient [-]	0.181	0.0265	0.233

Table 5.6: Summary of the drag coefficients for the takeoff, cruise and landing phases, according from the computations made in Section 6.2.2.

5.4.1 Engine type selection

Due to the aircraft's non-conventional configuration, special attention is given to engine selection to ensure sufficient thrust during cruise to balance drag and provide adequate acceleration capability, especially because there is no exact

quantification about the drag generated by the inner wing airfoil.

Three potential engine types are considered and compared against the mission requirements in Table 5.7.

Type	Thrust-to-Weight Ratio	SFC (lb/lbf·h)	Noise level	Long-range suitability
Turbojet	High (5:1)	High (0.9)	High	Poor
Turbofan	Moderate (4:1)	Low (0.37)	Low	Excellent
Hybrid-electric	Low (2:1)	Very Low	Very Low	Limited

Table 5.7: Comparison of turbojet, turbofan and hybrid-electric engine types, according to Mattingly [38].

Considering the range and efficiency requirements, a high-bypass turbofan engine is selected as the most suitable choice. Furthermore, the decision to use two engines for this aircraft is primarily based on safety and performance efficiency. From a safety perspective, the redundancy provided in the event of an engine failure is a significant advantage. This configuration also complies with the extended twin-engine operations (ETOPS) and the FAA 14 CFR Part 25 [25] airworthiness standards, according to Raymer [35].

This choice is confirmed by Figure 5.9, from where it can be concluded that the turbofan engines are the most suitable selection for transonic Mach numbers.

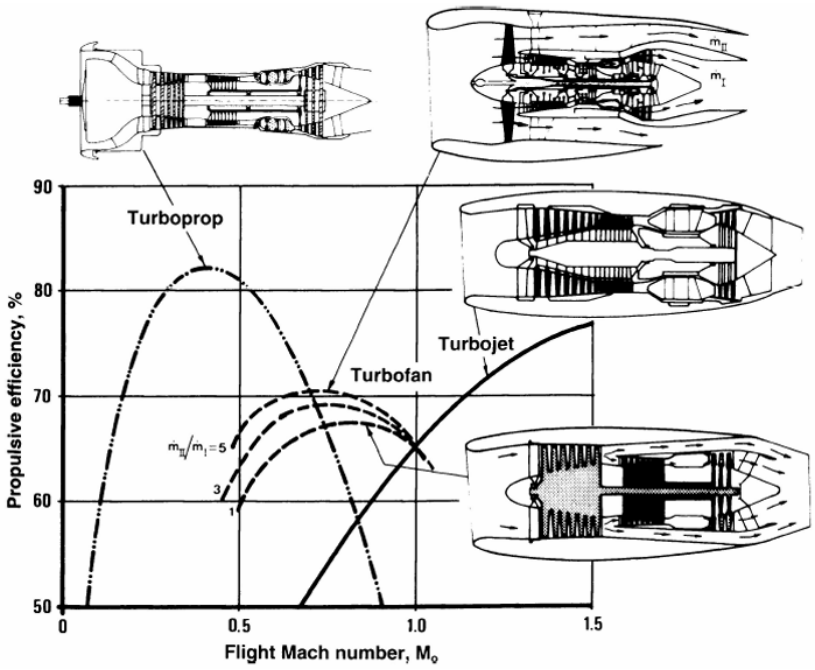

Figure 5.9: Comparison between turbojet, turbofan and turboprop engines in terms of propulsion efficiency as a function of the Mach number [39].

5.4.2 Engines position

The engines are symmetrically placed along the longitudinal axis of the aircraft on elevated pylons, of which the nacelles are angled moderately inward to achieve a balance between structural integration and aerodynamic efficiency. This configuration keeps the engines far from the passengers, thereby minimizing engine noise in the cabin. It also reduces the risk of foreign object ingestion during takeoff and landing. Placing them at the back of the inner wing allows also to reach the trim configuration, described in Section 6.4. Additionally, it gives the advantage of a cleaner airflow over the

top section of the outer-inner wing junction [35]. Furthermore, placing the engines at the top of the fuselage reduces the noise pollution to the environment [35].

Besides, in order to avoid distortion at the inlet of the engines, they are placed at a minimum distance of 3.18 ft from the inner wing structure. This position is discussed in Section 5.4.6.

5.4.3 Engine selection

According to AIAA requirements, the engine must be operationally available by 2035. Having a low TSFC, a high bypass ratio, or high propulsive efficiency, the selected engine is the Pratt & Whitney PW1521G. This choice is discussed in Section 7.2. Table 5.8 presents the essential geometric attributes of the selected engine, as provided by the EASA [40].

Parameter	PW1521G
Overall Length (Flange to Flange) [ft]	9.99
Overall Length (Fan Spinner Face to Aft #6 Comp. Bolt) [ft]	10.45
Nominal Diameter (Fan Case) [ft]	6.58
Max Radial Projection (At Drain Mast) [ft]	3.81
Dry Weight [lb]	4,800

Table 5.8: Main dimensions of the selected PW1521G engine [40].

The available thrust and thrust specific fuel consumption (TSFC) provided in the engine data sheet [40] correspond to static conditions rather than real flight conditions. To obtain the actual in-flight values, the thrust needs to be corrected by accounting for altitude and Mach effects. This is done using the methodology described by Gudmundsson [32]. The actual in-flight values are presented in Table 5.9.

Flight segment	Corrected thrust [lbf]	Corrected TSFC [lb/lbf·hr]
Takeoff	36,449.21	0.6132
Climb	27,480.97	0.6074
Cruise	9,766.48	0.5466
Landing	8,717.35	0.5676

Table 5.9: Corrected thrust and TSFC values of the selected Pratt & Whitney PW1521G engine for each flight segment.

5.4.4 Required thrusts and thrust margins

Following the methodology outlined by Gudmundsson [32], the required thrust needed for efficiently executing each flight phase is computed. By implementing this method for takeoff, an additional acceleration force component is included in order to account for the ground roll distance.

In the climb segment, an initial standard rate of climb assumption of 2000 ft/m is made to calculate the required excess thrust, while ensuring compliance with the FAA part 25 performance regulations [25]. Additionally, the required thrust at cruise is calculated assuming steady, level flight, based on data from the drag estimation [32]. The required thrust for each phase is shown in Table 5.10.

Thrust margins are calculated across all the flight segments using the required and available thrust to confirm the adherence to the FAA part 25 margin regulations [41]. Table 5.10 shows that all the flight segments exceed the required margin. This is primarily because a conservative design decision is taken to minimally oversize the engine due to the complexity of surely knowing the drag of the inner wing. This inner wing drag is discussed in Section 6.2.1.

Flight phase	Required thrust [lbf]	Available thrust [lbf]	Thrust margin [%]
Takeoff	30332.77	36449.21	20.16
Climb	14940.03	27480.97	83.94
Cruise	7287.52	9766.48	34.02

Table 5.10: Thrust requirements and margins for the takeoff, climb and cruise configurations.

5.4.5 Fuel consumption and storage

The total fuel weight and fuel volume are calculated based on the the cruise segment characteristics by using the Breguet range equation as described by Nicolai [42]. A maximum payload range of 8300 nm is assumed, this reflects the target mission profile for ultra long-range business jets and also ensuring that LIFT meets and exceeds the industry expectations. Implementing the Breguet range equation, the useful fuel weight W_f is defined as :

$$W_f = W_d \left(e^{\frac{R \cdot \mathrm{TSFC}}{V \cdot L/D}} - 1 \right) \tag{5.6}$$

where W_d is the dry weight of the aircraft, R is the range [nm] and V is the cruise speed [kt].

To adhere to the FAA safety regulations, a 5% reserve fuel margin is added to account for contingencies that may occur. The sum of the reserve fuel and the useful fuel weight gives the total fuel weight, denoted as $W_{f,\mathrm{total}}$.

Jet A-1 is the standard fuel used in the industry for long-range missions due to its global availability and reliable performance at high altitudes. It has a density of 6.7 lb/gal, consistent with the values reported by Shell and the FAA [43, 44]. It is used to perform the fuel sizing calculations, of which the results are summarized in Table 5.11.

Fuel type	Weight [lb]
Useful fuel	42,217.93
Reserve fuel	2,110.90
Total fuel	44,328.82

Table 5.11: Summary of the values for the useful, reserve and total fuel weights.

The fuel weight and density lead to a corresponding fuel volume of 6,616.24 gallons.

For volumetric optimization and stability purposes, the fuel tanks are located at the leading edge of the transition wing part. They have a volume of 900.52 ft^3, in order to contain all the fuel volume computed for the 8300 nm range mission. Additionally, it allows to store the shower's water and the electrical system underneath the floor of the cabin.

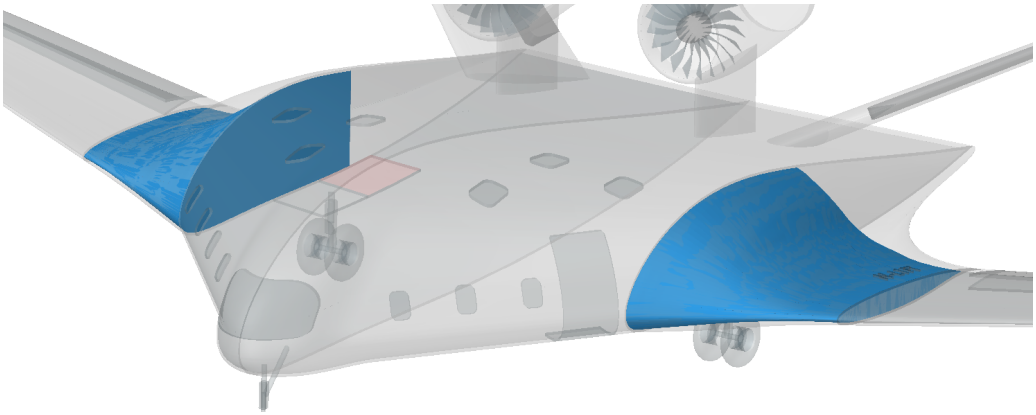

Figure 5.10: Location of the fuel tanks in LIFT.

5.4.6 Boundary Layer Ingestion investigation

A future improvement that could enhance the performance of LIFT is the boundary layer ingestion (BLI) technology. For this purpose, the engines could be placed closer to the inner wing, taking advantage of the distortion produced by the boundary layer [45]. Since, it allows to reduce the specific fuel consumption, it has environmental benefits.

Nevertheless, this technology is not used today because of a lot a problems, e.g. the flow distortion at the engine inlet, that are not solved yet. Additionally, this technology will maybe not be available in 2035, which is one of the requirement from the AIAA, as explained in Section 2.2. This is the reason why LIFT does not have a BLI engine.

5.5 Landing gear

To ensure stability at landing, the choice of a retractable tricycle landing gear configuration is chosen. This configuration is commonly used for most modern business jets [35].

5.5.1 Landing gear position

The position of the landing gear is determined by considering Raymer's [35] method, complemented by Currey's [46], giving different perspective on the method. It is based on the concept of the limit pitch angle of the aircraft, characterized by the tip back angle Θ. According to Daniel P. Raymer [35], this angle is often included within a range from 12° to 15°. Therefore, it is set to 15°, which prevents any possible landing configuration to land safely without impact on the parts of LIFT.

Then, the angle γ between the main landing gear and the most backward position of the center of gravity must at least be greater than Θ to avoid the plane to fall back. Here, those angles are the same.
In order to respect the weight repartition on the front wheels, the fraction of the mass supported by the nose landing gear must be in the range from 8% to 15% to abide 14 CFR 25 regulation [41]. These are margins taken to avoid skidding effect on one hand, and pitch down momentum at takeoff on the other hand.

Finally the lateral position is given by the overturn angle set at $\alpha_{CG} = 45°$, in order to have the landing gear retractable in the fuselage. The resulting configuration is shown in Figures 5.12 and 5.11 with the main geometrical parameters. Moreover, additional geometrical data are listed in Table 5.12.

Parameter	Value
Plane gravity center height [ft]	8.54
Distance between plane gravity center and main landing gear [ft]	8.84
Wing height [ft]	7.03
Overturn angle [°]	38

Table 5.12: Additional information about the landing gear geometrical disposition.

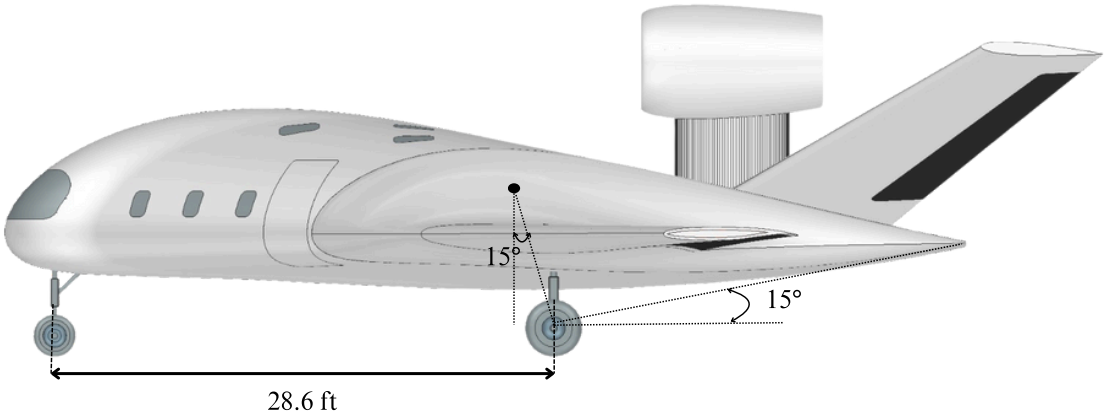

Figure 5.11: Side view of LIFT with landing gear main geometrical parameters.

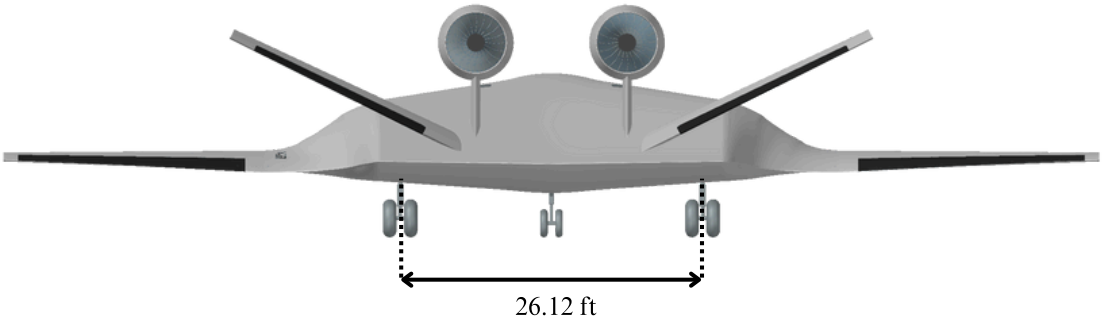

Figure 5.12: Rear view of LIFT with the distance between both main landing gear.

5.5.2 Landing gear design

Once the configuration is established, it is possible to dimension the complete landing gear layout by following Currey's guidelines [46].

Both tires are selected among the type VII catalog of tire manufacturers for the general aviation. Two wheels are placed for each landing gear location. Size relative to the aircraft are displayed, with rolling radius, in Figure 5.12. For the main landing gear, the tire is a 40×14 Aircraft Rib, while it is a 30×8.8 Flight Leader for the nose gear.

A rear braking system is selected on LIFT to sustain high kinetic loads, especially occurring on runway with high braking coefficients. Each wheel has a carbon 4 disc-based braking, with an outer radius of 7.5 in and an inner radius of 3 in to fit in the main gear. This braking system ensure the aircraft to decelerate sufficiently at landing for the aircraft to land easily on a minimal 3858.86 ft runway.

The damping system chosen is a common oleo-pneumatic with a metered orifice for both main and nose gears able to sustain rough landing conditions. Their total length is 25 in with a stroke of 10 in. Outside diameter of the oleo-pneumatic is then deduced with the load on each landing gear with safety factors. They correspond to 10.2 in for the main gears and 8.2 in on the nose gear.

5.6 Materials selection

In recent decades, the aerospace industry has increasingly shifted toward the use of advanced composite materials, driven by the demand for lighter, more fuel-efficient aircraft. To reduce weight while maintaining structural integrity, high-strength, lightweight composites such as molded carbon/epoxy laminates are preferred. These materials are extensively used in modern aircraft, including the Boeing 787 Dreamliner and Airbus A350 XWB demonstrating their effectiveness in primary structural applications such as wings and fuselages [47]. Moreover, composite materials contribute to manufacturing efficiency by reducing the number of assembled components, which can lower production costs [48].

The material selection process is conducted using Granta EduPack Software [49]. For the inner and outer wing structures, carbon fiber-reinforced polymers (CFRPs) are identified as the optimal choice. Specifically, HexPly® M21EV/IMA, developed by Hexcel, is selected due to its excellent mechanical performance and proven track record in aerospace applications. This material is currently employed in the Airbus A350 program, where it is used for components such as fuselage panels, wings, and empennage structures [50, 51]. More recently, it has also been adopted in the construction of the Dassault Falcon 10X business jet [52]. The mechanical properties of HexPly® M21EV/IMA are presented in Table 5.13.

Parameter	Value
Density [lb/in^3]	0.057
Tensile Strength [psi]	442,000
Compressive Strength [psi]	218,000
Shear Strength [psi]	13,600

Table 5.13: Mechanical properties of HexPly® M21/IMA [53].

For components that are subjected to high mechanical loads and require both superior specific strength and fatigue resistance, such as the landing gear, titanium alloys are highly suitable. Among these, Ti-3.5Al-5Mo-6V-3Cr-2Sn-0.5Fe is identified as a particularly promising alloy, offering an optimal balance of mechanical properties [54].

Chapter 6. Aircraft analysis

Once the aircraft design is fixed to meet the requirements, a performance analysis is conducted. For this purpose, different phases of the flight are considered, and the analysis covers various aspects such as aerodynamics, stability, structure, and overall performance.

6.1 Weight and center of gravity

In order to compute the weight of LIFT, the methodology from Okonkwo [19] is adopted. While the same approach is used for most of the components, engine weight is directly obtained from the manufacturer data sheet. Payload weight is determined based on design requirements, which are described in Section 2.1. Regarding the total fuel weight, it is computed from SFC and range, as done in Section 5.4.

The center of gravity positions of all the components are estimated from the geometry of the aircraft, as well as from the cabin layout, which is shown in Section 5.2. Table 6.1 and Figure 6.1 present the weight and center of gravity of all the components. The percentages calculated in Table 6.1 represent the relative position of the center of gravity in the longitudinal direction with respect to the entire length of LIFT, which is 55.12 ft.

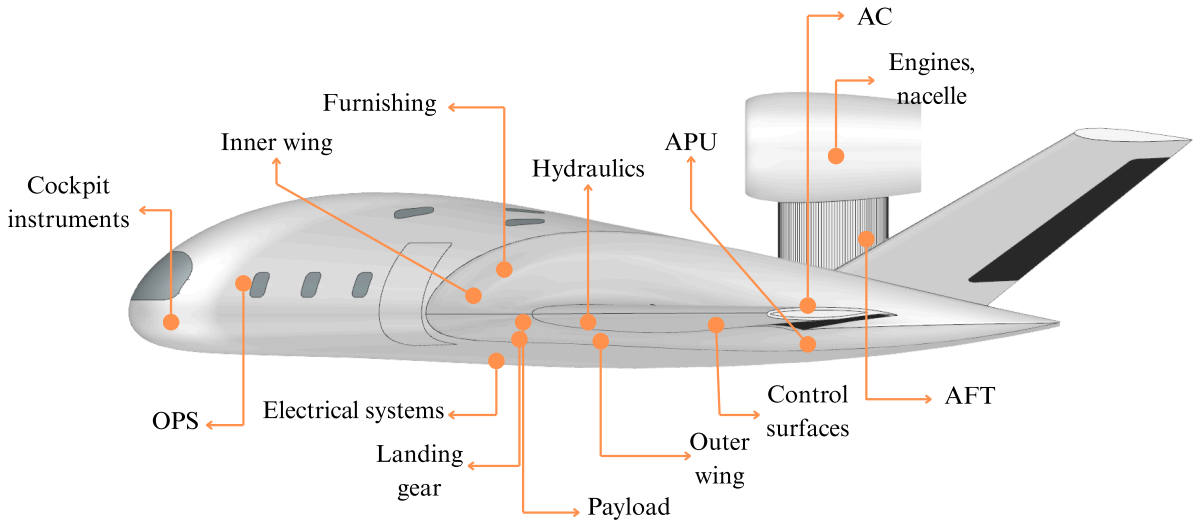

Figure 6.1: Representation of all the centers of gravity on LIFT.

Component	Weight [lb]	Percentage of the total length [%]
Outer wing	10440.98	49.77
Inner wing	11259.29	36.09
AFT	3929.21	80.32
Landing gear	4702.88	41.04
Engines	9598.92	74.06
Nacelle group	4608.05	74.06
APU	105.68	74.49
Cockpit instruments	1332.08	3.59
Hydraulics	1544.39	48.41
Furnishing	5201.71	39.4
Air conditioning (AC) and anti-icing	1955.7	71.49
Electrical systems	2261.54	38.55
Control surfaces	1346.6	62.16
Operational items (OPS)	427.77	11.37
Payload	1100.5	41.43
Passengers	2820	Varying
Fuel	44149.41	Varying
MTOW	105682.71	

Table 6.1: Weight and center of gravity percentage of the total length [%] for all the components.

The AFT component represents the part behind the cabin. It includes the end of the inner wing and the V-tail. Besides, as the fuel is burned during the flight and the passengers can move inside the cabin, the center of gravity location of both is varying.

The range in which the center of gravity of LIFT is included is described in Section 6.3.2.

Concerning the furnishing, it represents all the stuff that are available inside the cabin. It includes seats, conference table, insulation, and all the things that are presented on the layout in Section 5.2.3. The operational items refers to the masses added to the aircraft empty weight to bring it to the operating empty condition. It consists of the masses of the crew and associated personal items, safety and freight equipment, water and food [19].

6.2 Aerodynamics

The aerodynamic analysis is carried out using a combination of empirical and numerical methods. To validate the results obtained during the conceptual design phase, numerical simulations are performed to compute quantities such as lift and induced drag. Additionally, a detailed empirical study is conducted to provide the most accurate possible estimation of total drag.

6.2.1 Lift analysis

Empirical method

To achieve the design lift coefficient of 0.45 for the entire aircraft, an angle of incidence is defined for the outer wing. The inner and outer wings lift forces are computed separately using the DATCOM empirical formula provided by Toren-

beek [9]. The same reference area is used for both, and the lift coefficients obtained for each wing part are then added together. It appears that with an angle of attack of 0° for the inner wing and 2.7° for the outer wing, the design lift coefficient is reached.

Numerical methodology and validation

The software *DARTFlo*, developed by A. Crovato at the University of Liège [55], is used for the numerical simulations. It is an open-source C++/Python unstructured finite-element full potential solver, based on the assumptions of potential, steady, isentropic, and irrotational flow, along with the hypothesis of small perturbations in the flow.

For convergence purposes, the inner wing is not modeled. Indeed, when the whole aircraft is modeled, some numerical singularities appear near the trailing edge and especially in the transition region between the inner and outer wing. In fact, this region has a highly negative sweep angle for the trainling.

Then, to be consistent in the discussion, the reference wing area, depicted in orange in Figure 5.3, is modeled in *DARTFlo*, since this area is used to compute the lift of the outer wing in the empirical method.

The cruise and climb configurations are studied, corresponding to Mach 0.9 and Mach 0.39, respectively. Thess values are discussed in Section 6.2.2.

To validate the results obtained with *DARTFlo*, a convergence study is conducted on the lift and drag coefficients, with respect to the number of elements used in the simulation.

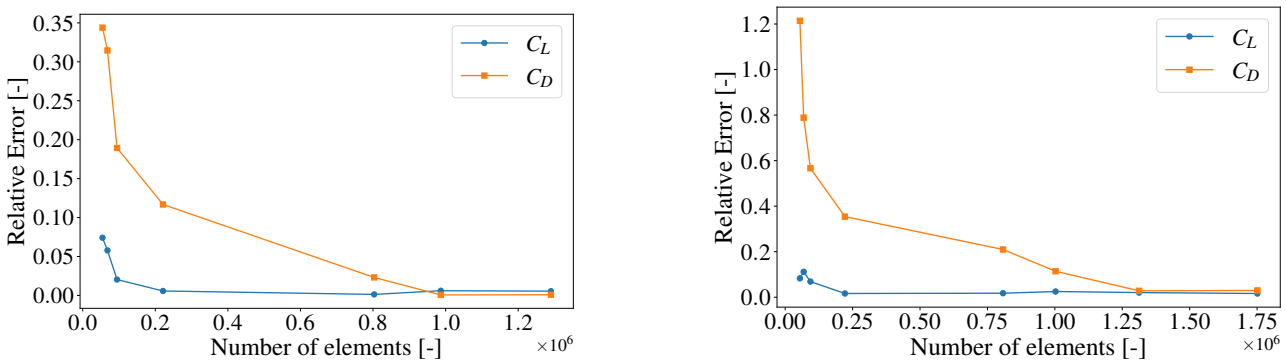

(a) Cruise convergence study with Mach 0.9.

(b) Climb convergence study with Mach 0.39.

Figure 6.2: Convergence study at 0° angle of attack on *DARTFlo* software for the reference area.

The method is considered converged when the relative error falls below 2.5%. Figure 6.2 shows that the modeling of the reference wing area reaches convergence with 986,718 elements at Mach 0.9 and with 1,312,447 elements at Mach 0.39. The same convergence study is performed for each angle of attack at both Mach number that are considered.

This convergence leads in obtaining the following mesh shown in Figure 6.3. The elements near the tip and the trailing edge are intentionally coarse to avoid singularity and convergence issue. To accurately capture sharp variations in flow quantities during shock formation, the mesh is sufficiently refined with a growth factor of 1.045.

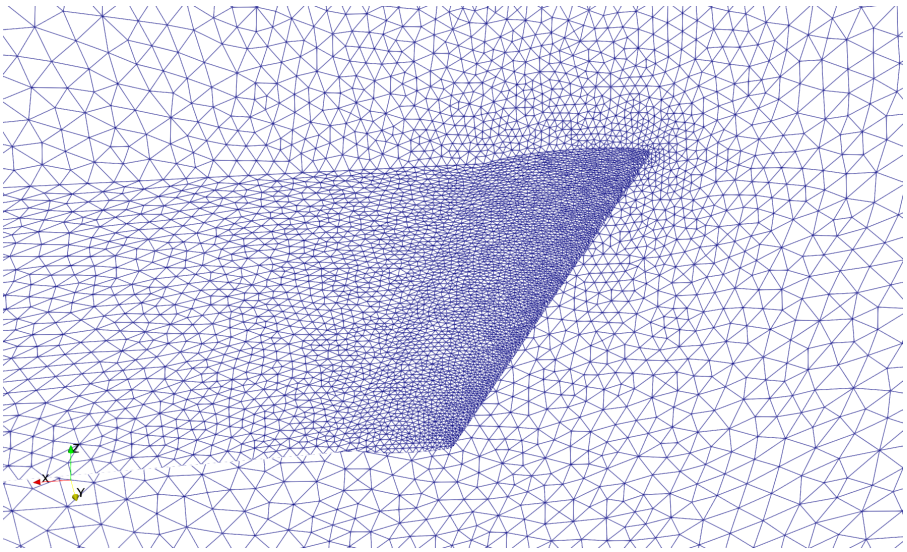

Figure 6.3: Mesh used for the simulation in cruise configuration with *DARTFlo*.

Lift variation

To compare the numerical and empirical approaches, the angle of attack required to achieve the same lift coefficient is evaluated. Since the inner wing is not modeled, this lift coefficient corresponds only to the one of the reference wing. Table 6.2 presents the angles of attack obtained with both methods.

Since the angle of attack predicted by *DARTFlo* is lower than the one derived analytically for the same C_L, this indicates that the empirical method underestimates both the generated lift and the lift curve slope in cruise configuration. In climb configuration, the angle of attack is also significantly underestimated by the empirical method, along with the corresponding lift curve slope.

	Cruise		Climb	
Parameter	Empirical	*DARTFlo*	Empirical	*DARTFlo*
Angle of attack at $C_L = 0.4$ [°]	2.7	0.8	−0.84	2.65
Lift curve slope [rad^{-1}]	3.6	7.985	3.877	4.653

Table 6.2: Comparison of the angle of attack and the lift curve slope of reference wing between empirical and numerical methods.

For the cruise configuration, the variation of lift with respect to the angle of attack for the outer wing is shown in Figure 6.4. It can be seen that, in this configuration, the numerical lift curve slope is far away to the empirical estimate, with a value of 7.985 rad^{-1}, in comparison with 3.6 rad^{-1}. However, in the climb configuration (Figure 6.4b), the angle of attack required to reach a lift coefficient of 0.4 is 2.65°, which deviates significantly from the empirical prediction and lift curve slope is 4.653 rad^{-1} which is not to far from the predictions.

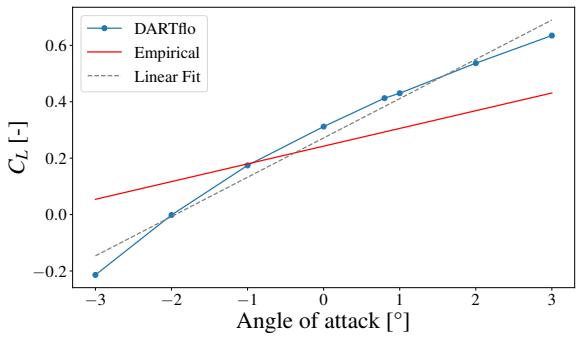

(a) Lift coefficient as a function of the angle of attack in cruise configuration (Mach 0.9).

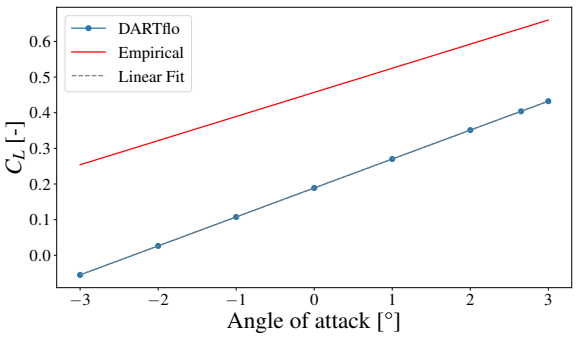

(b) Lift coefficient as a function of the angle of attack in climb configuration (Mach 0.39).

Figure 6.4: Comparison of lift coefficient evolution with angle of attack using empirical and numerical methods for both climb and cruise configurations.

The results obtained show significant discrepancies depending on the method which is used. This discrepancy can be explained in part by the limitations of the model or in the empirical data note reliable.

To define the global lift curve slope of the aircraft, Table 6.3 compares three methods. Two empirical approaches, Torenbeek and DATCOM, are commonly used. Additionally, a hybrid method combines the lift curve slope of the outer wing, computed using *DARTFlo*, and the lift curve slope of the inner wing estimated from Torenbeek's method is presented. This combined approach yields results close to those of the DATCOM method. Therefore, the hybrid method is retained, as *DARTFlo* provides an accurate estimation. This lift curve slope leads to a zero lift angle of -3.9°.

	Torenbeek	*DARTFlo* + Torenbeek	DATCOM
Lift curve slope [rad^{-1}]	4.285	6.596	6.15

Table 6.3: Comparison of the lift curve slope of total aircraft between empirical methods and combination of numerical and empirical method.

Lift distribution

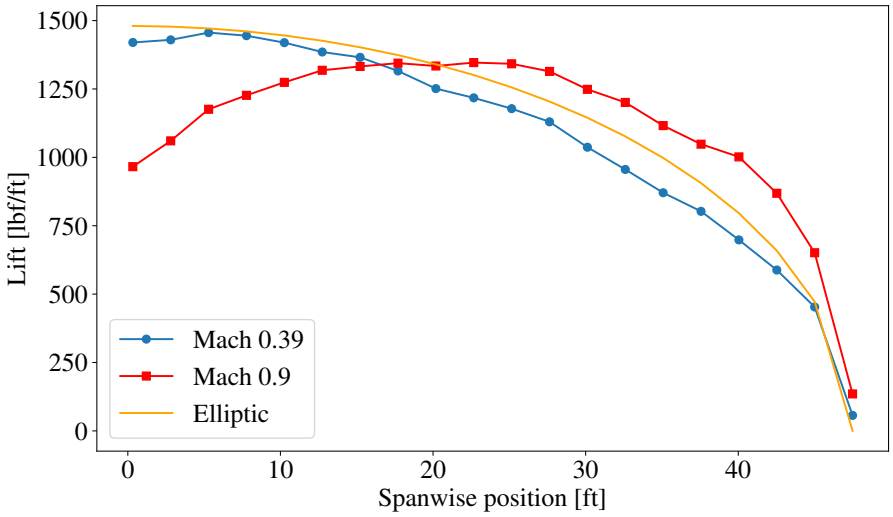

Figure 6.5: Spanwise lift distribution for a lift coefficient of 0.4.

Figure 6.5 shows lift distribution along the span. In the climb configuration, the lift distribution follow well the ideal elliptical lift distribution. At Mach 0.9, the lift distribution is no longer close to the elliptic one.

6.2.2 Drag analysis

Mach numbers calculations

Before describing the methodology used for the drag calculation, the Mach numbers for the different flight configurations can be computed. The method which is employed comes from Gudmundsson's book [32] and is based on true airspeed and atmospheric conditions. Table 6.4 summarizes the results for each flight configuration. The cruise Mach numbers is a choice discussed in Section 4.3.

Flight configuration	Mach number
Takeoff	0.204
Climb	0.392
Cruise	0.9
Landing	0.181

Table 6.4: Different Mach numbers during the cruise, climb, landing and takeoff configurations.

Methodology

To evaluate the drag acting on LIFT at cruise, the method proposed by E. Torenbeek [9] is used. It is based on empirical correlations, initially developed for conventional subsonic aircraft. Therefore, the obtained results will have to be carefully interpreted, since they will not described as accurately as possible the true drag that the aircraft will be subjected to in reality.

Besides, LIFT operates in a transonic regime, the wave drag has to be taken into account. This is done by the consideration of a form factor, which accounts for compressibility effects and sweep angles. Additional sources are also considered, as the proposed methods are combined to best match the design characteristics of LIFT.

The different assumptions made to approach a realistic implementation are also be mentioned. Throughout the method, the contribution of the tail is divided into two components: one corresponding to the equivalent horizontal surface and the other to the equivalent vertical surface, as proposed in the reference method.

The total drag is decomposed into several contributions: the protuberance, profile, induced and interference drags. Those contributions are graphically defined in Figure 6.6. The drag is analyzed during cruise, takeoff, landing and climb configurations.

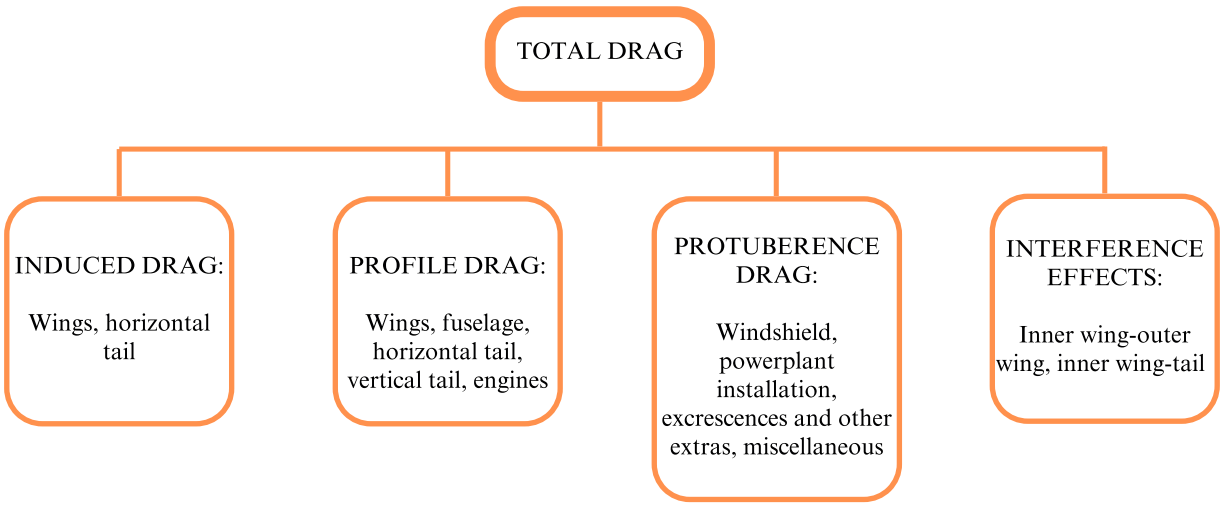

Figure 6.6: Drag contributions breakdown of LIFT.

Interference drag

This drag stands for the corrections to be applied due to the interactions between the flow fields of the isolated parts of the aircraft. It constitutes a minimal portion of the total drag and can even be negative in some cases. The considered interference interactions include outer wing-inner wing, outer wing-tailplane, and viscous interference.

Protuberance drag

Firstly, in accordance with the method proposed by E. Torenbeek [9], the drag contribution of cabin windows and the cockpit windshield is explicitly taken into account in the present study. This contribution is estimated based on the projected area of the window panels, following the statistical approach suggested by E. Torenbeek [9]. These elements are assumed to be well faired into the fuselage in order to minimize their aerodynamic impact. Then, the cooling drag caused by the ventilation of the space between the hot engine sections and the surrounding structure is also considered.

The method proposes empirical values for the profile drag penalties of jet transport due to excrescences, surface imperfections, and other additions for the outer wing, tailplane, inner wing, engine installation, and systems.

Induced drag

The induced drag is the drag due to the kinetic energy loss required to generate the trailing vortices and downwash for the outer wing and the horizontal surface of the V-tail. The downwash term is computed is Section 5.3.3. As a first approximation, the induced drag generated by the inner wing can be neglected, due to the presence of the outer wing at the tip of it.

The method considers that all main aircraft parts are isolated bodies. Initially, the outer wing is considered untwisted, and the drag factor (δ) is determined using the spanwise center of pressure (η_{cp}) for straight-tapered wings.

Moreover, an increment in induced drag is then added to account for the twist of the outer wing. The vortex-induced drag of the isolated horizontal tailplane is calculated in a similar manner to that of the outer wing.

Profile drag

The profile drag is divided into two components: skin friction drag and pressure drag. Since all the major components contributing to lift can be compared to smooth and streamlined bodies, the flat plate analogy is used.

A form factor proposed by Gudmundsson [32] accounts for the maximum thickness-to-chord ratio, compressibility effects, and sweep effects. This form factor is incorporated into the method to account for the geometric variations between LIFT main parts and the flat plate analogy. It is expressed as follows:

$$FF = 1 + \frac{(2 - M^2)\cos\Lambda_{c/4}}{\sqrt{1 - M^2\cos^2\Lambda_{c/4}}}\left(\frac{t}{c}\right) + 100\left(\frac{t}{c}\right)^4. \tag{6.1}$$

Additionally, a form factor, proposed by Gudmundosson [32], is applied for the nacelle of the engines.

Since LIFT is a transonic aircraft, it is assumed that turbulent flow remains fully developed over a flat plate surface and is affected by compressibility effects. The skin friction model proposed by Gudmundsson [32], which accounts for compressibility effects, is chosen to best fit the situation. This coefficient is defined as:

$$C_{f_{turb}} = \frac{0.455}{(\log_{10}(\mathrm{Re}))^{2.58}(1 + 0.144M^2)^{0.65}}. \tag{6.2}$$

No method is applied to account for the angle of attack of the outer wing and the horizontal tail, as the various components of LIFT are treated as streamlined bodies. The profile drag of the engine pylons is estimated using the same approach as that used for the outer wing.

Total drag

The method generally distinguishes between two types of drag coefficient formulations: drag areas ($f = (C_D \cdot S)_j$), and, more rarely, direct drag coefficients (C_{D_j}), which must then be multiplied by their respective reference areas to obtain the drag areas. To avoid confusion between the two contributions, the contribution of each streamlined bodies are related to the gross wing S area , corresponding to S_{ref} in the case of LIFT, as follows:

$$C_{D_j} = \frac{(C_D S)_j}{S}. \tag{6.3}$$

The calculated drag coefficients are shown in Figure 6.7. On one hand, they are summed to give the total drag coefficient for the considered phase of the flight envelope of LIFT. On the other hand, the total drag coefficient of LIFT can be formulated in such a way that it takes the form of a second-degree equation in terms of lift coefficient, in order to obtain

a drag polar for the different phases of the flight envelope. This decomposition is as follows:

$$C_{D_{LIFT}} = \frac{\Sigma(C_D S)_j}{S} = A + B \cdot C_L + D \cdot C_L^2, \tag{6.4}$$

where A is the zero-lift drag coefficient, B is the coefficient of C_L, D is the coefficient of C_L^2 and C_L is the total lift coefficient of LIFT. These values are calculated using Equation 6.3, where the formulas are rearranged to explicitly show the dependencies on C_L.

Cruise

The assumptions outlined above are made to enable the most realistic possible modeling of the drag experienced by LIFT during cruise.

This phase differs from the other phases of the flight envelope, as the landing gear is fully retracted into the inner wing and LIFT has reached its cruise speed and altitude. The values of the different drag coefficients, as well as the contribution of each component to the vortex-induced drag and profile drag, are listed in Tables 6.5, 6.6 and 6.7.

The first Table defined the vortex induced drag coefficient due to the outer wing and the horizontal tail. C_{D_i} refers to the vortex-induced drag coefficient, C_{D_p} to the profile drag coefficient. For simplicity, the drag due to the pylon is included with the engine. $C_{D_{pr}}$ represents the protuberance drag coefficient, and $C_{D_{int}}$ refers to the interference drag coefficient.

	Outer wing	Horizontal tail	Total
C_{D_i} [-]	0.00559	0.00102	0.00661

Table 6.5: Vortex induced drag coefficients of the different LIFT parts in cruise configuration.

	Outer wing	Inner wing	Horizontal tail	Vertical tail	Engines	Total
C_{D_p} [-]	0.00274	0.01020	0.00262	0.00100	0.00204	0.01861

Table 6.6: Profile drag coefficients of the different LIFT parts in cruise configuration.

C_L[-]	C_{D_i} [-]	C_{D_p} [-]	$C_{D_{pr}}$ [-]	C_{int} [-]	C_{D0} [-]	Total C_D [-]
0.45	0.00661	0.01861	0.00266	-0.00134	0.023563	0.026545

Table 6.7: Contributions of each type of drag to the total drag coefficient of LIFT in cruise.

Takeoff and landing

During takeoff and landing, flap deflections significantly affect the drag coefficient. At takeoff, the flaps are deflected by an angle of $\delta_f = 20°$, while during landing, the deflection reaches $\delta_f = 40°$. In this section, the most relevant corrections are discussed based on Appendix G of E. Torenbeek [9], which provides a method for evaluating low-speed drag. The drag coefficient can be expressed as follows, including the corresponding increments:

$$C_D = C_{D_0} + \frac{C_L^2}{\pi ARe} + \Delta_f C_{D_p} + \Delta_f C_{D_V} + \Delta_{trim} C_D, \tag{6.5}$$

where $\Delta_f C_{D_p}$, $\Delta_f C_{D_V}$, and $\Delta_{\text{trim}} C_D$ are the increments in profile, vortex-induced, and trim drag coefficients, respectively. C_{D_0} is also modified to account for takeoff and landing conditions. Furthermore, during these phases, the landing gear is deployed, resulting in an additional drag increase. As the aircraft flies close to the ground, the ground effect must also be considered. Lift and drag coefficients are summarized in Table 6.8 for the two configurations.

	C_L [-]	C_D [-]
Takeoff	1.337	0.181
Landing	1.692	0.233

Table 6.8: Drag and lift coefficients for takeoff and landing configurations.

Climb

The main distinction from takeoff lies in the retracted landing gear and the assumption that the aircraft is sufficiently high for ground effect to be negligible. As a result, these two drag contributions are not considered, leading to a lower overall drag coefficient. The corresponding lift and drag coefficients are summarized in Table 6.9. The contributions of the various drag components are illustrated in Figure 6.7 for the cruise, takeoff, and landing configurations.

	C_L [-]	C_D [-]
Climb	0.528	0.058

Table 6.9: Drag and lift coefficients for climb configuration.

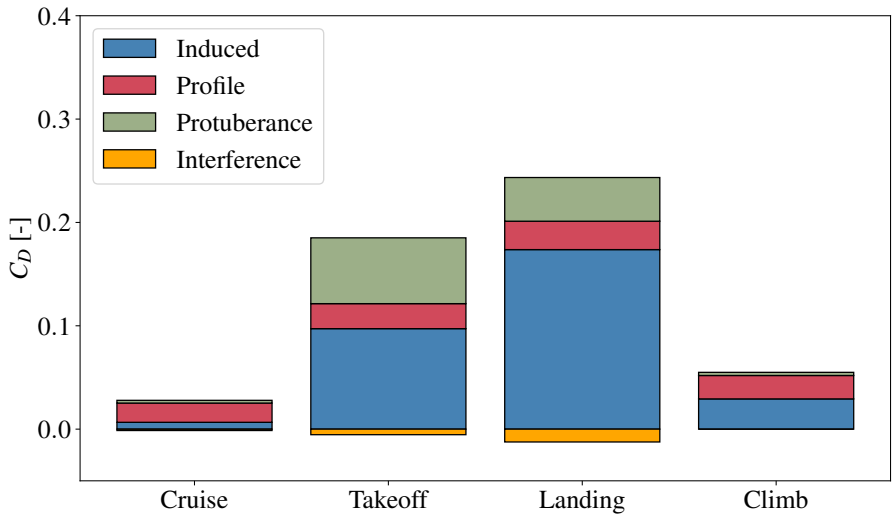

Figure 6.7: Comparison of the different contributions of drag for cruise, takeoff, landing and climb configurations.

The first notable observation is the significant increase in induced drag for takeoff, landing, and climb configurations. This is explained by the considerable increase in the lift coefficient resulting from flap deflection. Furthermore, for takeoff and landing, the interference drag is not negligible compared to that observed in cruise or climb conditions. Interestingly, this contribution is negative, representing a reduction in the overall drag coefficient.

Lift to drag ratio

In this section, the focus is on the lift to drag ratio, which can be derived from the previous analysis. The different lift to drag ratios are presented in Table 6.10. Despite the higher lift coefficients observed during takeoff and landing, the lower lift to drag ratios in these configurations are primarily due to the significantly increased drag coefficients, resulting from factors such as flap deflection, landing gear deployment, and other low-speed effects described previously.

In contrast, the climb configuration still has a significant drag coefficient, but it is much smaller than those observed during takeoff and landing. Therefore, the lift-to-drag ratio in climb is more favorable compared to takeoff and landing, as the induced drag remains moderate, even though the lift coefficient is not as high.

Additionally, the high value observed for the cruise condition is attributed to the relatively low drag coefficient associated with this phase of flight.

	Cruise	Takeoff	Landing	Climb
L/D [-]	16.95	7.37	7.27	9.1

Table 6.10: Lift to drag ratio for cruise, takeoff, landing and climb configurations.

Engine failure

Engine failure corresponds to a situation in which one engine suddenly ceases to operate, typically due to a mechanical malfunction. The resulting drag increment in cruise configuration consists of two main components: engine windmilling drag and drag due to the asymmetric flight condition.

Engine windmilling drag refers to the aerodynamic drag generated by the inoperative engine, which is no longer producing thrust and instead rotates freely under the influence of the incoming airflow.

Drag due to the asymmetric flight condition arises from the yawing and rolling moments induced by the loss of thrust on one side of the aircraft. These moments must be counteracted, primarily through ruddervator and aileron deflections, which in turn lead to an increase in overall drag.

The total drag increment is $\Delta C_{D_{\text{failure}}} = 0.009$, which corresponds to an increase of 33.9% relative to the drag coefficient in cruise. The most significant contribution to this increase arises from the engine windmilling drag. The resulting drag coefficient in cruise with one engine inoperative is $C_D = 0.0355$.

6.2.3 Comparison of the drag with another method

As the method does not initially take into account all the characteristics of LIFT, it is interesting to compare the results with others obtained from another method.

The additional method which is used is proposed by Gudmundsson [32]. The differences between both methods are analyzed for all the flight configurations in Table 6.11

Table 6.11 shows that both methods provide very similar results for the cruise configuration. Nevertheless, large relative difference appear between both methods for takeoff, climb and landing configurations. Additionally, it can be seen that, for those configurations, the drag coefficient predicted by Torenbeek's method is higher than the one obtained by using Gudmundsson's method. This can be explained by the fact that Torenbeek takes into account more physical effects than the other method. It allows to obtain more accurate results. Therefore, results from Torenbeek's method are kept.

Configuration	Torenbeek's method C_D [-]	Gudmundsson's method C_D [-]	Relative difference [%]
Takeoff	0.181	0.13225	26.93
Climb	0.058	0.03379	41.74
Cruise	0.026545	0.02679	0.92
Landing	0.233	0.19049	18.24

Table 6.11: Comparison between obtained drag coefficients using Torenbeek and Gudmundson's methods for takeoff, climb cruise and landing configurations.

6.2.4 Drag polar

As previously explained, the total drag coefficient breakdown of LIFT configuration can be expressed as a second degree equation with LIFT coefficient as the variable as shown in Equation 6.4. From this equation, a drag polar can be plotted for various C_L values. This expression provides a more refined representation of aerodynamic performance across various cruise conditions. In this Equation, the constant term A accounts for the zero-lift drag, which is primarily associated with profile drag. The linear term B captures the interaction between lift and drag; a negative value typically suggests favorable aerodynamic coupling, which helps reduce drag within a certain range of lift coefficients. The quadratic term D primarily corresponds to the induced drag.

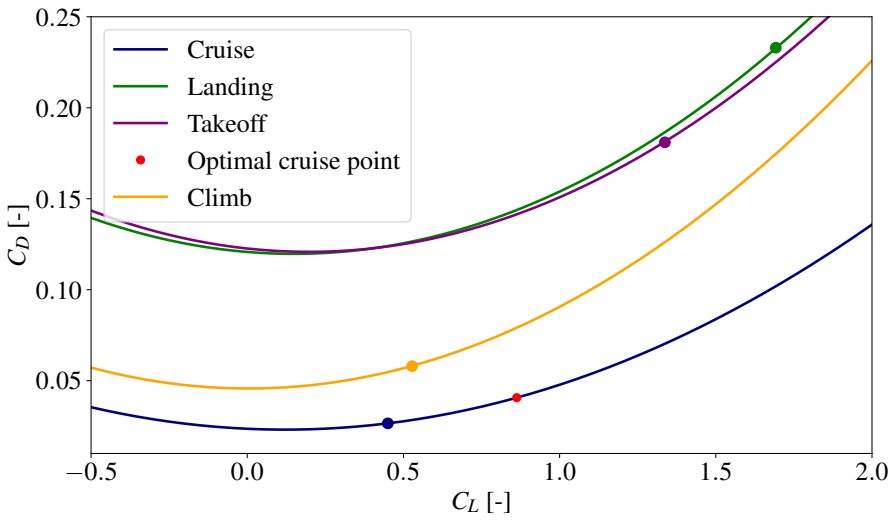

Figure 6.8: Drag polar curve for cruise, landing, takeoff and climb configurations, with the design points and the optimal cruise point (in red).

Figure 6.8 compares the cruise flight phase with the other segments of the flight envelope. As expected, the cruise configuration exhibits the lowest drag coefficients across the entire range of lift coefficients C_L, reflecting its optimized

aerodynamic performance. In contrast, the takeoff and landing phases are associated with significantly higher drag levels. This increase is primarily due to the deployment of high-lift and control surfaces, which, while enhancing lift, also contribute to a notable rise in parasitic drag. A key factor contributing to the differences observed between the curves is the altitude at which each phase occurs. At higher altitudes, the air density decreases, resulting in a linear reduction in drag. It is also noteworthy that the climb phase curve displays a steeper slope around $C_L \approx 1.5$. This behavior is largely attributed to the influence of ground effect, which becomes more pronounced as lift increases. The ground effect helps to limit the growth of drag during the low-altitude phases of flight, particularly takeoff and landing.

C_L [-]	C_D [-]
0.45	0.026545

(a) Lift and drag coefficients in cruise.

A[-]	B [-]	D [-]
0.0236	-0.0077	0.0319

(b) Values of A, B and D in the drag breakdown.

Figure 6.9: Main values of the drag analysis.

As expected, due to the shape of LIFT configuration, the outer wing generates a small induced drag. The profile drag represents the largest contribution to the overall drag in cruise configuration, which explains why the C_{D_0} of LIFT accounts for the majority of the total drag. Figure 6.8 confirms what is explained before. In cruise condition, the C_L is lower than during other configurations, while the C_D is also lower. Moreover, it can be seen that the drag is maximum during the landing, which verifies what is obtained previously.

Now, the lift to drag ratio L/D can be analyzed. However, since the method used is based on empirical approximations developed primarily for conventional aircraft, these empirical relationships do not fully align with the specific characteristics of LIFT configuration. This L/D ratio is once again calculated using the breakdown of the total drag in a cruise configuration.

Optimum L/D [-]	Cruise L/D [-]
21.24	16.95

Table 6.12: Lift to drag ratio in cruise.

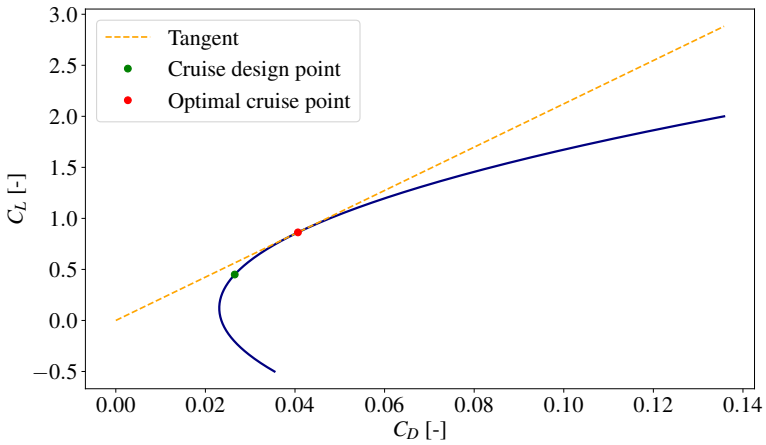

Figure 6.10: Drag polar in cruise.

As shown in Table 6.12 and Figures 6.10 and 6.11, the optimal design point under cruise conditions is not reached. Nevertheless, the resulting L/D ratio remains high for a business jet–type aircraft, indicating good aerodynamic efficiency. The results are promising, as LIFT, if optimized to achieve the optimal lift-to-drag ratio, would exhibit outstanding aerodynamic performance.

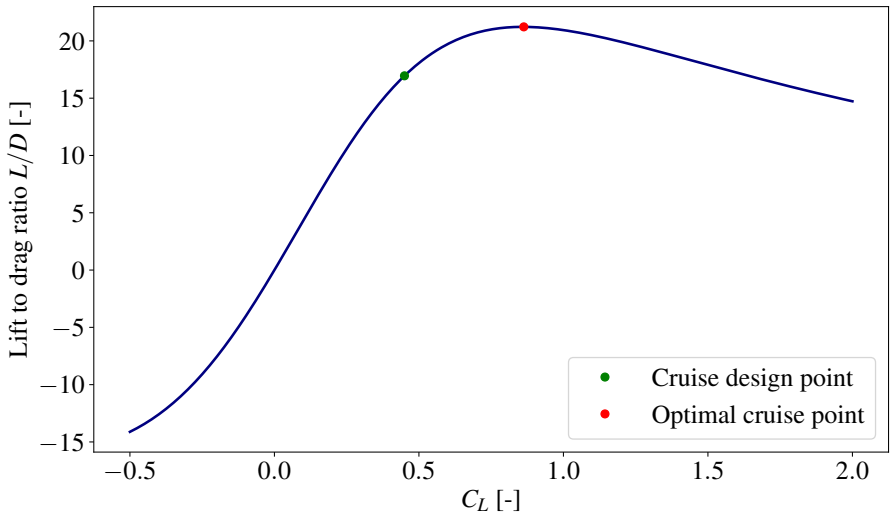

Figure 6.11: Lift to drag ratio as a function of the lift coefficient in cruise.

6.2.5 Optimal point study

In this section, a study of the optimal operating point is carried out to understand why it differs from the design point of the LIFT configuration. First, based on a mathematical analysis of Equation 6.4, the optimal lift coefficient $C_{L_{\text{opt}}}$ is defined as:

$$C_{L_{\text{opt}}} = \sqrt{\frac{A}{D}}, \tag{6.6}$$

where factor A represents the zero-lift drag coefficient C_{D0}, and factor D is the induced drag factor.

Since the objective is to understand why the design point lies below the optimum, both contributing factors are analyzed.

On one hand, factor D depends primarily on the outer wing and the horizontal tail, according to the current assumptions. Modifying this factor would require significant changes to the geometry of these components, which is not desirable at this stage.

On the other hand, as suggested in a Master's thesis from Cranfield University [56], the zero-lift drag coefficient of the Northrop XB-35, BWB aircraft flying at a speed comparable to that of LIFT, is around 0.012. This value is nearly twice as low as the one estimated for LIFT, as shown in Table 6.7. Given that LIFT flies at a slightly higher speed, a marginally higher skin friction coefficient is expected. Nevertheless, such a large discrepancy suggests that the C_{D0} obtained using Torenbeek's method might be overestimated, especially since this method is originally intended for conventional aircraft rather than BWBs.

Therefore, a parametric analysis of $C_{L_{\text{opt}}}$ and the corresponding optimal L/D ratio as a function of different A values is conducted, as shown in Figure 6.12.

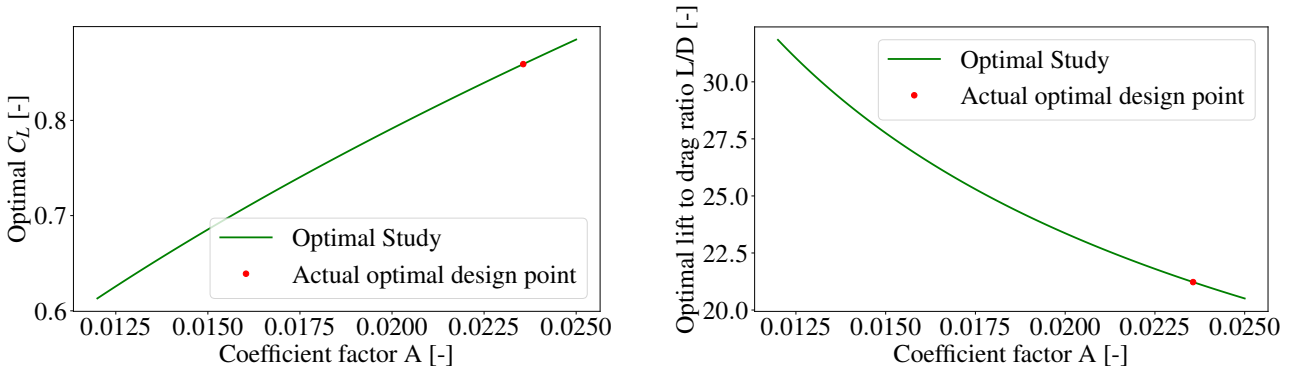

(a) Effect of reducing the zero-lift drag coefficient on the optimal lift coefficient.

(b) Effect of reducing the zero-lift drag coefficient on the optimal lift-to-drag ratio.

Figure 6.12: Influence of zero-lift drag coefficient on optimal aerodynamic parameters.

Figures 6.12a and 6.12b clearly show that adopting a more realistic value of A, consistent with typical BWB aircraft, would simultaneously increase the optimal L/D and reduce $C_{L_{\text{opt}}}$. This would bring the optimal point closer to the design point, while also improving the aerodynamic performance at both points. This analysis suggests that the discrepancy between the design and optimal points may primarily result from an overestimation of the zero-lift drag coefficient due to the limitations of Torenbeek's method when applied to BWB configurations. Another way to move closer to the optimal point is to slightly increase the lift coefficient. This could be achieved by increasing the angle of attack and by reducing the wing reference area or the cruise speed. Reducing the wing area improves drag but increases wing loading, affecting takeoff and landing. Lowering the speed also increases C_L and reduces wave drag, but extends flight time and operational costs.

6.2.6 Comparison with *DARTFlo*

In this section, the drag estimation obtained using *DARTFlo* is compared with the analytical results computed using Torenbeek's method for the outer wing for different phases of the flight envelope. This comparison aims to highlight the limitations and reliability of both approaches in the preliminary design phase of LIFT.

DARTFlo is a CFD solver capable of computing transonic flow characteristics, including shock waves and pressure drag. Depending on the fidelity level selected, *DARTFlo* can either solve inviscid flow equations or RANS equations. However, in the present study, *DARTFlo* is used in an inviscid configuration, meaning that only pressure drag is considered. This includes contributions from form drag and wave drag, but neglects viscous skin friction drag.
On the other hand, the empirical estimation based on Torenbeek's method accounts for both viscous and pressure drag through empirical correlations, making it more representative of the total drag expected in real flight conditions.

As shown in Figure 6.13, the drag predicted by *DARTFlo* is significantly higher than the empirical estimation. This is partially due to the inviscid assumption, which tends to overestimate shock wave intensity and associated wave drag, especially in transonic conditions.
While the outer wing is designed to minimize wave drag at cruise, *DARTFlo* still predicts non-negligible wave drag, as overestimating its impact.

Moreover, the induced drag computed by *DARTFlo* for the isolated outer wing does not reflect the global aerodynamic behavior of the full aircraft. In contrast, the analytical method is calibrated on complete aircraft data, including viscous and induced effects.

Given these limitations, the empirical drag estimation is retained, as it provides a more realistic baseline based on available data from similar BWB aircraft. Nevertheless, a more accurate drag prediction should be pursued in future work using higher-fidelity viscous simulations on the complete configuration.

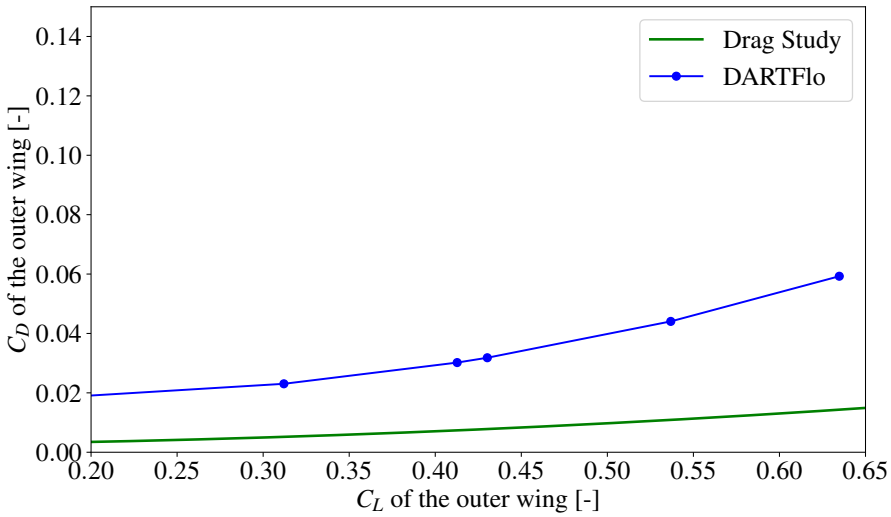

Figure 6.13: Comparison between numerical method and empirical correlations in cruise condition for the profile and induced drag coefficients of the outer wing as a function of its lift coefficient.

6.3 Stability

Static and dynamic stability are defined for the three directions in space, that will be discussed in this section.

6.3.1 Aerodynamic center and neutral point positions

As the Mach number varies during the flight, the aerodynamic center (AC) position also changes. According to empirical relations given by E. Torenbeek [9], the evolution of this position over the entire flight can be defined. Those relations being established for classical configurations, the results have to be carefully interpreted.

First both AC positions of the outer and inner wings are computed separately. Then, from them, the overall position of LIFT's AC is obtained by using a formula given by DATCOM [57]. The lifting-body force is assumed to act at this position.

The neutral point (NP), which depends on the aerodynamic center location, is computed according to Daniel P.Raymer [35].

Table 6.13 describes the variation of the AC and the NP as a function of the Mach number. Figure 6.14 describes the position of the AC on the aircraft for the different flight phases. The evaluation of the different Mach numbers is done in Section 6.2.2.

Flight phase	Mach number [-]	AC position [ft]	Neutral point [ft]
Landing	0.181	27.31	30.54
Takeoff	0.204	27.49	30.71
Climb	0.392	27.73	30.91
Cruise	0.9	28.11	31.21

Table 6.13: Aerodynamic center and neutral point positions from the nose of the aircraft and Mach numbers for the different flight configurations.

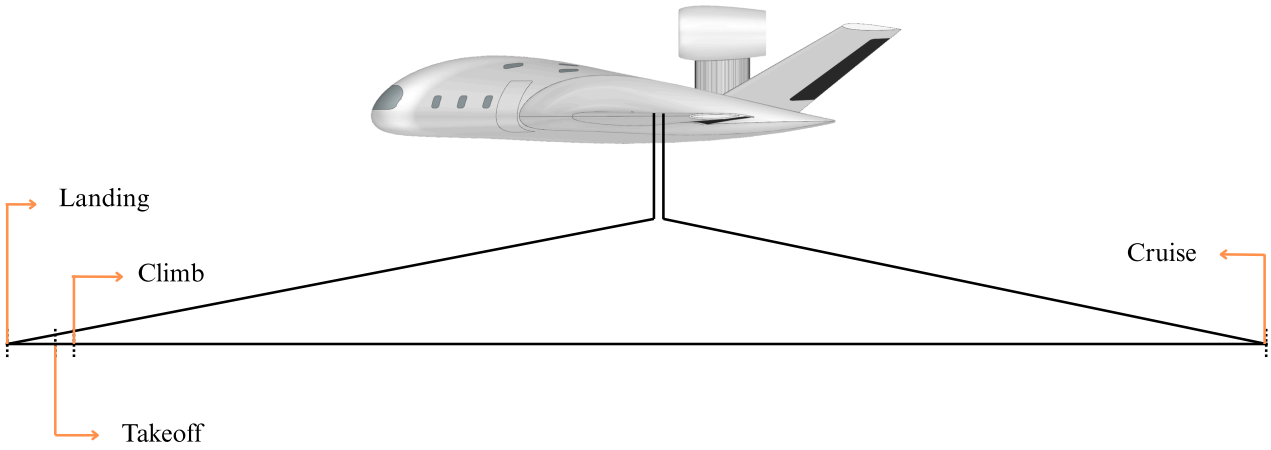

Figure 6.14: Evolution of the aerodynamic center position on the LIFT length for the different flight configurations.

As expected, the aerodynamic center moves rearward as the Mach number increases. Nevertheless, this variation is not significant, because there is a difference of 0.8 ft in position between the cruise and landing configurations.

6.3.2 Static stability

Longitudinal stability

The longitudinal static stability is governed by the static margin K_n, which must be higher than 5 % to ensure stability in the pitch plane. It is defined as [35]:

$$K_n = -\frac{dC_m}{dC_L} = \frac{x_n - x_{CG}}{\bar{\bar{c}}} = h_n - h_{CG} > 5\%, \tag{6.7}$$

where the h distances are normalized by the mean aerodynamic chord $\bar{\bar{c}}$. The subscript n stands for the neutral point, where CG is for the center of gravity.

The locations of the aerodynamic center, neutral point and of the center of gravity are represented in Figure 6.15, for the cruise flight configurations.

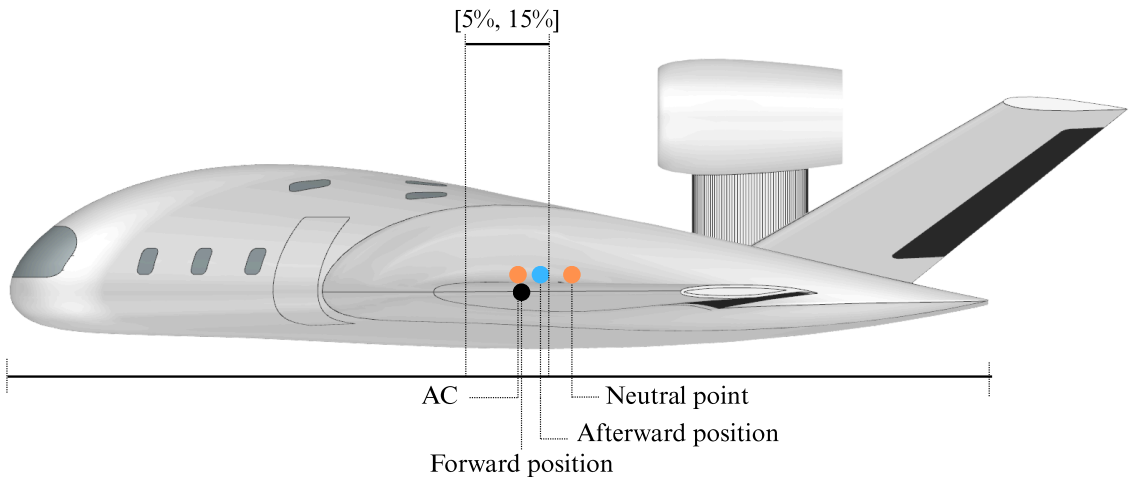

Figure 6.15: Stability range, with positions of AC, center of gravity and NP on LIFT for cruise conditions.

The center of gravity position is mainly described in Section 6.1. Nevertheless, as the its position changes during the flight, only limit cases will be considered for stability. Table 6.14 describes those positions.

	Location [ft]	Configuration
Forward position	28.28	Full fuel tanks, passengers at the front of the cabin
Afterward position	29.18	Empty fuel tanks, passengers at the back of the cabin

Table 6.14: Limit positions of the center of gravity during the flight.

The forward position and the afterward position are described in Figure 6.15 by the dark and blue point, respectively.

Table 6.15 summarizes values of the static margin for both locations of the center of gravity.

Center of gravity position	Static margin [%]
Afterward	5.64
Forward	8.15

Table 6.15: Static margin values for both limit positions of the center of gravity.

Since K_n is higher than 5 % for both limit positions of the center of gravity, the longitudinal stability is verified at cruise.

Concerning the takeoff, the longitudinal stability can be computed by using the takeoff thrust, computed in table 5.9, the AC position at takeoff, obtained from Table 6.13 and the center of gravity. This center of gravity corresponds to the forward position, since the passengers are seated at the front of the cabin and the fuel tanks are full during the takeoff.

The same method can be used for the landing phase. During the landing, the passengers are also seated. As an approximation, the center of gravity will selected for a configuration where the fuel tanks are empty. Ideally, it will not occur in reality, but it stands for the worst case. The center of gravity of this situation is placed at 28.39 ft from the nose of the aircraft.

The corresponding static margins for these flight phases, which verify the condition defined by Equation 6.7, are available in Table 6.16. In conclusion, LIFT is statically stable in all the flight configurations for the longitudinal motion.

Flight phase	Static margin [%]
Takeoff	6.76
Landing	5.98

Table 6.16: Static margin values for takeoff and landing.

Directional stability

The directional stability is calculated from the computation of the yawing moment coefficient, which is given by [42]:

$$C_{n_\beta} = \frac{\partial C_n}{\partial \beta} = C_{n_\beta fus} + C_{n_\beta wing} + C_{n_\beta tail}, \tag{6.8}$$

where β is the yaw angle. This coefficient has to be higher than 0 to ensure stability. Here, the inner wing is considered as a fuselage, in order to follow this methodology. Therefore, it has to be taken into account in the validity of the results. Components of the aircraft can have stabilizing or destabilizing effect. The inner wing has a destabilizing contribution, while the outer wing and vertical part of the V-tail are stabilizing. The tail is designed in order to compensate for the inner wing participation. Table 6.17 presents the contributions of the three parts for both limit configurations.

Center of gravity position	$C_{n_\beta fus}$ [-]	$C_{n_\beta wing}$ [-]	$C_{n_\beta tail}$ [-]	C_{n_β} [-]
Forward	-0.0220	0.0051	0.1309	0.1139
Afterward	-0.0229	0.0048	0.1322	0.1141

Table 6.17: Derivative of the yawing moment coefficient C_{n_β} with respect to the yaw angle β for the directional stability in the case of both limit positions of the center of gravity.

These values of C_{n_β} are included in the acceptable range advised by E. Torenbeek [9]. Additionally, C_{n_β} for takeoff and landing are presented in Table 6.18. It confirms that LIFT is statically stable for the directional motion for all the flight configurations.

Flight phase	C_{n_β} [-]
Takeoff	0.1132
Landing	0.1131

Table 6.18: Derivative of the yawing moment coefficient C_{n_β} with respect to the yaw angle β for the directional stability for takeoff and landing.

Lateral stability

In order to compute the roll stability, the method proposed by M.Nicolai is used [42], which says that the rolling moment coefficient

$$C_{l_\beta} = \frac{\partial C_n}{\partial \beta} = C_{l_\beta wing} + C_{l_\beta tail} + C_{l_\beta wing-fuselage} \tag{6.9}$$

has to be negative. Here, β is the sideslip angle. As a first approximation, it can be said that the desired value of C_{l_β} is the opposite of C_{n_β} [42]. Table 6.19 verifies this condition and confirms that LIFT is stable for the lateral motion in both configurations.

Center of gravity position	$C_{l_{\beta wing}}$ [-]	$C_{l_{\beta tail}}$ [-]	$C_{n_{\beta wing-fuselage}}$ [-]	C_{l_β} [-]
Forward	-0.0849	-0.0435	0	-0.1284
Afterward	-0.0849	-0.0464	0	-0.1313

Table 6.19: Derivative of the rolling moment coefficient C_{l_β} with respect to the sideslip angle β for the lateral stability in the case of both limit positions of the center of gravity.

$C_{n_{\beta wing-fuselage}}$ equals 0 in both configurations since LIFT has middle-mounted outer wings [42].

For takeoff and landing phases, C_{l_β} is available in Table 6.20. In conclusion, LIFT is statically stable for the lateral motion in all the flight configurations.

Flight phase	C_{l_β}
Takeoff	-0.1284
Landing	-0.1277

Table 6.20: Derivative of the rolling moment coefficient C_{l_β} with respect to the sideslip angle β for the lateral stability for takeoff and landing.

6.3.3 Dynamic stability

The implementation of the dynamic stability is based on the DATCOM method [57], created by the US Air Force. This methods implies empirical correlation, initially for conventional and subsonic aircraft, that are used to compute longitudinal and lateral derivatives. Since LIFT is a BWB, the results obtained from this method have to be approached carefully. To assess the robustness of the results, the computed stability derivatives are varied within a ±20% range, i.e., scaled from 0.8 to 1.2 times their nominal values, in order to evaluate their influence on the eigenvalues. If the real parts of the eigenvalues for all modes remain negative throughout this variation, the dynamic stability of the aircraft can be considered robust.

Those empirical derivatives allow to construct the state space representation of aircraft equations of motion

$$\dot{\mathbf{x}} = \mathbf{A}\mathbf{x} + \mathbf{B}\mathbf{u}, \tag{6.10}$$

with $\mathbf{x} = (u, v, w, p, q, r, \theta, \varphi, \psi)^T$ the states and $\mathbf{u} = (\eta, \xi, \zeta)$ the inputs [58].

Since the longitudinal and lateral motions can be decoupled, they will be analyzed separately. Thus, the derivatives will be presented in separated tables. The dynamic stability for both motions is defined by the eigenvalues of the A matrix, which must have a positive real part. From those eigenvalues, frequencies and damping ratios of each mode can be computed [58]. The frequency of oscillations corresponds to the module of the complex eigenvalue, while the damping ratio is the absolute real part of the eigenvalue, divided by the oscillations frequency. Tables 6.21 and 6.22 show the corresponding derivatives in cruise conditions. Furthermore, as it provides more accurate results, as discussed

in Section 6.2.1, the lift curve slope which is used is computed from numerical and experimental methods. It is equal to 6.596 rad^{-1}.

Derivative	Value [-]
C_{L_α}	6.150
C_{D_α}	0.385
C_{M_α}	-0.615
C_{L_u}	0.9
C_{D_u}	0.052
C_{M_u}	-0.027
C_{L_q}	4.114
C_{D_q}	0
C_{M_q}	-2.493
$C_{L_{\dot{\alpha}}}$	0.0001
C_{D_α}	0
C_{M_α}	-0.0002

Table 6.21: Longitudinal derivatives for dynamic stability.

Derivative	Value [-]
C_{y_β}	-0.3891
C_{n_β}	-0.0129
C_{L_β}	-0.1171
C_{y_r}	0.00001
C_{n_r}	-0.0688
C_{L_r}	0.2679
C_{y_p}	0
C_{n_p}	-0.0493
C_{L_p}	-0.5485

Table 6.22: Lateral derivatives for dynamic stability.

Longitudinal modes	Lateral modes
-1.168+4.488j	0
-1.168-4.488j	-2.124
-0.002+0.046j	-0.022+0.474j
-0.002-0.046j	-0.022-0.474j
	-0.065

Table 6.23: Eigenvalues of the longitudinal and lateral modes for dynamic stability.

Longitudinal modes

The longitudinal modes are characterized by two complex conjugate pairs. One describes the phugoid mode, while the other stands for the short period oscillations mode. Frequencies and damping ratios of those modes are listed in Table 6.24.

There exists not any requirement concerning damping ratios and frequencies for the civil aviation. Nevertheless, they can be compared to levels of flying qualities proposed by MIL-F-8785C, that defines flying qualities of piloted airplanes for military application [59].

Mode	Frequency [rad/s]	Damping ratio ζ [-]
Phugoid	0.0458	0.0391
Short period oscillations	4.6376	0.2518

Table 6.24: Frequency and damping ratio for phugoid ans short period oscillations modes.

Since $0.2 < \zeta < 0.3$ for the short period oscillations mode and the damping ratio of the phugoid is lower than 0.04, both modes are level 2 of qualities, which leads to a degradation in mission effectiveness with an increase of pilot workload.

Lateral modes

One complex conjugate pair and two real eigenvalues stand for the lateral modes. The dutch roll is characterized by a the complex pair, which has positive real part. Thus, this mode is stable. Besides, the two real eigenvalues are for roll subsidence and spiral modes, that are both non oscillating modes. Therefore, they are defined by a time constant, calculated from the opposite of the inverse of the eigenvalue module. Modes characteristics are summarized in Table 6.25.

Mode	Frequency [rad/s]	Damping ratio [-]	Time constant T [s]
Dutch roll	0.458	0.04747	-
Spiral	-	-	0.4708
Roll subsidence	-	-	15.2835

Table 6.25: Frequency and damping ratio for the dutch roll mode and time constants for spiral and roll subsidence modes.

As for the longitudinal modes, lateral modes will be compared to MIL-F-8785C requirements, even if there is no regulation for the civil aviation. The roll subsidence mode is level 2, since $8 < T < 20$, while the spiral mode is level 1 because $T < 1.4$s. Concerning the dutch roll mode, it is level 3 of flight qualities, which means inadequate mission effectiveness with high pilot workload.

Sensitivity analysis

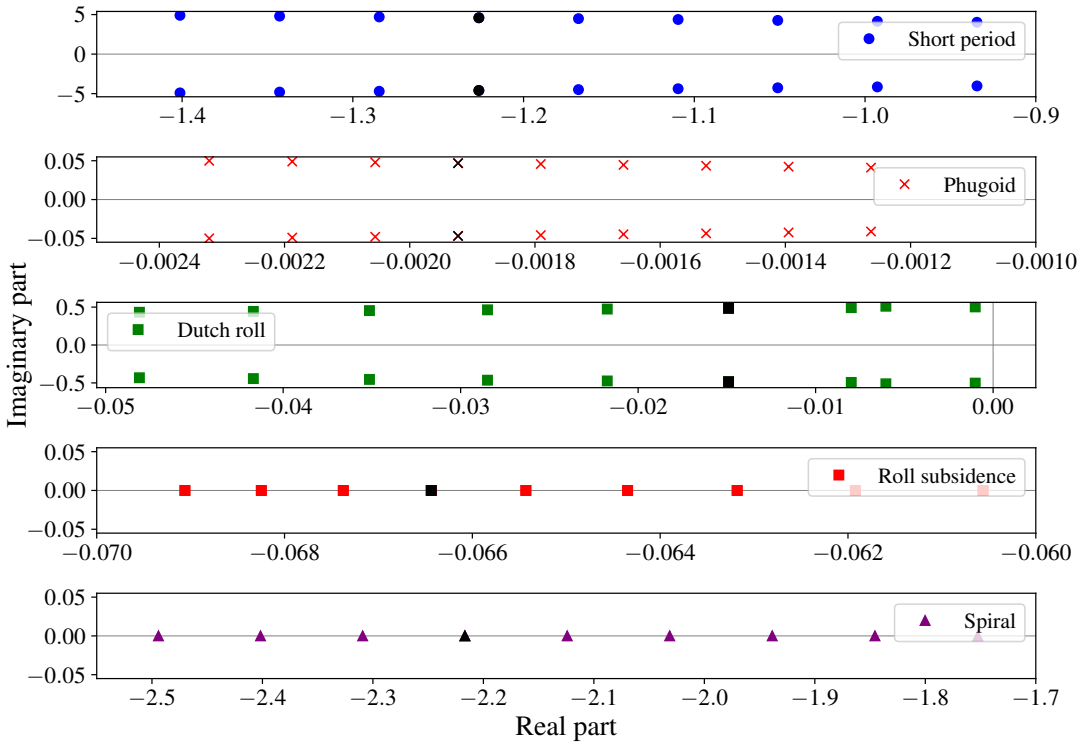

Figure 6.16: Sensitivity study on the eigenvalues of the eigenvalues for both lateral and longitudinal motions with the design configuration in black.

As the DATCOM method is initially not adapted for LIFT's type of aircraft, the coefficients that are computed in order to obtain the eigenvalues of the different modes are possibly not exact. Therefore, they are varied from a factor of 0.8 to 1.2

to see the change in the eigenvalues. Since the real parts remain negative, these variations do not alter the stable nature of LIFT's dynamic modes. Figure 6.16 presents the different eigenvalues in the complex plane, where each conjugate pair of eigenvalues corresponds to different coefficients values. The design eigenvalues are represented in black.

In conclusion, the DATCOM method proves to be a suitable tool for a preliminary evaluation of LIFT's dynamic stability, as the aircraft remains stable even when the coefficients are varied within a reasonable range.

6.4 Equilibrium in cruise

Since the aerodynamic center and the center of gravity are defined, the equilibrium in the pitch plane for cruise conditions can be verified.

All the forces acting on the aircraft are represented in Figure 6.17.

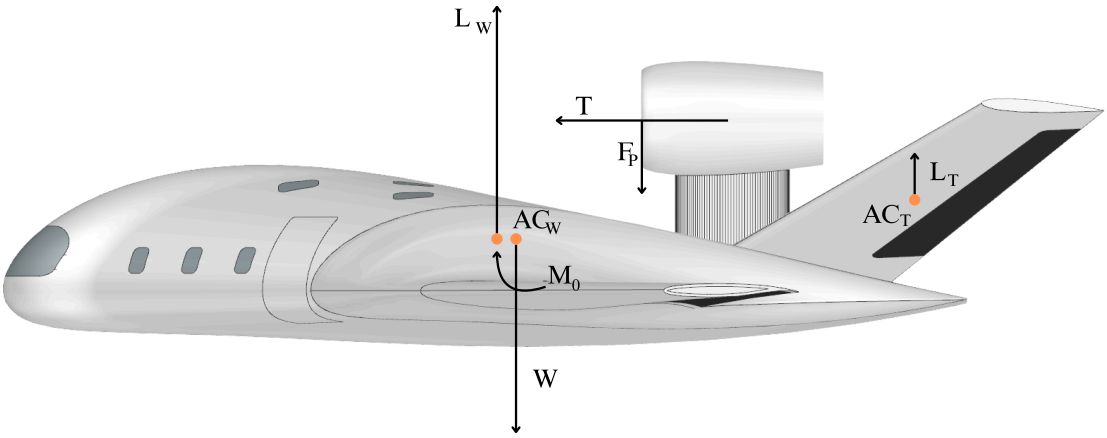

Figure 6.17: Forces that act on LIFT in order to form the pitching equilibrium equations.

The two lifting surfaces, the tail and the body, are designed in order to satisfy the static pitching equations, which are as follow:

$$L + L_T - W + F_P = 0 \tag{6.11}$$

which is the translational equation with L and W the total lift force and the weight, respectitvely, and

$$M_0 + L\left(x_{CG} - x_{AC}\right) - L_T\left(x_{AC_T} - x_{CG}\right) - T\left(z_{engines} - z_{CG}\right) + F_P\left(x_{CG} - x_{engines}\right) = 0 \tag{6.12}$$

which represents the rotational equation around the center of gravity of LIFT.

The force F_P is the force resulting from the turning of the air at the inlet front face of the engines, which is computed from an equation given by Raymer [35]. Additionally, $z_{engines}$ and $x_{engines}$ stand for the height of the engines and the position of them from the nose of the aircraft, respectively.

The positions of the aerodynamic center and center of gravity x_{AC} and x_{CG}, respectively, are discussed in Sections 6.1 and 6.3.1.

The total intrinsic moment due to the lifting surface is computed from airfoil moment coefficients [9], which does

not take into account the tail since its airfoil is symmetric.

Additionally, the drag of the engines is accounted for in the thrust term T, and the drag of the tail can be considered negligible compared to T.

In conclusion, Equations 6.11 and 6.12 verify that LIFT is at equilibrium during cruise configuration.

6.5 Structure

6.5.1 Placard diagram

The Placard diagram illustrates the altitude-velocity dependency. The ceiling, defined by the lift and thrust limits, is 52,492 ft. The two velocities depicted in Figure 6.18, V_C and V_D, correspond to the design cruise velocity and the dive velocity, respectively. V_C is determined by equating the drag force to the available thrust at maximum engine power. It is given by:

$$V_C = \sqrt{\frac{2T_{\max}}{\rho S C_D}}, \tag{6.13}$$

where $T_{\max}$ and ρ depend on the altitude, while C_D depends on both altitude and V_C itself, making the expression implicit.

The design cruise Mach number, M_C, corresponds to the Mach number associated with V_C, and is therefore obtained under maximum engine thrust conditions. Above the design altitude, the maximum velocity is limited by a constant M_C, as compressibility effects prevent flight at higher Mach numbers. Below the design altitude, the air density increases. However, since the temperature remains constant up to the stratospheric limit, the Mach number remains equal to M_C. Beneath the stratospheric limit, the combined effects of increased drag due to higher air density and the limited thrust available from the engine result in a decrease in true airspeed.

During a dive, the jet can exceed the design cruise Mach number. The design dive Mach number is defined as $M_D = 1.25\, M_C$. As with M_C, above the design altitude, M_D is constant. Below the design altitude, V_D is defined as the minimum between the velocity corresponding to M_D and $1.25\, V_C$.

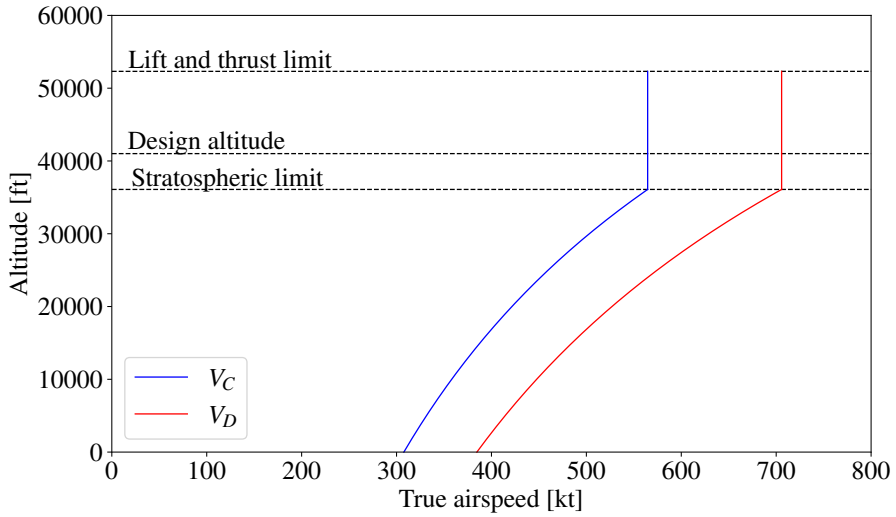

Figure 6.18: Placard diagram.

6.5.2 Maneuver envelope

The maneuver and gust envelopes illustrate the various loads experienced by the aircraft under several critical flight conditions, each corresponding to a specific airspeed. Equivalent airspeed is used to minimize the impact of altitude dependency.

The maneuver envelope is shown in blue in Figure 6.19. For a heavy aircraft, and in accordance with FAR requirements, the maneuvering load factor is limited to a minimum of -1 and a maximum of 2.5. The calculation of the load factor is given by the following equation:

$$n = \frac{L}{W} = \frac{\rho_0 V_e^2 S C_{L,\max}}{2W}, \tag{6.14}$$

where ρ_0 is the air density at sea level, and V_e is the equivalent airspeed.

From this curve, V_{s1} and V_A can be determined. V_{s1} represents the stall velocity in cruise conditions and is defined as the intersection of the stall line with the load factor equal to one. V_A represents the maximum velocity at which full control deflection is permitted and corresponds to the intersection of the stall line with $n_{\max}$.

Furthermore, the limit load factor is defined as the maximum load that the airplane can withstand during flight. The ultimate load factor is then obtained by multiplying the maximum load factor by a safety factor of 1.5. This leads to $n_{\text{ultimate}} = 3.75$. The structure must be able to sustain the ultimate load for at least 3 seconds without failure. It is important to note that for load factors exceeding the limit load factor, the aircraft would experience permanent deformations.

Concerning the gust envelope, shown in red in Figure 6.19, it accounts for sudden gusts that the jet may encounter during flight. This envelope is derived from the maneuver envelope. The gust velocities, denoted as U_e, are determined by interpolating their values at different altitudes and are expressed in ft/s. The gust load factor is given by the following equation:

$$n_g = 1 + \frac{F C_{L,\alpha\ \text{plane}} U_e V_e S}{498W}, \tag{6.15}$$

where V_e is the equivalent airspeed in kt, and F is the gust alleviation factor. F can be determined as follows:

$$F = \frac{0.88\mu}{5.3+\mu} \quad \text{with} \quad \mu = \frac{2W}{\rho C_{L,\alpha plane} cgS}, \tag{6.16}$$

where μ is the airplane weight ratio.

Using the gust envelope, the minimum speed required to enter a gust region without stalling, V_B, can be determined. It is defined as the intersection between the stall curve and the n_g curve.

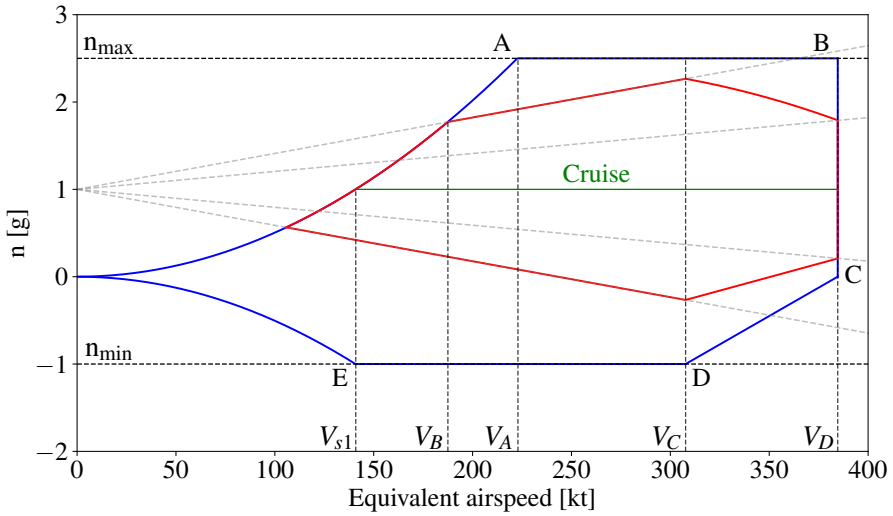

Figure 6.19: Maneuver envelope (blue), gust envelope (red) and gust loads (doted grey lines) at design altitude.

6.5.3 Aerodynamic loads

In this section, the various critical configurations, represented by points A, B, C, D, and E in Figure 6.19, are analyzed to determine the corresponding aerodynamic loads and angles of attack. All the relevant loads are depicted in Figure 6.20.

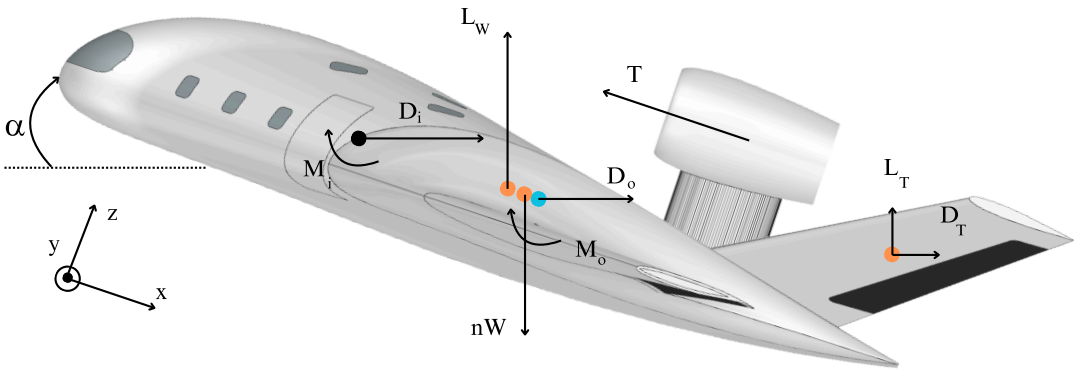

Figure 6.20: Representation of the aerodynamic loads acting on LIFT during the flight.

The equilibrium of vertical forces and the moment equilibrium about the center of gravity yield the following equations:

$$\begin{cases} L_W + L_T = nW - T\sin(\alpha); \\ l_W \cdot L_W - l_T \cdot L_T = I_\theta \cdot \ddot{\theta} - M_i - M_O - l_i \cdot D_i + l_T \cdot D_T + l_o \cdot D_o + l_{thrust} \cdot T, \end{cases} \tag{6.17}$$

with

- L_W and L_T the lift of the reference wing and the tail, respectively.
- nW the product of the load factor and the MTOW.
- T the thrust provided by the engine.
- α the angle of attack.
- l_i the lever arm with respect to the center of gravity.
- I_θ = 9,455,821.28 [lb·ft^2] the moment of inertia computed with SIEMENS NX 22 software [60].
- $\ddot{\theta} = \frac{39n(n-1.5)}{V}$ [rad/s^2] the maximum pitch acceleration, following the FAA Part 25 regulation.
- M_i and M_o the pitching moment of the inner wing and the outer wing respectively.
- D_i, D_T, D_o the inner wing, tail and outer wing drag respectively.

The third equation needed to complete the system of three unknowns is the equation of the lift of the reference wing:

$$L_W = \frac{1}{2}\rho V^2 S C_{L_\alpha}(\alpha - \alpha_{L0}). \tag{6.18}$$

The fin loading may also be calculated such as:

$$F_{fin} = \frac{1}{2}\rho V^2 S_{HT} a_T \psi \tag{6.19}$$

with a_T the vertical tail lift curve slope and $\psi = 15$ [°], the maximum yaw angle.

Finally, the aerodynamic loads for each critical point are listed in Table 6.26.

6.5.4 Structural loads

Due to the non-conventional configuration of the LIFT, the analysis is restricted to the more traditional wing section, as illustrated in Figure 6.21.

Regarding the inner wing structure, its non-cylindrical configuration introduces some challenges for pressurization. To address this, several structural concepts merit consideration [19]. Among them are Liebeck's Integrated Skin and Shell Concept [61], as well as NASA's Multi-Bubble Fuselage (MBF) [62] and the Columned Multi-Bubble Fuselage (CMBF)

	A	B	C	D	E
n [-]	2.5	2.5	0	-1	-1
V [kt]	223	385	385	308	141
α [°]	3.52	-2.68	-5.75	-7.57	-13.82
L_W [lbf]	237,698	246,373	17,784	-75,538	-78,163
L_T [lbf]	25,943	18,430	-16,707	-28,765	-24,990
D_i [lbf]	2,585	7,696	7,696	4,925	1,033
D_o [lbf]	1,194	3,556	3,556	2,276	477
D_T [lbf]	161	479	479	307	64
M_o [lbf·ft]	-223,895	-666,529	-666,529	-426,579	-89,464
M_i [lbf·ft]	113,260	337,170	337,170	215,789	45,256
F_{fin} [lbf]	24,730	73,621	73,621	47,118	9,882

Table 6.26: Aerodynamic loads at each critical point of the maneuver envelope.

proposed by Cho et al. [63]. These approaches provide promising avenues for overcoming the structural and pressurization complexities inherent in blended wing body configurations.

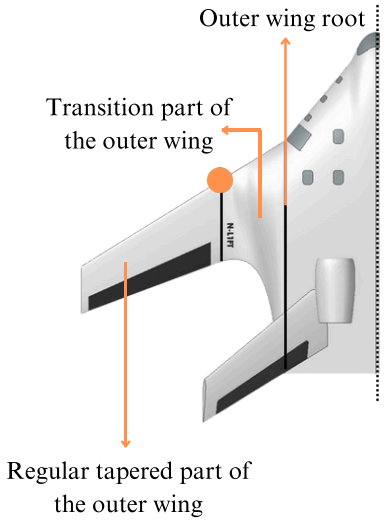

Figure 6.21: Top view of the different part of the outer wing.

The selected portion of the wing is the one between the transition part and the regular taprered part of the outer wing. It is subjected to various external loads, including lift (L_{wt}), drag (D_{wt}), its own weight (W_{wt}), and an aerodynamic pitching moment (M_w). Due to the aircraft's symmetry, only half of the wing is analyzed. Consequently, all forces are halved, and the contributions from the transition section are subtracted to isolate the loads acting solely on the region under investigation.

The equilibrium of forces and moments is established with respect to a local coordinate system, located at the leading edge of the analyzed section and represented by the orange point in Figure 6.21. It is important to note that this reference frame differs from the one used in Figure 6.20. In this reference frame, the y-axis is aligned with the chordwise direction, the x-axis with the spanwise direction, and the z-axis points upward. The analytical expressions for the internal forces and moments are provided in Equations 6.20, where α is the angle of attack and β is the setting angle at the studied section. These expressions are then evaluated at key points within the flight envelope, with the corresponding numerical

results adapted for the wing summarized in Table 6.27.

$$
\begin{cases}
T_x = 0 \\
T_y = \left(\dfrac{nW_{wt}}{2} - \dfrac{L_{wt}}{2}\right)\sin(\alpha+\beta) + \dfrac{D_{wt}}{2}\cos(\alpha+\beta) \\
T_z = \left(-\dfrac{nW_{wt}}{2} + \dfrac{L_{wt}}{2}\right)\cos(\alpha+\beta) + \dfrac{D_{wt}}{2}\sin(\alpha+\beta) \\
M_x = \dfrac{1}{2}\cos(\alpha+\beta)\left(-nW_{wt}\cdot y_{cg,w} + L_{wt}\cdot y_{ac,w} - D_{wt}\cdot z_{ac,w}\right) \\
\qquad + \dfrac{1}{2}\sin(\alpha+\beta)\left(-nW_{wt}\cdot z_{cg,w} + L_{wt}\cdot z_{ac,w} + D_{wt}\cdot y_{ac,w}\right) - \dfrac{M_w}{2} \\
M_y = \dfrac{1}{2}\cos(\alpha+\beta)\left(nW_{wt}\cdot x_{cg,w} - L_{wt}\cdot x_{ac,w}\right) + \dfrac{1}{2}\sin(\alpha+\beta)\left(D_{wt}\cdot x_{ac,w}\right) \\
M_z = \dfrac{1}{2}\sin(\alpha+\beta)\left(nW_{wt}\cdot x_{cg,w} - L_{wt}\cdot x_{ac,w}\right) + \dfrac{1}{2}\cos(\alpha+\beta)\left(D_{wt}\cdot x_{ac,w}\right)
\end{cases}
\tag{6.20}
$$

	A	B	C	D	E
T_x [lbf]	0	0	0	0	0
T_y [lbf]	-5,039.02	-490.32	730.52	-263.85	-1,956.55
T_z [lbf]	38,270.64	40,185.28	3,226.96	-11,879.50	-12,198.40
M_x [lbf·ft]	404,747.60	504,119.13	152,574.79	-35,006.57	-99,692.02
M_y [lbf·ft]	-312,403.88	-328,445.99	-27,068.41	96,277.88	99,104.72
M_z [lbf·ft]	-41,170.36	-3,931.49	6,066.11	-2,078.02	-15,920.01

Table 6.27: Structural loads acting on the studied wing section at various points of the flight envelope.

6.5.5 Structural design

The next step involves designing the wing structure to support the previously evaluated loads. This structural design phase determines the cross-sectional areas of the stringers and the thickness of the skin in the studied wing segment. The methodology employed follows the framework taught in the Aeronautical Structures course by Professor L. Noels at the University of Liège, Belgium [64].

The analysis begins with the idealization of stringers into discrete elements known as booms, a simplification used to facilitate analytical stress calculations. The following assumptions are made: direct stresses are carried exclusively by the booms, while the skin is assumed to carry only shear stresses. Additionally, the twist angle is neglected. In a subsequent section, a finite element analysis is conducted using SIEMENS NX 22 software [60] to compare with the analytical results.

Two design strategies are available. The first is the elastic design approach, which limits the stress based on the 0.1% proof stress divided by a safety factor s. The second is the ultimate load design method, which relies on the ultimate stresses and applies an ultimate load factor to the applied loads.

In this study, the elastic design approach is adopted. As outlined in Section 5.6, the selected material is a carbon fiber reinforced polymer (CFRP), specifically HexPly® M21EV/IMA. Using a safety factor of 1.5, the allowable direct and shear stresses are calculated as shown in Equation 6.21 :

$$\sigma_{max} = \frac{\sigma_{yield}}{s} = \frac{218}{1.5} = 145.3 \text{ ksi} \quad \text{and} \quad \tau_{max} = \frac{\tau_{yield}}{s} = \frac{13.6}{1.5} = 9 \text{ ksi} \tag{6.21}$$

Wing section

The tapered wing is idealized into two structural cells. The first cell extends from the leading edge to the first spar, located near the quarter-chord. The second cell spans from this spar to a second spar positioned just ahead of the control surfaces, at $y/c = 0.7$. Beyond this point, no further structural cell is considered.

A total of 37 booms are distributed across the section, with a spacing of 7.8 inches between consecutive booms. The layout of the booms within the airfoil section is illustrated in Figure 6.22.

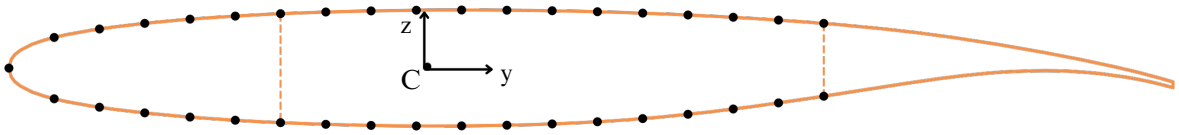

Figure 6.22: Distribution of the booms along the airfoil profile.

Boom area

The initial step is to determine the coordinates of the centroid, (y_C, z_C), using the positions (y_i, z_i) of each boom in a frame of reference at the leading edge. For simplification in manufacturing, all booms are assumed to have identical area $B = B_i$. The centroid is then computed as :

$$y_C = \frac{\sum_{i=1}^{N} B_i x_i}{\sum_{i=1}^{N} B_i} = 5.64 \text{ ft}, \qquad z_C = \frac{\sum_{i=1}^{N} B_i z_i}{\sum_{i=1}^{N} B_i} = 0.02 \text{ ft}. \tag{6.22}$$

Taking the centroid as the reference for the local coordinate system, the direct stress in each boom is computed using :

$$B\sigma_{xx}^{i} = \frac{\left(\frac{I_{zz}}{B} M_y + \frac{I_{yz}}{B} M_z\right)(z_i) - \left(\frac{I_{yz}}{B} M_y + \frac{I_{yy}}{B} M_z\right)(y_i)}{\left(\frac{I_{yy}}{B}\right)\left(\frac{I_{zz}}{B}\right) - \left(\frac{I_{yz}}{B}\right)^2}. \tag{6.23}$$

Here, I_{yy}/B, I_{zz}/B, and I_{yz}/B represent the second moments of area per unit boom area. For each load case in the flight envelope, the minimum required boom area B_{min} is determined as :

$$B_{min} = \max \left| \frac{B\sigma_{xx}^{i}}{\sigma_{max}} \right|. \tag{6.24}$$

The critical case occurs at point **B** of the envelope, leading to a minimum boom area of $B_{min} = 0.130 \text{ in}^2$.

Skin thickness

The skin, assumed to have a constant thickness, is designed to resist shear loads T_y, T_z, and the torsional moment M_x. The first step is to compute the open-section shear flow $q_0(s)$ in each skin segment between adjacent booms :

$$q_0(s) = -\frac{\left(\frac{I_{yy}}{B}T_z^{\text{web}} - \frac{I_{yz}}{B}T_y^{\text{web}}\right)}{\left(\frac{I_{yy}}{B}\right)\left(\frac{I_{zz}}{B}\right) - \left(\frac{I_{yz}}{B}\right)^2}\left[\sum_{i:s_i\leq s} z_i\right] - \frac{\left(\frac{I_{yy}}{B}T_y^{\text{web}} - \frac{I_{yz}}{B}T_z^{\text{web}}\right)}{\left(\frac{I_{yy}}{B}\right)\left(\frac{I_{zz}}{B}\right) - \left(\frac{I_{yz}}{B}\right)^2}\left[\sum_{i:s_i\leq s} y_i\right]. \tag{6.25}$$

The web-corrected loads are :

$$\begin{cases} T_y^{\text{web}} = T_y - \sum_i P_y^i \quad \text{with} \quad P_y^i = B\,\sigma_{xx}^i\,\dfrac{\delta y^i}{\delta x}, \\ T_z^{\text{web}} = T_z - \sum_i P_z^i \quad \text{with} \quad P_z^i = B\,\sigma_{xx}^i\,\dfrac{\delta z^i}{\delta x}. \end{cases}$$

A closed-section correction term q^I is then added for each cell. This term is obtained from the momentum equilibrium (Equation 6.26) and the twist rate compatibility (Equation 6.27).

$$y_T T_z - z_T T_y = \oint_{C_1} q_0 p\,ds + \oint_{C_2} q_0 p\,ds + 2A_1 q^I(0) + 2A_2 q^{II}(0) + \sum_i^N \sigma_{xx}^i\,B\,\frac{\delta z_i}{\delta x} y_i - \sum_i^N \sigma_{xx}^i\,B\,\frac{\delta y_i}{\delta x} z_i. \tag{6.26}$$

$$A_2\left(q^I(0)\,l_{\text{cell},1} + q^{II}(0)\,l_{\text{spar }1,2} + \oint_{C_1} q_0\,ds\right) = A_1\left(q^{II}(0)\,l_{\text{cell},2} + q^I(0)\,l_{\text{spar }1,2} + \oint_{C_2} q_0\,ds\right), \tag{6.27}$$

with $l_{\text{cell},1}$, $l_{\text{cell},2}$ are the perimeter of the two cells and $l_{\text{spar }1,2}$ is the lenght of the spar between cell 1 and 2. The shear flows due to torsion in each cell, q_1 and q_2, are then computed by solving :

$$\begin{cases} M_x = 2A_1 q_1 + 2A_2 q_2, \\ 0 = q_1\left(\dfrac{l_{\text{cell},1}}{A_1} + \dfrac{l_{\text{spar }1,2}}{A_2}\right) - q_2\left(\dfrac{l_{\text{cell},2}}{A_2} + \dfrac{l_{\text{spar }1,2}}{A_1}\right). \end{cases} \tag{6.28}$$

Finally, the total shear flow is obtained by summing all contributions. The required skin thickness is then determined using the maximum shear flow and allowable shear stress :

$$t_{\min} = \frac{q_{\max}}{\tau_{\max}} = 0.427 \text{ in.} \tag{6.29}$$

Although CFRP exhibits excellent tensile strength, its relatively low shear strength explains the substantial thickness required in the design.

6.5.6 Structure Finite Element Analysis

In light of the simplifications made during the analytical part of the structural design, a useful benchmark for comparing the results can be obtained through Finite Element Method (FEM) analysis. As said previously, the focus is on the root

wing of the regular tapered wing as represented in Figure 6.21. The solver used for the simulation is Simcenter Samcef from Siemens NX-22 [60].

Model

The section of the wing consists of a tapered extension of the Sc(2)-0710 airfoil, as described in Figure 5.2. It extends from the tip of the wing to the root wing, just before the curvature of the transition wing. The wing retains the characteristics listed in Table 5.2, notably having a span of 22.61 feet. Additionally, the twist is incorporated into the geometry, which is not considered in the analytical study. The global configuration of the wing structure is illustrated in Figure 6.23, with stringers in blue, spars in green, ribs in orange, and the skin in gray.

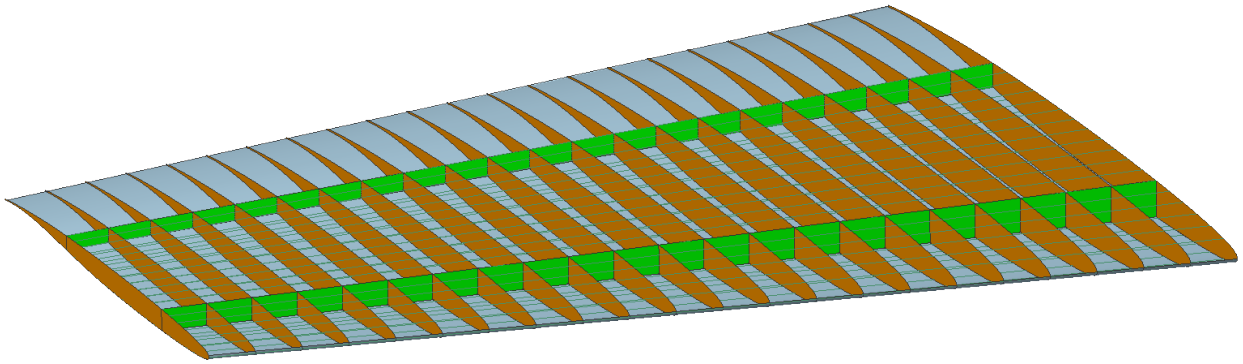

Figure 6.23: Tapered wing structural layout with stringers in blue, spars in green, ribs in orange, and the skin in gray.

The two spars are located respectively at 23 % and 70 % of the chord length, as shown in Figure 6.22. The use of 37 stringers as well as 23 spars placed at equal pitch along the span complement the structural layout of the wing. The structural layout of the wing is complemented by the use of 37 stringers and 23 spars placed at equal intervals along the span. The thickness of the skin, ribs, and spars is considered uniform, set at 0.427 in, in line with the model used in the analytical study. The stringers are all modeled by a Z-shaped bar with a cross-section area of 0.130 in^2 with the corresponding geometry given in Figure 6.24.

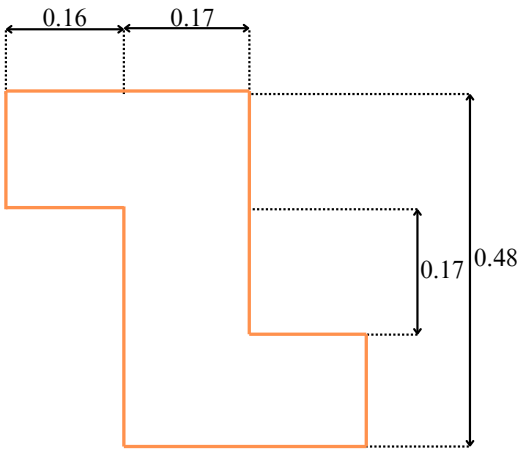

Figure 6.24: Cross-section of the stringer used in the FEM model, with the dimensions in inches.

Meshing, loading and constraints

For simplicity and computational efficiency, the skin, ribs, and spars are modeled using 2D sheet elements, while the stringers are modeled as 1D bar elements. The FEM elements chosen for the spars, ribs and skin are chosen to be triangular elements. Although quadrilateral elements are generally recommended for accuracy, triangular elements are used here to obtain a high-quality mesh for the complex airfoil profile and avoid stress singularity problems in the simulation. The meshes are refined using a convergence study of the principal and shear stress to strike a balance between accuracy and computational time.

The only constraint applied to the wing is a fixed condition at the root, supposing a perfectly rigid transition part. The applied loads are limited to the wing's self-weight and aerodynamic loads. The objective of the simulation is to compare the analytical results with the simulation results. Therefore, the worst-case loading scenario from Table 6.26 is considered.

The lift force is approximated by applying an elliptical on the front rib, as we suppose it represents the aerodynamic centerline of the airfoil. The drag and moment are applied uniformly along the span of the front rib, here again supposed as the aerodynamic centerline. The resulting loading and constraints layout is show in Figure 6.25, with the lift in blue, the drag in green and the aerodynamic moment in red. The green crosses represent the clamped root rib.

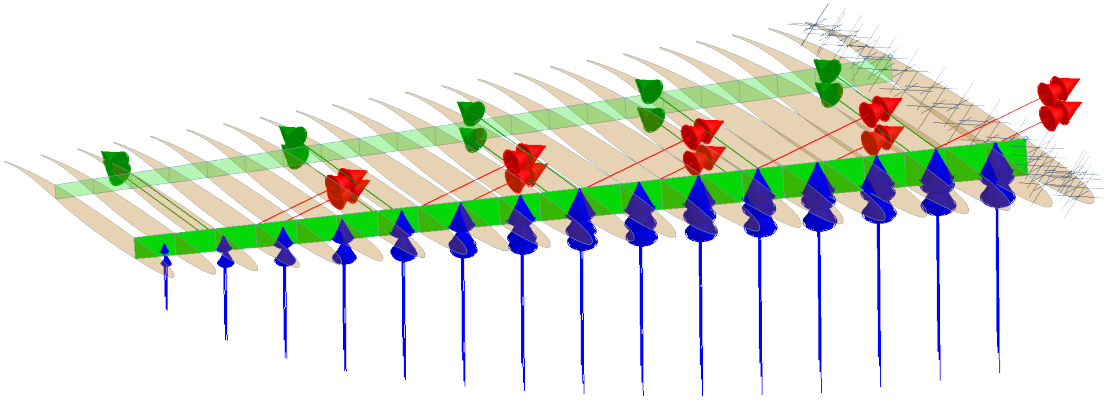

Figure 6.25: Modeled load and constraints distribution on the tapered airfoil with the lift in blue, the drag in green, the aerodynamic moment in red and the clamped root rib in green.

Results

From the result of the simulation, threes quantities have to be analyzed. The shear stress as well as the principal stress extremes are keys to compare our model with analytical results. In Figure 6.26, the maximum displacement of the wing is at the tip of 0.7 in. The huge rigidity performance is discussed at the end of this section.

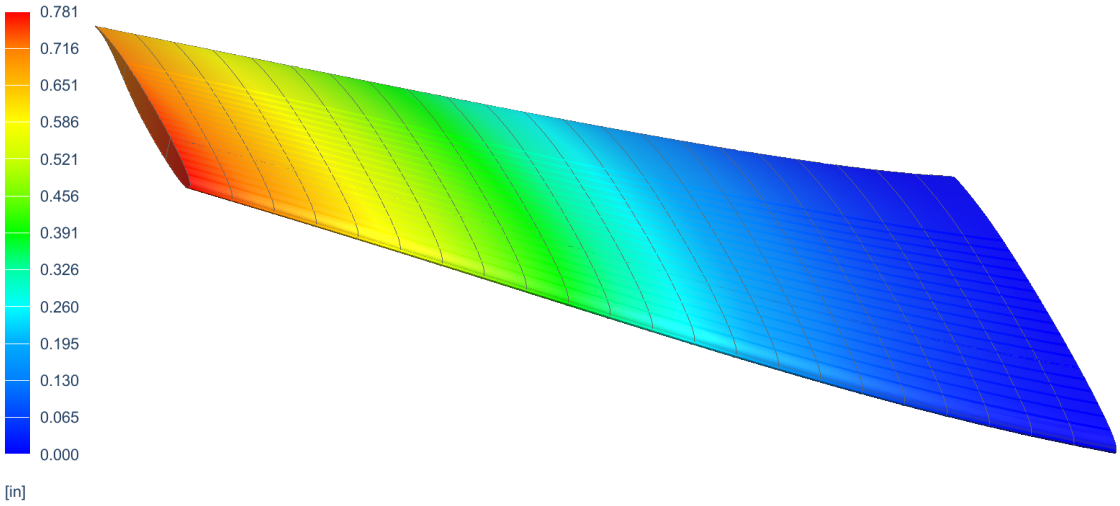

Figure 6.26: Displacement of the wing under extreme loading conditions.

As shown in Figure 6.27, the stringers experience the highest stresses near the root. The stringers on the extrados are subjected to compression, while those on the intrados are in tension. This behavior is consistent with the observed displacement, confirming the expected stress distribution.

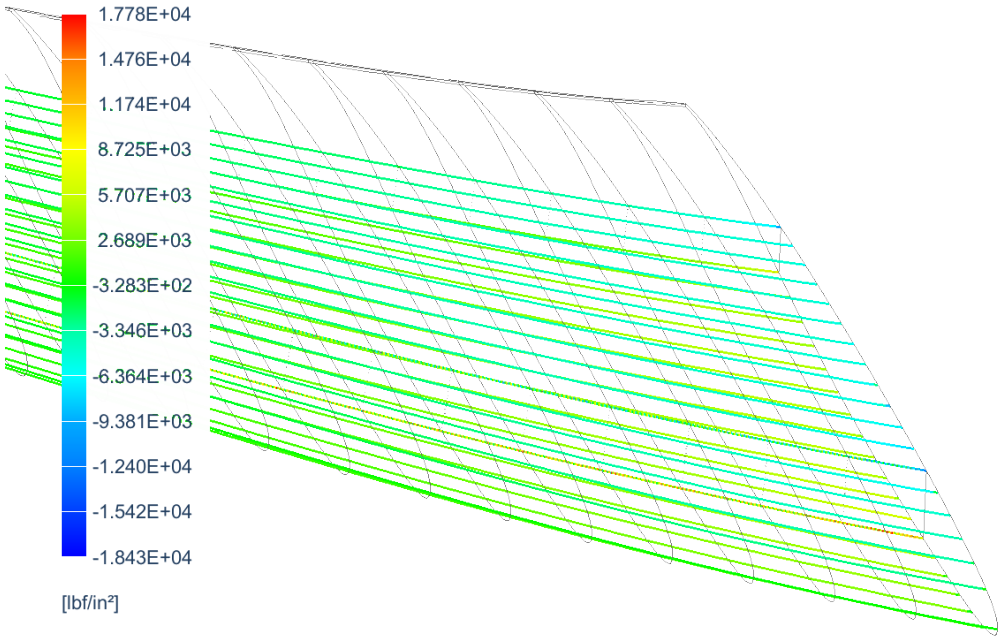

Figure 6.27: Stringer stresses under extreme loading conditions

The maximum shear stress and principal stress along the internal structure of the tapered wing are shown in Figure 6.29 and Figure 6.28. As expected, the maxima for both quantities are located at the root of the wing. Most of the structure does not carry a significant load compared to the root of the wing, justifying the focus on the root in the analytical part of the study.

Similar observations can be made regarding the skin of the fuselage, which experiences high shear stress and principal stress near the wing root. In the simulation, the maxima for the principal stress is located at the spars and the maxima of the shear stress is located on the skin of the wing.

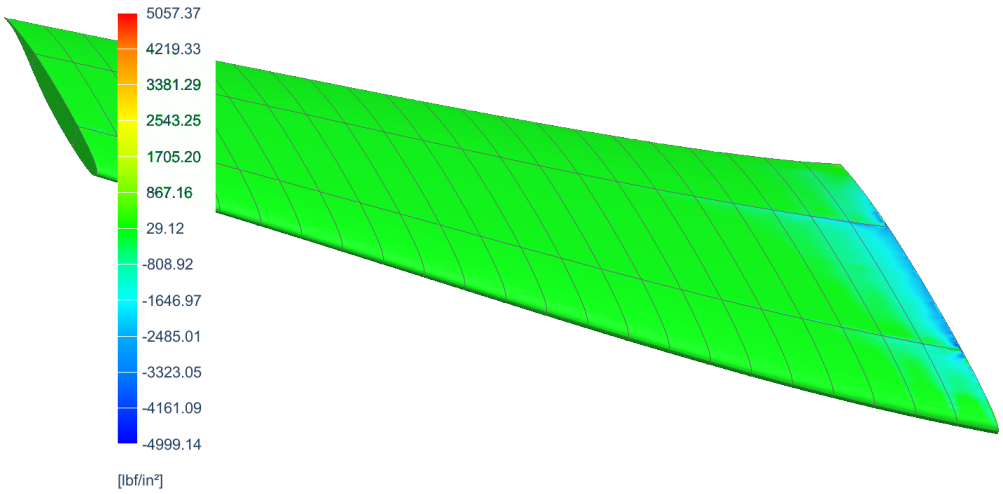

Figure 6.28: Principal stress of the wing under extreme loading conditions.

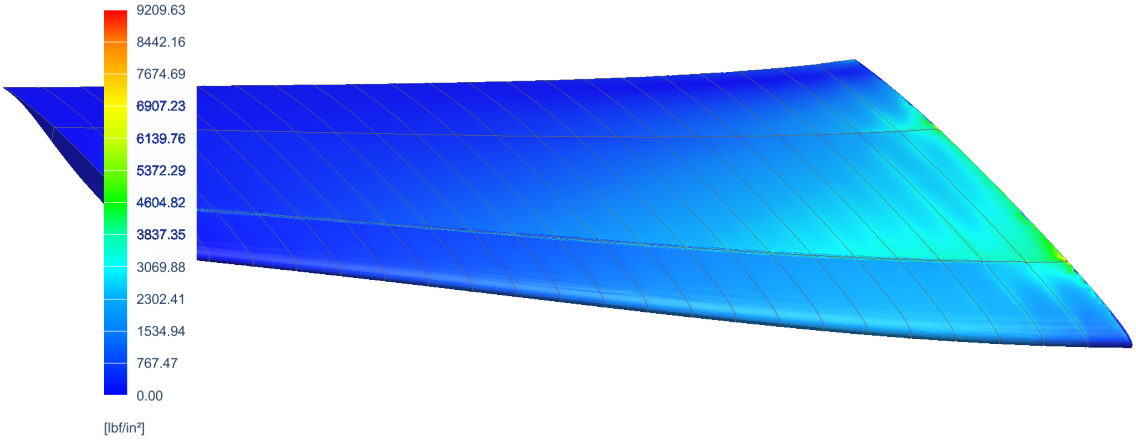

Figure 6.29: Maximum shear stress of the wing under extreme loading conditions.

The maximum values of the studied quantities are summarized in Table 6.28.

	Finite Element Method	Analytical Results
Maximum displacement [in]	0.7	-
Maximum shear stress [ksi]	9.2	9.1
Maximum Principal stress [ksi]	5.1	145
Maximum Direct stress in stringers [ksi]	18.4	145

Table 6.28: Results and comparison with analytical results from the FEM simulation.

In regard to the maximum shear stress, the simulation matches the theoretical results. However, a great difference of estimations for the maximum of the principal stress and the direct stress in the booms is observed. This difference is due to the anisotropic behavior of the chosen CFRP, because the simulation is based on isotropic properties. Thus, the most constraining load case being the shear, the thickness of the skin (and of the spars and ribs) end up being oversize. Although the theory predicts only the equivalent beams to sustain the direct and bending stresses, in reality the 2D elements end up sustaining the majority of it, resulting in an overall decrease of the direct and principal stresses on the wing. This also has an impact on the overall displacement being very low because of this over-reinforcement.

6.6 Performance

6.6.1 Range analysis

From the Breguet range equation, a payload-range diagram is created, in order to analyze the range capabilities of LIFT. This is done on the basis of the performance foundation described by Gudmundsson [32] which shows the relationship between the payload and the fuel weight using propulsion and aerodynamic parameters.
The trend of the payload capacity as a function of the mission range is assessed with respect to the MTOW, cruise segment parameters, and the fuel volume, while also ensuring adherence to the design requirement of a range of 8,000 nm. The payload-range diagram, which illustrates the trade-off between payload and range, is shown in Figure 6.30.

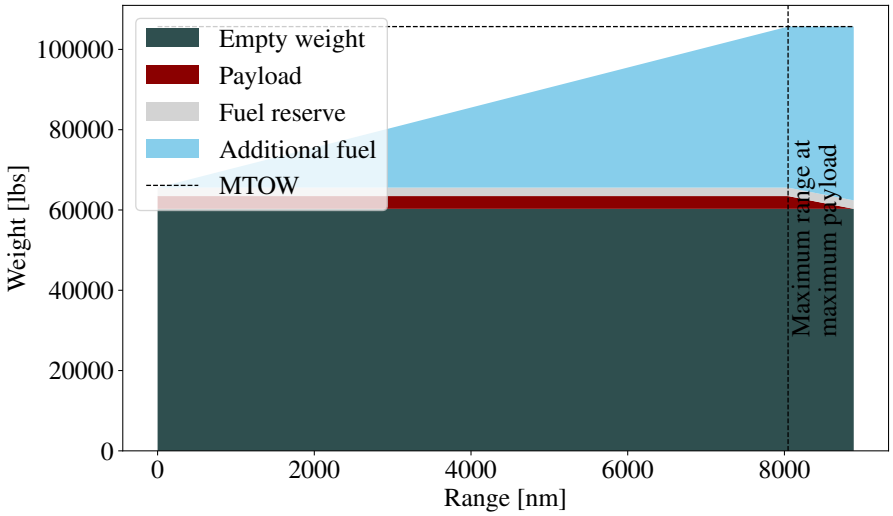

Figure 6.30: Payload-range diagram of LIFT in cruise condition.

The Figure 6.30 shows that at maximum payload of approximately 3,180 lb, LIFT is capable of a range of approximately 8,046 nm. Furthermore, as the payload is reduced, additional fuel can be carried which extends the range to 8,460 nm. Given how the diagram is divided into segments, it shows a good visualization of how fuel distribution differs with the required range.

6.6.2 Takeoff performance

The takeoff performance is computed using the methodology described by Gudmundsson [32], and also implementing adjustments for the difference in density, wind conditions, and the runway slope at each mission airports.

The methodology considers the ground-roll and airborne segments. The decisive parameter is primarily the stall speed, which is calculated with respect to the maximum lift coefficient at the takeoff configuration where high lifting devices are deployed [35]. This leads to a stall speed of 114.88 kt.

The takeoff performance of the aircraft is computed for the there requested missions to ensure the adherence to the AIAA requirements and also to the FAA Part 25 requirements [41].

For all the missions, the climb gradient in the case of One Engine Inoperative (OEI) is analyzed at takeoff safety speed to ensure it's adherence to the minimum of 2.4 % per FAA Part 25 regulations. The table 6.29 gives a breakdown of the takeoff performance parameters. It also shows the robustness of the aircraft in various operating conditions, while meeting all the required criteria.

Parameter	Passenger mission	Aspen mission	Napa mission
Takeoff distance [ft]	4,483.13	4,865.37	5,126.77
Stall speed [kt]	114.88	125.84	131.69
Rotation speed V_R [kt]	126.37	138.42	144.86
Part 25 Compliance	✓ Yes	✓ Yes	✓ Yes

Table 6.29: Takeoff performance summary of the required mission conditions.

As shown in Figure 6.31, the aircraft accelerates from rest using full engine power until it reaches the rotation speed, V_R. During the rotation phase, the pilot increases the angle of attack, allowing the aircraft to lift off the ground. This is followed by the transition segment, where the aircraft establishes a more stable climb attitude. Finally, the aircraft enters the obstacle climb-out phase, during which LIFT climbs at an angle of 3° to clear a 50 ft obstacle, in compliance with AIAA guidelines and FAA Part 25 regulations. The complete takeoff sequence for the Passenger mission from brake release to obstacle clearance is illustrated in Figure 6.31, and the total takeoff distance is $S_{TO} = 4483.13$ ft.

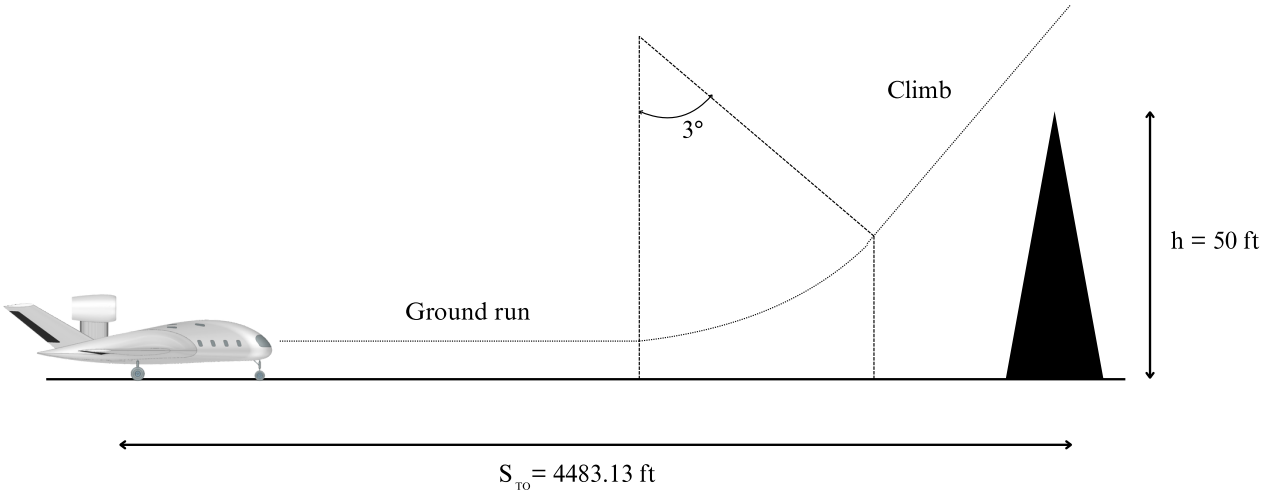

Figure 6.31: Segments of the Passenger mission takeoff maneuver, including ground run, rotation, transition, and climb to a 50 ft obstacle height, according to Gudmundsson [32].

6.6.3 Landing performance

The aircraft's performance in this segment is evaluated by considering the approach speeds, touchdown conditions, braking efficiency, and runway friction characteristics. A detailed summary of the aircraft's landing performance is presented in Table 6.30. It is important to note that the final total landing distances for each mission are adjusted based on the atmospheric and physical characteristics of the airports to provide a more realistic estimate. These distances respect the mission requirements explained in Section 2.

Parameter	Passenger	Aspen	Napa
Approach distance [ft]	1004.05	1004.05	1004.05
Approach time [s]	5.94	4.95	4.52
Rotation distance [ft]	165.27	237.87	285.33
Rotation time [s]	1.16	1.39	1.52
Ground run distance [ft]	2089.82	2099.32	2854.80
Total Landing Distance [ft]	3093.88	3103.37	3858.86

Table 6.30: Landing performance summary of the required mission conditions.

This phase represents the reverse of the takeoff procedure, beginning from the standard 50 ft obstacle height and ending with a complete stop on the runway. As illustrated in Figure 6.32 for the Passenger mission, the landing maneuver is divided into distinct segments. The approach phase begins with LIFT descending toward the runway threshold at a flare angle of 4 degrees. This is followed by the flare segment, during which the aircraft gradually reduces its vertical speed to achieve a smooth touchdown [35]. After contact with the ground, the aircraft enters the free-roll segment, coasting momentarily before brake application begins to bring the aircraft to a complete stop.

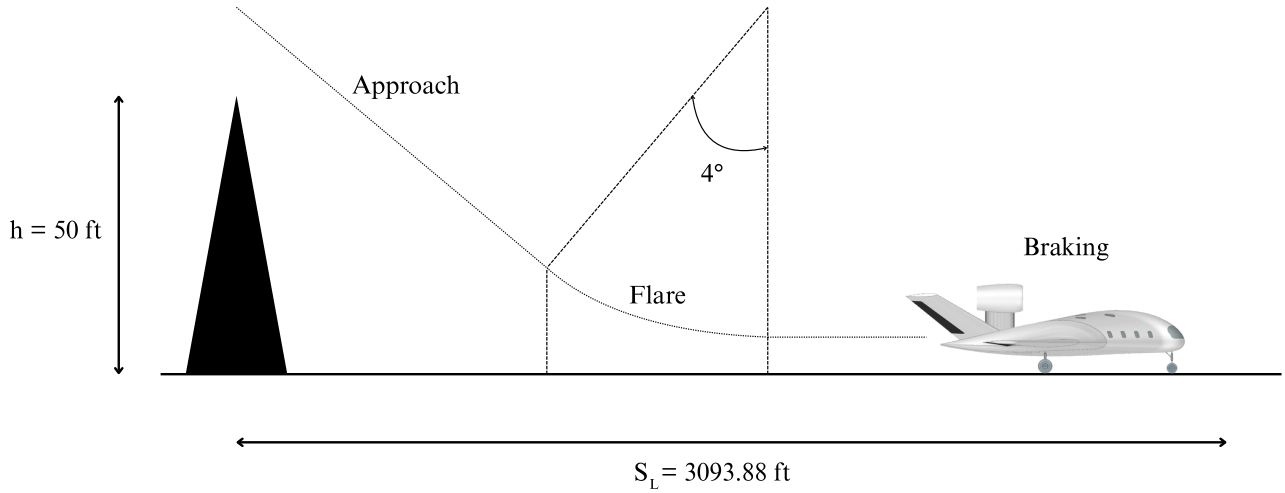

Figure 6.32: Passenger mission landing maneuver profile showing the approach, flare, and braking phases from a 50 ft height obstacle, according to Gudmundsson [32] .

6.6.4 Climb performance

The climb performance of the LIFT is analyzed over a range of altitudes and true airspeed based on the theoretical methodology to determine the climb rate and the best climb speed rate as outlined by John D. Anderson [65] . The aircraft's airspeed varies throughout the flight as the power setting changes, which consequently affects its rate of climb. However, at a specific airspeed, the rate of climb reaches its maximum [32].

The analysis of this flight segment is done by iteratively calculating the excess available thrust at flight conditions to find the Rate of Climb (ROC). The weight used in this analysis was linearly reduced from the beginning of the climb until it reaches the cruise altitude to model a real-life case of the evolution of the fuel burn during the flight phase.

The climb performance of the LIFT is analyzed using the rate of climb (ROC) diagram shown in Figure 6.33. The

altitude where the maximum ROC is 100 ft/min known as the service ceiling [32] is computed to be 51,591 ft and the absolute ceiling where the maximum ROC is 0 ft/min takes place at an altitude of 52,492 ft. The time to climb to the cruising altitude of 41,010 ft using optimal flight configurations is approximately 13 minutes.

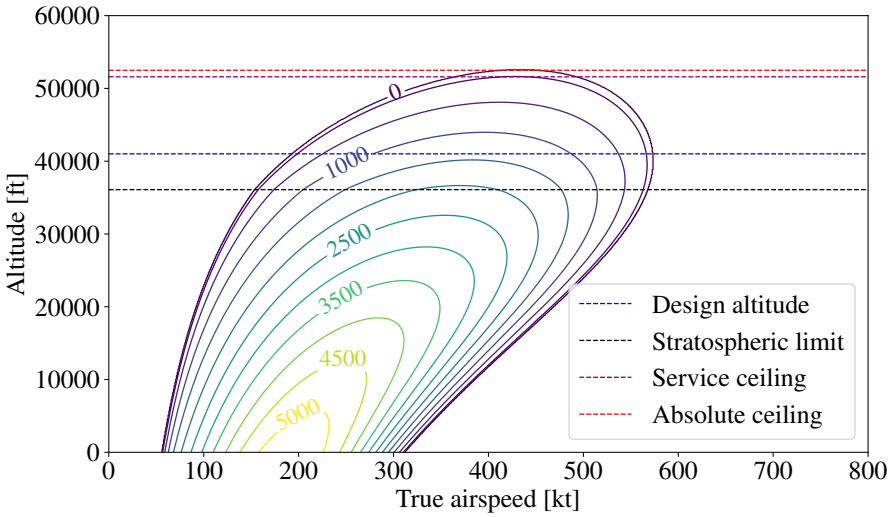

Figure 6.33: Rate of climb diagram.

6.6.5 Turn performance

To analyze the maneuverability performance of LIFT at high altitude, a turn performance diagram is constructed at the cruise altitude of 41,010.5 ft. This is done using the outlined methodology in Raymer and Anderson [35, 65], which features the capability of the aircraft under aerodynamic and propulsion constraint. Figure 6.34 illustrates the relationship between turn rate and true airspeed. To analyze the maneuvering capabilities, the analysis used the following constraints:

- Stall limit: It is gotten from the maximum lift coefficient at cruise ($C_{L_{\max}} = 1.329$). This shows the allowable turn rate at each airspeed, below this limit, the aircraft cannot produce enough lift to sustain a level turn [65].
- Thrust limit: This constraint shows the point were the available thrust equals the aerodynamic drag, after this point the aircraft cannot sustain a turning flight. Thrust lapse model which considers the mach and altitude effect is used as given by Gudmundsson[32].
- Load Factor Curves: This curves which ranged from $n_z = 1.45$ to $n_z = 3.0$ in Figure 6.34, helps to show the structural demand relating to the intensity of the turn. These curves highlight the increase in bank angles and the structural loads experienced by the aircraft during turns.
- Constant Turn Radius Lines: These lines highlights the geometric implications of the various turning rate at different airspeed.
- Corner Speed: This is the point of intersection between the stall limit and the thrust limit. This point shows the maximum allowable turn rate of the aircraft without exceeding structural, aerodynamic and thrust limits [35].

From Figure 6.34, it can be seen that LIFT achieves a maximum sustainable turn rate of 0.0915 rad/s at a corner speed of 313.8 kt. After the intersection, the available thrust isn't sufficient to maintain a tighter turn at high load factors. This performance analyses is crucial to check the compliance of the aircraft's handling qualities with structural, aerodynamic and propulsive limits and make sure they adhere to the certifying regulations.

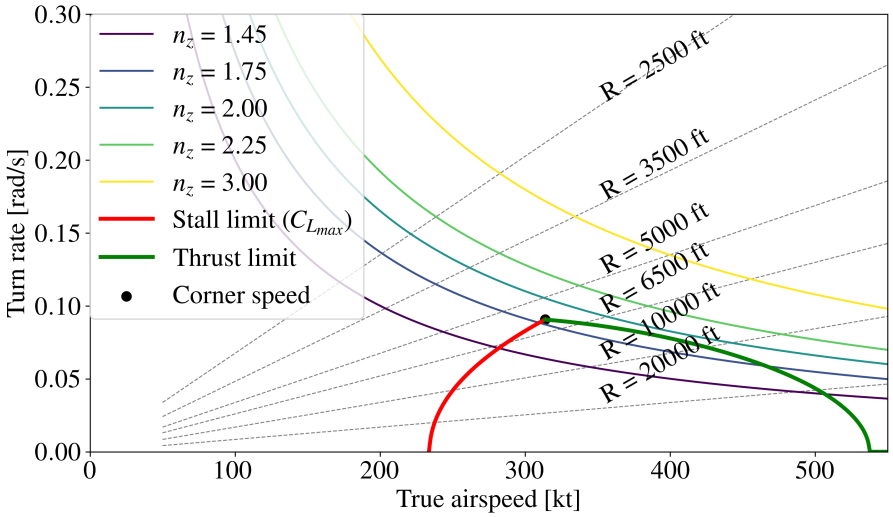

Figure 6.34: Turn rate and corner speed diagram at cruise altitude.

Chapter 7. Trade off

7.1 Airfoil selection of the inner wing

As the design is mainly influenced by the pitching down moment of the inner wing airfoil, it can be varied in order to analyze the changes on the equilibrium and stability and drag. Because LIFT flies at Mach 0.9, the behavior at high speed of the airfoil is important. Therefore, it is interesting to replace the inner wing airfoil by a supercritical airfoil, which stands for a behavior adapted to transonic speeds. Table 7.1 compares the selected reflex NACA 45118 airfoil and highlights the main differences between both.

	NACA 45118	SC(2) 0518	Conclusion
Behavior for transonic speed	Not adapted	Adapted	More drag
Pitching moment coefficient [-]	-0.0293	-0.1849	+ 15.85%
Horizontal tail area [ft^2]	114.83 ft^2	196.85 ft^2	+71.43 %
Span of the horizontal tail [ft]	21.43	70.3	+228.04%

Table 7.1: Comparison between the reflex NACA 45118 airfoil and the SC(2) 0518 supercritical airfoil for the inner wing.

Even if the supercritical airfoil generates a lower drag, it requires incoherent tail dimensions (for a same angle of attack), that can lead to structural problems. Having a horizontal tail of a span that represents 74% of the total span is nonsensical. Besides, the complexity and the cost of the tail manufacturing process would be higher due to its size.

7.2 Engines selection

Once the engine type is selected, it is interesting to compare several turbofan engines in order to select the most suitable one for the LIFT missions. The different engines that are selected to be compared are the selected Pratt & Whitney PW1521G, CFM LEAP-1A, Rolls-Royce Pearl 15 and GE Passport 20. They are all usually used for a comparable application to LIFT. Table 7.2 presents a comparison between them. It is important to note that the TSFC are from approximate average values gotten from public sources, as the exact operational values are proprietary. The thrust available in Table 7.2 is the uninstalled thrust.

Engine	Thrust [lbf]	Bypass Ratio	Average TSFC [lb/lbf/hr]	Dry weight [lb]
Pratt & Whitney PW1521G	21,970	12:1	0.52	4,800
CFM LEAP-1A	24,500	11:1	0.545	6,130
Rolls-Royce Pearl 15	15,250	4.8:1	0.58	4,032
GE Passport 20	20,000	5.6:1	0.56	4,554

Table 7.2: Comparison of data between the Pratt & Whitney PW1521G, CFM LEAP-1A, Rolls-Royce Pearl 15 and GE Passport 20 engines.

Since the CFM LEAP-1A provides the higher thrust, it will be directly compared to the Pratt & Whitney PW1521G,

as done in Table 7.3.

	Pratt & Whitney PW1521G	CFM LEAP-1A	Conclusion
Uninstalled thrust [lbf]	21,970	24,500	-10.33%
Bypass Ratio	12:1	11:1	Better
Average TSFC [lb/lbf/hr]	0.52	0.545	-4.59%
Dry weight [lb]	4,800	6,130	-21.7%
Fan diameter [ft]	6.58	6.5	+1.23%
Overall length (flange to flange) [ft]	9.99	10.92	-8.52%

Table 7.3: Direct comparison based on performance and geometrical parameters between the selected Pratt & Whitney PW1521G engine and the CFM LEAP-1A.

Even if the Pratt & Whitney engine produces a lower thrust than the CFM LEAP-1A, it fulfills the mission requirements given by AIAA. Therefore, a higher thrust is not needed. Besides, the bypass ratio is higher for the PW1521G, which allows to reduce the generated noise and increase the propulsive efficiency. Furthermore, the PW1521G TFSC is lower, which is an advantage.

While the fan diameter is increased, even if it is not significant, the overall length of the PW1521G engine is lower, which is a good point concerning the generated drag.

In terms of stability, equilibrium and performance, the dry weight of the engine is also critical. A lower engine weight reduces the MTOW, which is better. Concerning the center of gravity position, a lighter engine is also preferred, since it prevents shifting it rearward.

Additionally, it has a superior propulsive efficiency due to its Geared Turbo fan architecture which will tailor the thrust needs according to the mission segments [40].

These factors collectively indicate that the PW1521G is the most appropriate engine choice for LIFT.

Chapter 8. Cost analysis

The cost analysis of LIFT is critical to ensure not only the technical feasibility but also its financial viability in supporting efficient production and operation in the ultra-premium long-range jet market. To better estimate the cost of operations and development, the Eastlake Model was employed. This model is a modified version of the Development and Procurement Cost of Aircraft (DAPCA-IV) model. Eastlake corrects the discrepancies by adapting better cost estimation relationships to more accurately predict the realities of aircraft design, manufacturing, and certification, particularly for aircraft certified under FAA Part 25.

Quantity discount factor (QDF) was included in the calculation to account for the reduced cost due to the number of units produced [32]. The Eastlake model defines the QDF as $\text{QDF} = \left(F_{\text{Exp}}\right)^{1.4427 \cdot \ln N}$, where F_{Exp} represents the experience effectiveness factor that was selected as 90 %, this represents 10% cost reduction per unit for the production run which better matches the real production cost and N is the number of units produced, this was applied to the variable production cost for 200 units over 5 years.

8.0.1 Man-hours calculation

The development of LIFT requires a realistic and thorough estimation of man-hours, encompassing all stages from engineering and tooling to manufacturing, to ensure effective resource allocation. The Eastlake model, as described by Gudmundsson [32], was used to estimate these man-hours for a business jet certified under FAA Part 25.

The estimation is based on the airframe weight (4030.73 lb), cruise speed (517 kt), and a production rate of 5 units per month. The following equations were applied to compute the man-hour requirements for engineering, tooling, and manufacturing.

$$H_{\text{ENGR}} = 4.86 \cdot W_{\text{airframe}}^{0.777} \cdot V_H^{0.894} \cdot N^{0.163} \cdot F_{\text{CERT1}} \cdot F_{\text{CF1}} \cdot F_{\text{COMP1}} \cdot F_{\text{PRESS1}}. \tag{8.1}$$

As shown in Equation 8.1, the engineering man-hours are a function of airframe weight, velocity, and several correction factors.

$$H_{\text{TOOL}} = 5.99 \cdot W_{\text{airframe}}^{0.777} \cdot V_H^{0.696} \cdot N^{0.263} \cdot F_{\text{CERT2}} \cdot F_{\text{TAPER2}} \cdot F_{\text{CF2}} \cdot F_{\text{COMP2}} \cdot F_{\text{PRESS2}}. \tag{8.2}$$

Tooling man-hours, calculated using Equation 8.2, depend on similar parameters, with additional factors accounting for wing taper and other structural complexities.

$$H_{\text{MFG}} = 7.37 \cdot W_{\text{airframe}}^{0.82} \cdot V_H^{0.484} \cdot N^{0.641} \cdot F_{\text{CERT3}} \cdot F_{\text{CF3}} \cdot F_{\text{COMP3}}. \tag{8.3}$$

Equation 8.3 provides the estimate for manufacturing man-hours, incorporating airframe weight, design speed, production quantity, and relevant correction factors.

The resulting man-hours for a production run of 100 units are summarized in Table 8.1.

Variable	Value[hr]
Number of engineering man-hours	31,948,441.14
Number of tooling man-hours	18,099,093.82
Number of manufacturing man-hours	50,074,766.64

Table 8.1: Engineering, tooling, and manufacturing man-hours for 100 produced units.

8.0.2 Fixed cost

The fixed cost for LIFT, which includes engineering, development support, and flight test operations, was calculated using the Esatlake cost model to ensure consistency and reliability. These costs are independent of production volume and serve as a baseline for the research, development, test, and evaluation (RDT&E) budget. The following equations were used in the analysis:

$$C_{\text{ENGR}} = H_{\text{ENGR}} \cdot R_{\text{ENGR}} \cdot \text{CPI}_{2012}. \tag{8.4}$$

Equation 8.4 estimates the engineering cost, where $R_{\text{ENGR}} = 127.92\$$ represents the labor rate, which includes various costs such as overhead, benefits, and other related expenses. The Consumer Price Index (CPI) is set to 1.38 for some costs, reflecting adjustments based on historical data. For costs where up-to-date rates are available, the CPI is considered as 1.

$$C_{\text{TOOL}} = H_{\text{TOOL}} \cdot R_{\text{TOOL}} \cdot \text{CPI}. \tag{8.5}$$

Equation 8.5 calculates the tooling cost, where $R_{\text{TOOL}} = 84.82\$$ is the applicable tooling labor rate.

$$C_{\text{DEV}} = 95.24 \cdot W_{\text{airframe}}^{0.63} \cdot V_H^{1.3} \cdot \text{CPI}_{2012} \cdot F_{\text{CERT5}} \cdot F_{\text{CF5}} \cdot F_{\text{COMP5}} \cdot F_{\text{PRESS5}}. \tag{8.6}$$

Equation 8.6 calculates the cost of development support based on aircraft weight, design speed, and several correction factors. Lastly, Equation 8.7 determines the cost of flight test operations, where $N_P = 3$ is the number of prototypes.

$$C_{\text{FT}} = 2606.51 \cdot W_{\text{airframe}}^{0.325} \cdot V_H^{0.822} \cdot N_P^{1.21} \cdot \text{CPI} \cdot F_{\text{CERT6}}, \tag{8.7}$$

The total fixed cost for a five-year production run of 300 units is summarized in Table 8.2.

Variable	Cost per unit [$]
Total cost of engineering	13,622,815.30
Total cost of tooling	5,117,217.13
Total cost of development support	2,147,188.20
Total cost of flight test operations	370,537.45
Total fixed cost	21,257,758

Table 8.2: Total fixed cost for 300 produced units.

8.0.3 Variable cost

Unlike fixed costs, variable costs fluctuate based on production volume and are directly proportional to the number of units produced. These costs include manufacturing labor, materials, quality control, and vendor-supplied components. The total variable cost per unit is calculated by summing these expenses and dividing by the total number of units expected to be produced [32].

Variable	Cost per unit [$]
Manufacturing labor	11,562,029.94
Materials & Equipments	10,864,002.66
Quality control	3,459,937.46
Avionics	1,180,221
Landing gear	1,967,036
Propulsion	7,359,673
Manufacturer's liability insurance	750,000
Total variable cost	37,142,900

Table 8.3: Variable cost breakdown per unit for 300 produced units.

Table 8.3 presents the detailed breakdown of variable costs per unit. These values are based on a production run of 300 units and reflect the direct expenses incurred for each aircraft produced.

8.0.4 Sensitivity of production quantity on minimum selling price

This section examines how the minimum selling price (MSP) varies with the number of units produced. Following the Eastlake model described by Gudmundsson [32], the MSP is calculated by dividing the total fixed (nonrecurring) cost by the number of units produced and adding the unit variable cost. The formula is expressed as:

$$\text{Minimum selling price} = \frac{C_{\text{fixed}}}{N} + C_{\text{variable}}, \tag{8.8}$$

where $C_{\text{fixed}} = \$5.47$ billion is the total nonrecurring cost, and $C_{\text{variable}} = \$37.14$ million is the variable cost per aircraft, as detailed in Section 8.3.

Figure 8.1 illustrates the relationship between the MSP and the number of units produced. As expected, the MSP decreases with increased production due to economies of scale. However, beyond approximately 500 units, the reduction in MSP begins to plateau, indicating diminishing returns in cost reduction.

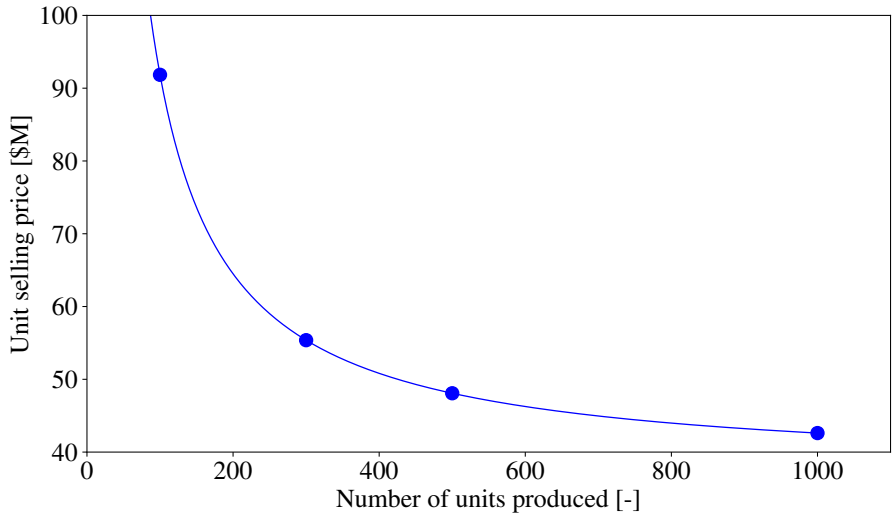

Figure 8.1: Minimum selling price as a function of units produced, based on the Gudmundsson [32] cost model.

8.1 Annual and operational cost

This section provides a comprehensive breakdown of the annual and operational costs associated with operating the LIFT aircraft. These figures are important for establishing a realistic and competitive cost of ownership, helping prospective customers understand the recurring expenses necessary to maintain airworthiness and flight readiness.

The estimates are based on the EASTLAKE Direct Operating Cost (DOC) model, which focuses on costs directly affecting flight operations. Table 8.4 presents the annual costs, including crew salaries, maintenance, insurance, fuel, training, and other essential items.

Variable	Cost [$]
Pilot	175,000
Co-pilot	120,000
Flight attendant	100,000
Benefits	118,500
Hangar	25,000
Maintenance cost	96,000
Insurance hull	700,000
Single limit liability	50,500
Inspection cost	12,000
Overhaul cost	750,000
Aircraft modernization	25,000
Weather service	3,000
Recurrent training	30,000
Refurbishing	70,000
Navigation chart service	7,000
Landing & handling fees	8,000
Fuel cost $(2.1\$\ pergallon)$	210,000
Computer program	20,000
Total cost	2,520,000
Cost per flight Hour	5,040

Table 8.4: Annual operational cost breakdown for LIFT.

8.1.1 Break-even analysis

Using the Eastlake cost model, the minimum selling price—incorporating Research, Development, Test, and Evaluation (RDT&E) expenses is estimated at approximately $54.6 million. This figure reflects the complexity and advanced capabilities expected of an ultra-premium, long-range business jet. Additionally, the annual operational cost is estimated at $2.52 million, corresponding to a Direct Operating Cost (DOC) of approximately $4 per nautical mile.

To ensure profitability, a break-even analysis was performed assuming a total production of 300 units over a 5-year period. A profit margin of 20% was added to the minimum selling price, yielding a unit sales price of approximately $66.5 million. Based on this estimate, the break-even point is reached after the production of 187 units, which is expected to occur within the third year of production. This positions LIFT as a competitive solution in the ultra-premium long-range market, while ensuring compliance with FAA Part 25 certification requirements.

To further evaluate economic robustness, a parametric break-even analysis was conducted using three different selling prices: $60.9 million (10% below the base price), $66.5 million (base case), and $72.0 million (10% above the base price). These variations represent conservative, baseline, and optimistic pricing strategies, respectively. Using the fixed and variable costs defined in Section 8.0.4, total revenue was calculated for each case, and the corresponding break-even points were identified—i.e., the production quantity at which cumulative revenue equals total incurred cost [32]. The results are illustrated in Figure 8.2.

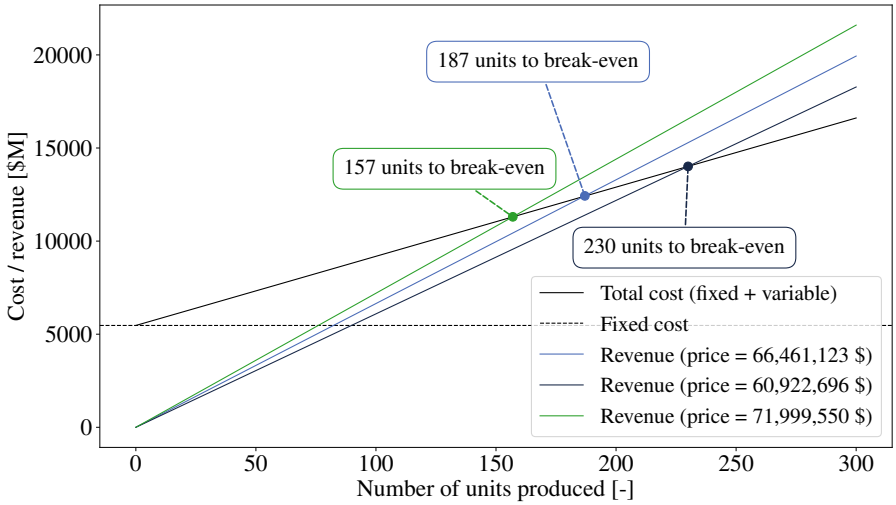

Figure 8.2: Break-even analysis at different unit prices.

Figure 8.2 demonstrates that the fixed (nonrecurring) cost remains unchanged across scenarios. The varying slopes of the revenue lines are driven by the unit selling prices, which directly affect how quickly the break-even point is reached. A higher selling price accelerates break-even, while a lower price delays it. This highlights the critical balance between pricing strategy and financial risk, emphasizing how relatively small adjustments in unit price can substantially impact the economic viability of the aircraft program.

8.1.2 Life cycle cost analysis

According to Gudmundsson [32], the Life Cycle Cost (LCC) represents the total cost associated with an aircraft from its development to its retirement. To assess the long-term economic feasibility of LIFT, the LCC methodology proposed by Gudmundsson is applied. This approach accounts not only for acquisition costs but also includes annual fixed operational costs and variable costs that scale with flight hours. The objective is to evaluate whether LIFT remains cost-effective over its operational lifespan compared to similar aircraft in the business jet category.

The LCC can be expressed as:

$$\text{LCC} = P_{\text{purchase}} + N_{\text{periods}} C_{\text{fixed}}^{\text{op}} + N_{\text{flight hours}} C_{\text{op}}^{\text{var}}, \tag{8.9}$$

where P_{purchase} is the aircraft purchase price, N_{periods} is the service duration, $C_{\text{fixed}}^{\text{op}}$ is the annual fixed operational cost, $N_{\text{flight hours}}$ is the annual flight time, and $C_{\text{op}}^{\text{var}}$ is the variable cost per flight hour.

Based on earlier findings, the purchase price of LIFT is \$66,461,123. The aircraft is expected to remain in service for 30 years, with an annual fixed operational cost of \$2,520,000. It is projected to fly approximately 500 hours per year, and the variable operational cost is estimated at \$5,040 per flight hour. With this, the total life cycle cost of the aircraft is approximately \$217.66 million. To contextualize this LCC, it is compared with Dassalut Falcon 10X in Chapter 9.

8.2 Life cycle emission assessment

In recent years, the aviation industry has placed increasing emphasis on reducing its carbon footprint and overall environmental impact. The Blended Wing Body (BWB) configuration offers a promising approach by enhancing aerodynamic efficiency and improving fuel economy compared to conventional tube-and-wing aircraft designs. This Life Cycle Assessment (LCA) evaluates the environmental impacts of the aircraft from a cradle-to-grave perspective, encompassing all phases from raw material extraction and manufacturing, through operational use and maintenance, to eventual end-of-life disposal or recycling. By considering the full life cycle, the LCA provides a comprehensive understanding of the sustainability performance of the BWB design.

8.2.1 Methodology

The analysis assumes a full operational lifetime of 30 years, with 500 flight hours annually at a target cruise speed of 517 knots. This corresponds to an anticipated total operational distance of approximately 7.75 million nautical miles, servicing 8 passengers.

The Attributional LCA approach [66] is employed to estimate the average environmental impact over the aircraft's lifespan, using established emission factors. The phases included in the assessment are: raw material extraction and processing, manufacturing, operations, maintenance, and end-of-life disposal and recycling.

The emission factors utilized in this analysis are sourced from the Ecoinvent database, a comprehensive and widely recognized life cycle inventory resource. Additionally, a Radiative Forcing Index (RFI) of 2 is applied to account for non-CO_2 effects associated with high-altitude emissions during cruise conditions [67].

The results of the Life Cycle Assessment (LCA) are summarized in Table 8.5. As observed, the operational phase dominates the overall emissions, primarily due to fuel combustion during flight. Despite the improved aerodynamic and fuel efficiency of the Blended Wing Body configuration compared to traditional tube-and-wing aircraft, fuel consumption remains the largest contributor to the aircraft's environmental impact. This underlines the importance of further optimizing the operational phase and exploring the integration of low-emission propulsion technologies, such as hydrogen-based systems or Sustainable Aviation Fuel (SAF).

The total life cycle emissions is calculated to be approximately 190 million lb CO_2-eq, resulting in an emissions intensity of 1.103 lb CO_2-eq per passenger-kilometer. Although this value is relatively high compared to larger commercial aircraft, it reflects the limited passenger capacity of this ultra-premium business jet.

End-of-life considerations is also included in the assessment. A recycling credit is applied based on the assumption that 80% of the airframe mass is recyclable, while only 20% of the composite material can be effectively recovered through pyrolysis or mechanical processing. This credit, reflected as a negative emission value, contributes to a modest reduction in total environmental impact.

Phase	Emissions [lb CO_2-eq]
Raw Material Extraction and Processing	1,342,128
Manufacturing	541,613
Operation (with RFI)	188,198,065
Maintenance	541,613
End-of-Life Disposal and Recycling	-563,177
Total	190,060,242
Emissions per Passenger-kilometer	1.10315

Table 8.5: Life cycle emissions breakdown of LIFT in lb CO_2-equivalent.

Chapter 9. Comparison

Once the complete design is described and analyzed, LIFT is compared on the same quantities that are described in Section 4.2.1. The goal of this comparison is to evaluate the competitiveness of LIFT on the ultra premium long range business jets market. Table 9.1 presents a comparison between LIFT and the Dassault Falcon 10X, which is currently one of the newest aircraft in this segment.

Quantity to compare	Value for LIFT	Value for Dassault Falcon 10X	Conclusion
Unit price [$]	66,461,123	75,000,000	-11.39%
DOC [$/nm]	4	4	Same
Max passengers	8	19	-11
Cruise Mach [-]	0.9	0.925	-2.7%
Wingspan [ft]	94.98	110	-13.64%
Max cabin height [ft]	8.1	6.67	+21.44%
Cabin width [ft]	29.17	9.1	+220.55%
Range [nm]	8,000	7500	+6.67%
Takeoff distance [ft]	4,483.1	5930	-24.4%
Landing distance [ft]	3,093.88	2470	+25.26%

Table 9.1: Comparison between LIFT and Dassault Falcon 10X. Green values indicate superior LIFT characteristics, while red values indicate advantages of the Falcon 10X.

From Table 9.1, it can be concluded that LIFT could have a rightful place in the ultra premium long range business jet market. Although it accommodates fewer passengers (8 vs. 19), it offers a superior passenger experience with an 850.35 ft^2 spacious, home-like cabin featuring a high ceiling. The minimum cabin height is 5.58 ft, allowing for a fully habitable interior. While the landing distance is longer for LIFT, it still complies with the requirements set by AIAA.

With a projected selling price of approximately $66.5 million and a DOC of $4 per nautical mile, LIFT is competitively positioned. The break-even point at 187 units over 3 years demonstrates its financial viability.

Additionally, life cycle costs (LCC) of both aircraft are compared in Table 9.2. The LCC analysis for LIFT is detailed in Section 8.1.2.

Aircraft	Estimated LCC
Dassault Falcon 10X	$185–195 million
LIFT	$217.66 million

Table 9.2: Estimated life cycle cost comparison between Falcon 10X and LIFT.

Table 9.2 shows that LIFT has a higher LCC, mainly due to the innovative BWB configuration which entails increased maintenance and infrastructure costs. Being relatively early-stage technology, it also benefits from limited support networks. However, the BWB's superior aerodynamic efficiency and enhanced cabin comfort justify this premium positioning.

Another useful comparison is between range and Maximum Takeoff Weight (MTOW). As illustrated in Figure 9.1, LIFT exhibits a competitive maximum range of approximately 8,000 nm while maintaining a relatively low MTOW of 105,500 lb. This highlights the efficiency of design choices made during configuration selection and conceptual design stages.

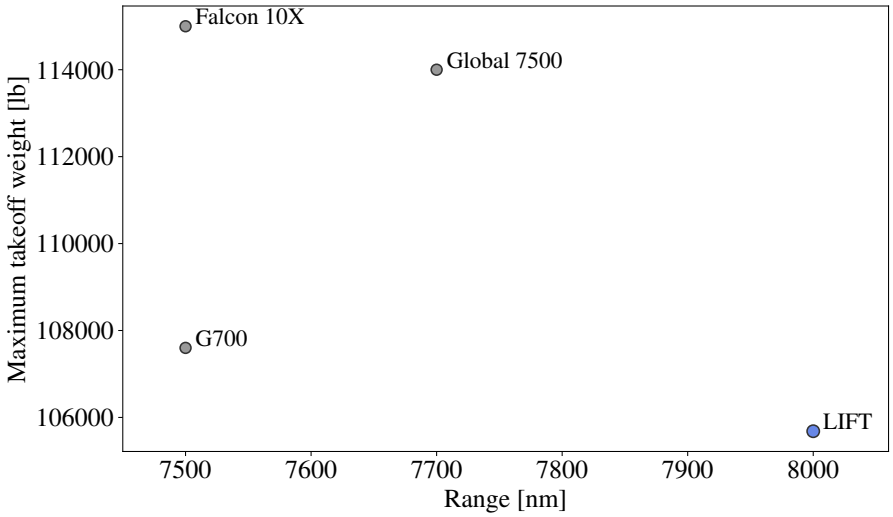

Figure 9.1: MTOW as a function of range for LIFT, Dassault Falcon 10X, Gulfstream G700, and Bombardier Global 7500.

Finally, LIFT is equipped with the latest Pratt & Whitney engines, further strengthening its market position by leveraging state-of-the-art propulsion technology. This supports its potential to meet and possibly exceed current market expectations.

Chapter 10. Conclusion

LIFT project embodies a bold step forward in business aviation, pushing the boundaries of aerodynamic efficiency, operational versatility, and onboard luxury. Developed in response to the 2024–2025 AIAA Graduate Team Aircraft Design Competition, this blended wing body configuration sets a new benchmark in its category. This report outlines the design methodology, based on a combination of numerical tools and empirical methods, such as *DARTFlo*, Siemens NX, and DATCOM method.

Powered by its Pratt & Whitney PW1521G turbofan engines, LIFT achieves a cruise Mach number of 0.9 and range of 8,000 nm, making it an optimal solution for long-range business travel. Additionally, with its wingspan of 94.98 ft, its takeoff distance of 4,483.1 ft and landing distance of 3,093.88 ft, LIFT can operate from a wide range of airports, including short and high-altitude runways, offering a level of flexibility that many other business jets cannot ensure.

With its C_L of 0.45 and its 0.0265 C_D, LIFT has a L/D of 16.95, which reduces significantly its environmental impact, while having a higher lift to drag ratio than the business jets currently available on the market. Furthermore, the use of high-performance composite materials increases the mechanical performance, while leading to a MTOW of 105,682 lbs.

LIFT configuration not only meets aerodynamic and structural objectives, but also redefines the standard of on-board comfort. The innovative cabin layout, designed to carry up to 8 passengers, allows a home-like interior of 850.35 ft^2, aiming to set a new benchmark in luxury and comfort within the business jet market. Passengers benefit from a 161.61 ft^2 meeting room, that allows the customers to plan meetings together. Thanks to its queen-size bed, the bedroom, which measures 59.25 ft^2, provides exceptional comfort and rest during long-haul missions.

From the economic aspect point of view, LIFT is highly competitive, with an estimated selling price of $66,461,123, and operating costs within market expectations. Moreover, the environmental aspect is considered with the analysis of the global life cycle and the compatibility with sustainable aviation fuels.

In summary, LIFT is not just a concept, it is a vision of the future of business aviation, where speed, sustainability, comfort, and versatility converge. This report lays a solid foundation for further development, including high-fidelity CFD and FEM validations, and the potential realization of a scaled demonstrator. As the aviation industry continues to evolve, LIFT stands as a clear contender to redefine what a next-generation business jet can and should be.

Bibliography

[1] International Air Transport Association. *Global Air Passenger Demand Reaches Record High in 2024*. https://www.iata.org/en/pressroom/2025-releases/2025-01-30-01/. Accessed: 2025-02-13. 2025.

[2] Federal Aviation Administration. *Business Jet Report: January 2025 Issue*. https://aspm.faa.gov/apmd/sys/bjpdf/b-jet-202501.pdf. Accessed: 2025-02-13. 2025.

[3] American Institute of Aeronautics and Astronautics. *AIAA Design Competitions*. Accessed: 2025-05-14. 2025. URL: https://aiaa.org/get-involved/university-students/design-competitions/.

[4] Federal Aviation Administration. *FAR Part 91.205 - Instrument and Equipment Requirements*. Accessed April 2025. 2023. URL: https://www.ecfr.gov/current/title-14/chapter-I/subchapter-F/part-91/section-91.205.

[5] *Van Nuys Airport*. Accessed: 2025-04-22. 2025. URL: https://www.iflyvny.com/.

[6] *Aspen-Pitkin County Airport*. Accessed: 2025-04-22. 2025. URL: https://www.airnav.com/airport/kase.

[7] *Napa County Airport*. Accessed: 2025-04-22. 2025. URL: https://www.airnav.com/airport/KAPC.

[8] *Mexico City Airport*. Accessed: 2025-04-22. 2025. URL: https://themexicocityairport.com/information/.

[9] Egbert Torenbeek. *Synthesis of subsonic airplane design*. eng. Cham, 1976. ISBN: 9029825057.

[10] John T. Correll. "Jack Northrop and the Flying Wing". In: *Air & Space Forces Magazine* (2016). Accessed: 2025-02-13. URL: https://www.airandspaceforces.com/article/jack-northrop-and-the-flying-wing/.

[11] Skytamer.com. *Northrop YB-49 Flying Wing Bomber (N-50)*. https://www.skytamer.com/Northrop_1947_N-50_YB-49.html. Accessed: 2025-02-13.

[12] U.S. Air Force. *B-2 Spirit*. https://www.af.mil/About-Us/Fact-Sheets/Display/Article/104482/b-2-spirit/. Accessed: 2025-02-13.

[13] JetZero. *JetZero Official Website*. https://www.jetzero.aero/. Accessed: 2025-02-13.

[14] JetZero. *United Airlines invests in JetZero*. Accessed April 2025. Apr. 2025. URL: https://www.jetzero.aero/united-investment-announcement.

[15] Airbus. *Airbus reveals new zero-emission concept aircraft*. https://www.airbus.com/en/newsroom/press-releases/2020-09-airbus-reveals-new-zero-emission-concept-aircraft. Accessed: 2025-02-13. 2020.

[16] NASA. *X-48 Blended Wing*. https://www.nasa.gov/image-article/x-48-blended-wing/. Accessed: 2025-02-13.

[17] Yingchun Chen Zhenli Chen Minghui Zhang. "Assessment on critical technologies for conceptual design of blended-wing-body civil aircraft". In: *Chinese Journal of Aeronautics* (2019).

[18] Michael Gobel Andreas Wittenberg Fabian Neumann. "Blended Wing Body Chances and Problems of a new Aircraft Concept". In: *Linkoping University* (2017).

[19] Paulinus Peter Chukwuemeka Okonkwo. "Conceptual Design Methodology for Blended Wing Body Aircraft". PhD Thesis. Cranfield University, May 2016.

[20] *Gulfstream G700*. Accessed: 2025-04-22. 2025. URL: https://the-jet-collection.com/aicraft/gulfstream-g700/for-sale/#:~:text=and%20the%20map%3A-,Gulfstream%20G700%20Price,as%20high%20as%20%5C$80%20million.

[21] *Bombardier Global 7500*. Accessed: 2025-04-22. 2025. URL: https://www.guardianjet.com/jet-aircraft-online-tools/aircraft-brochure.cfm?m=Gulfstream-G700-208.

[22] *Dassault Falcon 10X*. Accessed: 2025-04-22. 2025. URL: https://www.dassault-aviation.com/fr/civil/la-famille-falcon/falcon-10x/.

[23] *Bombardier Global 7500 vs Gulfstream G700*. Accessed: 2025-04-22. 2025. URL: https://www.avbuyer.com/articles/jet-comparisons/bombardier-global-7500-vs-gulfstream-g700-114094.

[24] Harijono Djojodihardjo and Alvin Kek Leong Wei. "Conceptual Design and Aerodynamic Study of Blended Wing Body Business Jet". In: *28th International Congress of the Aeronautical Sciences*. Sept. 2012. DOI: 10.13140/2.1.2478.1122.

[25] Federal Aviation Administration. *FAR Part 25 - Airworthiness Standards: Transport Category Airplanes*. Accessed April 2025. 2023. URL: https://www.ecfr.gov/current/title-14/chapter-I/subchapter-C/part-25.

[26] International Civil Aviation Organization. *Annex 6 to the Convention on International Civil Aviation: Operation of Aircraft, Part I — International Commercial Air Transport — Aeroplanes*. https://www.icao.int/safety/airnavigation/pages/Annexes.aspx. Accessed April 2025. 2022.

[27] Sir George Cayley. "Aeronautical & Miscellaneous Notebook". en. In: *Cambridge University Press* (1993).

[28] *BigFoil*. Accessed: 2025-04-23. 2025. URL: https://www.bigfoil.com/.

[29] Mark Drela. *XFOIL*. URL: https://web.mit.edu/drela/Public/web/xfoil/.

[30] Martin Hepperle. *JavaFoil*. URL: https://www.mh-aerotools.de/airfoils/javafoil.htm.

[31] Pericles Panagiotou et al. "Quasi-3D Aerodynamic Analysis Method for Blended-Wing-Body UAV Configurations". en. In: *Aerospace* 8.1 (Jan. 2021), p. 13. ISSN: 2226-4310. DOI: 10.3390/aerospace8010013. URL: https://www.mdpi.com/2226-4310/8/1/13 (visited on 04/22/2025).

[32] Snorri Gudmundsson. *General Aviation Aircraft Design: Applied Methods and Procedures*. 1st. Oxford, UK: Butterworth-Heinemann, 2014. ISBN: 978-0-12-397308-5.

[33] Charles D. Harris. *NASA supercritical airfoils: A matrix of family-related airfoils*. eng. Legacy CDMS, 1990.

[34] May-Fun Liou et al. "Aerodynamic Design of the Hybrid Wing Body Propulsion- Airframe Integration". en. In: ().

[35] Daniel P. Raymer. *Aircraft Design: A Conceptual Approach*. 6th. AIAA Education Series, 2018. ISBN: 978-1624104909.

[36] Dr. Jan Roskam. *Part II: Preliminary configuration design and integration of the propulsion system*. eng. Kansas, 1985. ISBN: 1884885438.

[37] Mohit Singh. “Fabrication and Analysis of NACA 0012 Airfoil in Wind Tunnel”. In: *International Research Journal of Engineering and Technology (IRJET)* (2018). Accessed: 2025-04-22. URL: https://www.irjet.net/archives/V5/i5/IRJET-V5I5927.pdf.

[38] Jack D. Mattingly. *Elements of Propulsion: Gas Turbines and Rockets*. AIAA, 2005.

[39] Koen Hillewaert. *Introduction to airbreathing propulsion systems*. Lecture notes. 2024.

[40] European Union Aviation Safety Agency (EASA). *Type-Certificate Data Sheet for Pratt & Whitney PW1500G Series Engines*. IME.090. Version Issue 09. European Union Aviation Safety Agency (EASA). Nov. 2022. URL: https://www.easa.europa.eu/en/document-library/type-certificates/engine-tcds.

[41] Federal Aviation Administration. *14 CFR Part 25 - Airworthiness Standards: Transport Category Airplanes*. Accessed: February 13, 2025. 2024. URL: https://www.ecfr.gov/current/title-14/chapter-I/subchapter-C/part-25.

[42] Leland M. Nicolai and Grant E. Carichner. *Fundamentals of Aircraft and Airship Design*. 1st. Vol. 1. Reston, Virginia: American Institute of Aeronautics and Astronautics (AIAA), 2010. ISBN: 978-1-60086-751-4.

[43] Federal Aviation Administration. *Aviation Fuel Properties - Advisory Circular AC 20-105B*. https://www.faa.gov/documentLibrary/media/Advisory_Circular/AC_20-105B.pdf. Accessed April 2025. 2004.

[44] Shell Aviation. *Jet Fuel Technical Handbook*. https://www.shell.com/business-customers/aviation/aeroshell/technical-library/technical-datasheets.html. 2005.

[45] Panagiotis Laskaridis Nicolas G.M. Moinou Drewan S. Sanders. “Advancements and prospects of boundary layer ingestion propulsion concepts”. In: *Progress in Aerospace Science* 138 (2023).

[46] N.S. Currey. *Aircraft Landing Gear Design: Principles and Practices*. AIAA education series. American Institute of Aeronautics and Astronautics, 1988. ISBN: 9781600860188. URL: https://books.google.be/books?id=XMpdOeWeqq8C.

[47] Sasmita Mohanty et al. “A Review on Utilization of Textile Composites in Transportation towards Sustainability”. In: *Journal of Reinforced Plastics and Composites* 37.24 (2018). Accessed: 2025-02-13, pp. 1435–1451. DOI: 10.1177/0731684418802026.

[48] DragonPlate. *Why is Carbon Fiber Preferred for Aircraft Bodies?* Accessed: 2025-02-13. 2019. URL: https://dragonplate.com/why-is-carbon-fiber-preferred-for-aircraft-bodies.

[49] Ansys. *Granta Edupack Software*. URL: https://www.ansys.com/products/materials/granta-edupack#tab1-3.

[50] ADS Advance. *Hexcel advances A350 structural support*. Accessed: 2025-04-24. Feb. 2018. URL: https://www.adsadvance.co.uk/hexcel-advances-a350-structural-support.html.

[51] A.G. Gibson, Y.S. Wu, and J.T. Evans. “Mechanical behaviour of carbon fibre/epoxy composites at high strain rates”. In: *Polymer Testing* 32.6 (2013), pp. 1061–1069. ISSN: 0142-9418. DOI: 10.1016/j.polymertesting.2013.06.006. URL: https://www.sciencedirect.com/science/article/pii/S0034361713700894.

[52] Hexcel Corporation. *Hexcel to Supply Carbon Fiber Prepreg for Dassault F10X Program*. Accessed: 2025-04-24. May 2021. URL: https://www.hexcel.com/News/News-Releases/3429/hexcel-to-supply-carbon-fiber-prepreg-for-dassault-f10x-program.

[53] Hexcel Corporation. *HexPly® M21 Global Data Sheet*. Accessed: 2025-04-24. July 2017. URL: https://www.hexcel.com/user_area/content_media/raw/HexPly_M21_global_DataSheet.pdf.

[54] Renato Altobelli Antunes, Camilo Augusto Fernandes Salvador, and Mara Cristina Lopes de Oliveira. "Materials Selection of Optimized Titanium Alloys for Aircraft Applications". In: *Materials Research* 21.2 (2018). Accessed: 2025-02-13. DOI: 10.1590/1980-5373-MR-2017-0979.

[55] Adrien Crovato. *DARTFlo*. Sept. 2021. URL: https://gitlab.uliege.be/am-dept/dartflo.

[56] Benjamin Fleck. "Conceptual Design of a Blended Wing Body Business Jet". Master's Thesis. PhD thesis. Cranfield University, 2021. URL: https://dspace.lib.cranfield.ac.uk/server/api/core/bitstreams/bc3da4c0-4dd2-484d-86a4-77c25f64db9f/content.

[57] R. D. Finck. *USAF STABILITY AND CONTROL DATCOM*. US Air Force, 1982.

[58] Dimitriadis Grigorios. *Flight Dynamic And Control*. Lecture 2. 2025.

[59] U.S. Military. *Military specification: flying qualities of piloted airplanes*. US Air Force, 1980.

[60] *Siemens NX*. https://plm.sw.siemens.com/fr-FR/nx/.

[61] Robert H. Liebeck. "Design of the Blended Wing Body Subsonic Transport". In: *Journal of Aircraft* 41.1 (2004), pp. 10–25. DOI: 10.2514/1.9084.

[62] Kevin R. Bradley. *A Sizing Methodology for the Conceptual Design of Blended-Wing-Body Transports*. NASA Contractor Report NASA/CR-2004-213016. NASA Langley Research Center, Sept. 2004. URL: https://ntrs.nasa.gov/api/citations/20040110949/downloads/20040110949.pdf.

[63] Sung Hwan Cho, Cees Bil, and Javid Bayandor. "BWB Military Cargo Transport Fuselage Design and Analysis". In: *Proceedings of the 26th International Congress of the Aeronautical Sciences (ICAS)*. Anchorage, Alaska, 2008. URL: https://www.icas.org/icas_archive/ICAS2008/PAPERS/539.PDF.

[64] Ludovic Noels. *MECA0028 Aeronautical Structures*. Accessed: 2024-04-25. 2013. URL: http://www.ltas-cm3.ulg.ac.be/classes.htm.

[65] John D. Anderson. *Introduction to Flight*. 5th. New York, NY: McGraw-Hill Education, 2005. ISBN: 978-0072825695.

[66] Henrikke Baumann and Anne-Marie Tillman. *The Hitch Hiker's Guide to LCA: An Orientation in Life Cycle Assessment Methodology and Application*. Lund, Sweden: Studentlitteratur AB, 2004.

[67] ecoinvent Association. *ecoinvent Database, Version 3.9.1*. Accessed: 2025-04-17. https://www.ecoinvent.org. 2024.